

Prevailing Triaxial Shapes in Atomic Nuclei and a Quantum Theory of Rotation of Composite Objects

T. Otsuka,^{1,2,3,4,*} Y. Tsunoda,^{5,6} N. Shimizu,^{6,5} Y. Utsuno,^{7,5} T. Abe,^{8,2} and H. Ueno²

¹*Department of Physics, The University of Tokyo, 7-3-1 Hongo, Bunkyo, Tokyo 113-0033, Japan*

²*RIKEN Nishina Center, 2-1 Hirosawa, Wako, Saitama 351-0198, Japan*

³*Institut für Kernphysik, Technische Universität Darmstadt, D-64289 Darmstadt, Germany*

⁴*KU Leuven, Instituut voor Kern- en Stralingsfysica, 3000 Leuven, Belgium*

⁵*Center for Nuclear Study, The University of Tokyo, 7-3-1 Hongo, Bunkyo, Tokyo 113-0033, Japan*

⁶*Center for Computational Sciences, University of Tsukuba, 1-1-1 Tennodai, Tsukuba, Ibaraki, 305-8577, Japan*

⁷*Advanced Science Research Center, Japan Atomic Energy Agency, Tokai, Ibaraki 319-1195, Japan*

⁸*Quantum Computing Center, Keio University, 3-14-1 Hiyoshi, Kohoku-ku, Yokohama 223-8522, Japan*

(Dated: October 1, 2024)

Virtually any object can rotate: the rotation of a rod or a linear molecule appears evident, but a number of objects, including a simple example of H_2O molecule, are of complex shapes and their rotation is of great interest. For atomic nuclei, rotational bands have been observed in many nuclei, and their basic picture is considered to have been established in the 1950's. We, however, show that this traditional picture is superseded by a novel picture. In the traditional view, as stressed by Aage Bohr in his Nobel lecture with an example of ^{166}Er nucleus, most heavy nuclei are like axially-symmetric prolate ellipsoids (i.e., with two shorter axes of equal length), rotating about one of the short axes, like a rod. In the present picture, however, the lengths of these three axes are all different, called triaxial. The triaxial shape yields more complex rotations, which actually well reproduce experimental data, as confirmed by state-of-the-art Configuration Interaction calculations. Two origins are suggested for the triaxiality: (i) binding-energy gain by the symmetry restoration for triaxial shapes, and (ii) another gain by specific components of the nuclear force, like tensor force and high-multipole (e.g. hexadecupole) central force. While the origin (i) produces basic modest triaxiality for virtually all deformed nuclei, the origin (ii) produces more prominent triaxiality for a certain class of nuclei. An example of the former is ^{154}Sm , a typical showcase of axial symmetry but is now suggested to depict a modest yet finite triaxiality. The latter, prominent triaxiality, is discussed from various viewpoints for some exemplified nuclei including ^{166}Er , and experimental findings, for instance, those by multiple Coulomb excitations obtained decades ago, are re-evaluated to be supportive of the prominent triaxiality. Many-body structures of the γ band and the double- γ band are clarified, and the puzzles over them are resolved. Regarding the general features of rotational states of deformed many-body systems including triaxial ones, the well-known $J(J+1)$ rule of rotational excitation energies is derived, within the quantum mechanical many-body theory, without resorting to the quantization of a rotating classical rigid body. This derivation is extended to the $J(J+1)-K^2$ rule for side bands with $K \neq 0$. The present picture of the rotation is robust and can be applied to various shapes or configurations, including clusters and molecules. Thus, two long-standing open problems, (i) occurrence and origins of triaxiality and (ii) quantum many-body derivation of rotational energy, are resolved. Their possible relations to the Nambu-Goldstone mode for the symmetry restoration are mentioned. As one of a few feasible experimental approaches to the triaxiality of the ground state, the Relativistic Heavy-Ion Collision is mentioned. Davydov's claim of triaxial shapes over many nuclei and the validity of his rigid-triaxial-rotor model are separately assessed. Substantial impacts on superheavy nuclei and fission due to the wide occurrence of triaxial shapes are mentioned.

CONTENTS

1. Introduction Referring to Molecular Rotation	2	3.4. Governing triaxiality over the ground and γ bands	9
2. Nuclear Ellipsoidal Deformation	3	4. Underlying mechanism of the triaxiality, symmetry restoration	10
3. Multi-nucleon Structure of ^{166}Er nucleus clarified by CI calculations	5	4.1. Implication of K quantum number for rotational bands	10
3.1. Rotational states of axially-symmetric and triaxial ellipsoids	5	4.2. $K^P = 0^+$ cases	10
3.2. Properties of ^{166}Er nucleus by the present CI calculation	6	4.3. $K^P = 2^+$ cases	12
3.3. Triaxiality of ^{166}Er nucleus and its clarification by T-plot	8	4.4. Relation to symmetry restoration and other remarks	12
		5. A quantum theory of the rotation of multi-nucleon system	13
		5.1. Formulation	13
		5.2. Contributions of leading and next-to-leading orders	14
		5.3. Contributions of next-to-next-to-leading order	14

* otsuka@phys.s.u-tokyo.ac.jp

5.4. Verification Examples	15
5.5. Finite K values	15
5.6. Sketch for projected energy levels for K and J quantum numbers	18
5.7. Remarks on earlier approaches	18
6. Second major source of triaxiality: nuclear forces	18
6.1. Introduction	18
6.2. Monopole and multipole interactions: a brief overview	19
6.3. Central-force contribution	20
6.4. Tensor-force contribution	21
6.5. High- j orbitals, triaxiality and tensor force	21
6.6. Explorations of triaxiality in other nuclei	24
6.7. Contributions to $K=0$ lowering	24
7. Interim Summary for the triaxiality and the rotation	25
8. Related properties and models	27
8.1. γ vibration model	27
8.2. Double γ phonon state	27
8.3. Davydov model	28
8.4. Staggering	28
8.5. Deformed Shell Model and other approaches	28
9. Nuclei around ^{166}Er in the Segrè chart	29
9.1. Trends	29
9.2. Re-visit to early experiments	29
10. Structure of ^{154}Sm	30
10.1. Energies	30
10.2. Tplots	33
10.3. Deformation parameter γ	33
11. Summary and prospects	33
Acknowledgements	37
Author Contributions	37
A. Configuration Interaction (CI) calculation or Shell-model calculation	38
B. Monte Carlo Shell Model and T-plot	38
C. K projection	39
D. Analysis with reduced monopole interaction	41
E. Analysis with Monopole-Frozen interaction	42
references	42

1. INTRODUCTION REFERRING TO MOLECULAR ROTATION

The atomic nucleus comprises Z protons and N neutrons, which are collectively called nucleons. With the mass number $A=Z+N$, a given nucleus is labeled as AX where X denotes

the element, e.g., ^{166}Er for erbium-166 ($Z=68$). The nucleus, as an assembly of many nucleons, exhibits a clear surface with a certain shape. In many nuclei, the shape is an ellipsoid, which rotates [1–3, 5]. There has been the conventional text-book picture of nuclear shape and rotation, as stressed by Aage Bohr in his Nobel-prize lecture in 1975 [6]. The present work, however, depicts a different picture supported by recent studies that were infeasible in earlier days. Before an in-depth description of the major outcome, we overview the rotation of molecular systems, because it is easier to imagine. Figures 1a–b schematically display the rotation of diatomic (O_2) and triatomic (H_2O) molecules [7]. The O_2 molecule is like a rod and rotates about an axis perpendicular to the axis connecting the two O atoms (see Fig. 1a). It cannot rotate about the axis connecting two atoms, because the quantum state does not change by such rotation.

The situation with the H_2O molecule is more complex. As shown in Fig. 1b, this molecule can rotate about more than one axis. Thus, if the molecule has a complex configuration of atoms, its rotational motion occurs about multiple axes.

Nucleons form atomic nuclei with approximately constant nucleon density. The surface of a nucleus can then be discussed because this density sharply drops down outside the surface in most of nuclei. The surface forms a shape. In a naïve picture with the surface tension *à la* the liquid drop, the shape should be a sphere. However, the shape appears, in many nuclei, not to be a sphere but to be an ellipsoid or something close to it [1–3]. Thus, the deformation of the ellipsoid (from the sphere) is a general and basic subject of nuclear physics.

A nuclear analogy to the O_2 molecule can be found in a nucleus with an ellipsoidal shape like Fig. 1c. This type of ellipsoid is stretched on the vertical axis in the paper plane (side view), with a nuclear quantum state invariant under the rotation about the vertical axis (top view). This invariance is called *axial symmetry*, and the vertical axis here is called the *symmetry axis*. In quantum mechanics, no rotational motion arises about the symmetry axis because the state does not change, like a di-atomic molecule (see Fig. 1a). On the other hand, the ellipsoid can rotate about an axis perpendicular to the symmetry axis (side view).

The axial symmetry can be broken in reality. The cross section of the ellipsoid then becomes an ellipse as shown in the top view of Fig. 1d. The rotation can now also occur about the axis perpendicular to this cross section (i.e., the z -axis in Fig. 1e), as seen in the right drawing of Fig. 1d. Although details are different, this is basically similar to the H_2O molecule case: a complex object can rotate in multiple ways.

This article is organized as shown in the Table of Contents. Section 1 is an introduction referring to molecules. Section 2 presents a simple overview of the nuclear surface deformation from a sphere to an ellipsoid and the so-called rotational bands. Section 3 shows the state-of-the-art Configuration Interaction (CI) calculation (the most advanced version of the Monte Carlo Shell Model (MCSM)) on the structure of the nucleus ^{166}Er , reproducing experimentally observed properties and exhibiting its triaxial shapes. General and analytic discussions are presented in Secs. 4 and 5, respectively, on

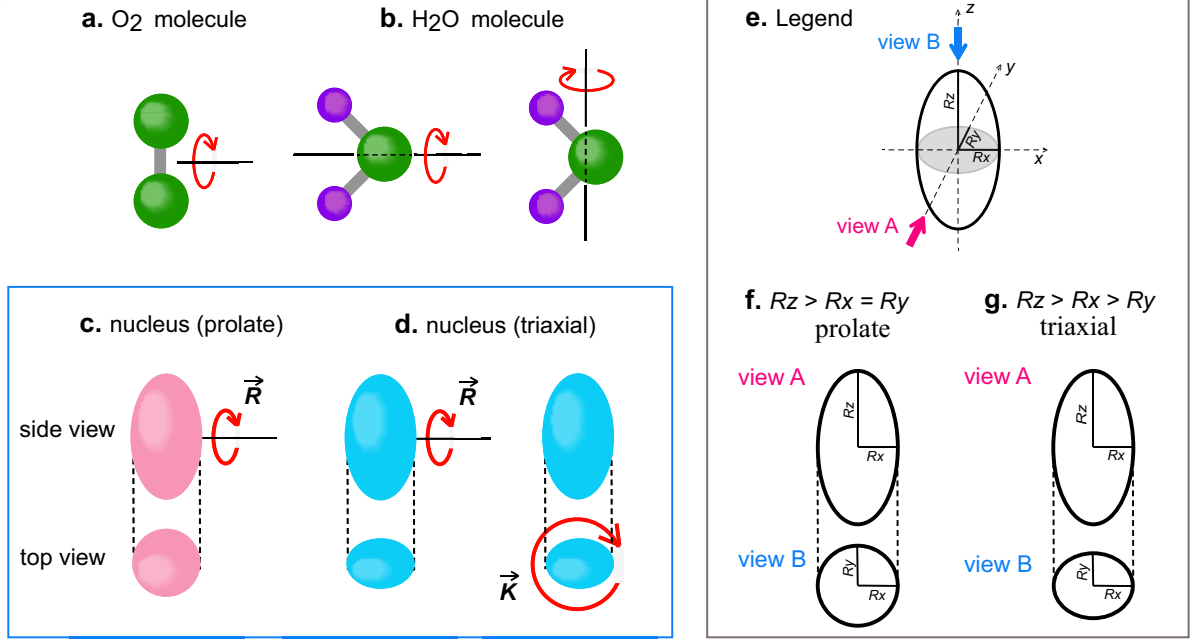


FIG. 1. Schematic illustrations of the rotations of molecules and atomic nuclei. **a** O_2 molecule. **b** H_2O molecule. **c** prolate and **d** triaxial nuclear shapes, with associated rotations \vec{R} and \vec{K} . **e** Legend. **f, g** Principal axes of prolate and triaxial ellipsoids.

the underlying mechanisms of the triaxial shapes and the rotational spectra, by referring to the restoration of two rotational symmetries. It is mentioned that, in Sec. 5, the well-known $J(J+1)$ rule of the rotational spectrum is derived as a J -dependent effect of the nuclear Hamiltonian for a quantum many-body system. This derivation definitely differs from the explanation of the apparently same $J(J+1)$ rule in terms of the quantization of the kinetic energy of a free rigid-body rotor, e.g. [4]. Section 6 shows the second major mechanism for the triaxial shapes based on characteristic properties of nuclear forces. An interim summary of Secs. 4-6 is given in Sec. 7, introducing the basic triaxiality and the prominent triaxiality. It will be deduced from these arguments that the intrinsic structure of a deformed nucleus is not completely decoupled from extrinsic features. This may be in contrast to the typical conventional view pointing to the opposite direction, a good separation between them, e.g. [4].

Some related important topics are mentioned in Sec. 8. In Sec. 9, 13 heavy nuclei are described as nuclei with prominent triaxiality in terms of the CI calculations, and more nuclei are empirically suggested to be so. Sec. 10 presents the discussions on the structure of the nucleus ^{154}Sm , as an example of nuclei that are not triaxial (i.e. axial) traditionally. This will provide a comparison to the discussions in earlier sections. It is also shown that even ^{154}Sm shows a modest but non-vanishing triaxiality, that is the basic triaxiality. Sec. 11 is a summary and prospects, which include concise sketches of the present picture of the nuclear rotation compared to the traditional one, a possible relevance to the Nambu-Goldstone theorem, possible experimental observations of ground-state triaxiality, and remarks on deeply related work by A. S. Davy-

dov and that by D. Cline. There are five appendices, of which Appendices C, D, and E present new but somewhat detailed results and arguments.

2. NUCLEAR ELLIPSOIDAL DEFORMATION

The ellipsoidal deformation of nuclear surface is the main subject of this work. We start with a simple modeling with a uniform nucleon-density distribution inside the surface of the ellipsoid, which also means a discrete drop to zero density outside the surface. The surface is then specified by axes R_x, R_y and R_z as shown in Fig. 1e, where the standard convention for the axis lengths $R_z \geq R_x \geq R_y$ is taken. The ellipsoid is viewed from two different angles, A and B. The prolate ellipsoid is shown in Fig. 1f where $R_x = R_y$ holds. The ellipsoid without the axial-symmetry is shown in Fig. 1g, where the three axes take different lengths. This feature is called *triaxial*. The ellipsoid shows quadrupole moments:

$$Q_0 = \langle 2z^2 - x^2 - y^2 \rangle, \quad (1)$$

and

$$Q_2 = \sqrt{3/2} \langle x^2 - y^2 \rangle, \quad (2)$$

where $\langle \rangle$ implies the integral of the designated quantity multiplied by the matter (or charge if appropriate) density. The prolate shape is characterized by positive Q_0 and vanishing Q_2 , whereas the triaxiality is by finite Q_2 . We show, in this paper, the unexpected preponderance of the triaxiality, its consequences in nuclear rotation and its robustness rooted in symmetry restoration and nuclear forces. Although the oblate ellipsoid $R_z = R_x > R_y$ is another possible case, it emerges at

rather high excitation energies in the nuclei to be discussed. Consequently, the oblate shape will be discussed elsewhere.

The nuclear shape is studied, in the present work, as a quantum many-body problem. The nuclear structure is described by the wave functions obtained by solving an appropriate many-body Schrödinger equation, where the Hamiltonian contains terms representing nuclear forces. A possible interpretation of the major origin of the deformed nuclear shapes is depicted in Fig. 2a. Short-range attractive forces between nucleons produce substantial binding energies for nucleons configured with an appropriate density like the lower part of Fig. 2a. However, if an isotropic density distribution is assumed, active nucleons are isotropically distributed in an outer layer of a certain thickness (see upper part of Fig. 2a) because of the shell structure: radial wave functions of single-particle orbitals are rather widely spread near the surface. The nucleon density then becomes lower than that of the lower part of Fig. 2a, resulting in a weaker binding due to fewer nucleons within the range of nuclear forces. This interpretation appears to be consistent with results of quantum many-body calculations of various types including the present ones to be shown. This interpretation is obtained based on a constant nucleon density, a shell structure and a short-range attractive force, where the short range refers to a distance shorter than the nuclear size. An in-depth analysis of this interpretation seems to be an intriguing topic.

In eigenstates of the Schrödinger equation of the current interest, nuclear shapes appear as consequences of many-body correlations (or collective motion), including Jahn-Teller effect [9]. To be more concrete, as the nucleus is treated as a multi-nucleon quantum system, the quadrupole moments and other related quantities are calculated from their wave functions. Although the nucleus in such quantum mechanical descriptions shows a density approximately uniform and a surface with imperfect sharpness, it can be connected to the afore-mentioned uniform-density classical ellipsoid with the same values of the quadrupole moments. Such a mapping to the classical image serves as a useful intuitive way for grasping the essence of the structure of atomic nuclei, leaving other details untouched. It is noted that all physical quantities are obtained in this article by quantum many-body calculations.

Attractive forces relevant to Fig. 2a are much stronger between a proton and a neutron than between two neutrons or between two protons. This implies that the deformation becomes strong if there are sufficiently large numbers of active (or valence) protons and active neutrons, outside the inert core (see Fig. 2a). On the other hand, if the protons (neutrons) form a closed shell, as the closed shell is spherical, the neutrons (protons) also form a spherical shape.

Different nuclear shapes result in visible differences in observables. Figure 2c exhibits the global systematics of the level energies of the lowest state of spin/parity $J^P=2^+$ for even- Z and even- N (*even-even*) nuclei, on top of the $J^P=0^+$ ground state. For doubly-magic nuclei, the excitation from the ground state can be made by moving a nucleon over a magic gap. This requires a large amount of energy, meaning a high excitation energy. There are high spikes in Fig. 2c with the excitation energies more than 2 MeV (see green open circles).

These spikes correspond to conventional ($N=8, 20, 28, 50, 82, 126$) or new ($N=16, 32, 34, 40$) magic numbers. Beyond $N \sim 40$, most of the points (blue closed circles) show low excitation energies down to several tens of keV. An example of such low excitation energies is shown for the nucleus, ^{166}Er , in the yellow-shaded part of Fig. 2b, which displays the lowest states of $J^P=2^+, 4^+$ and 6^+ . The excitation energy for each J^P is denoted $E_x(J^P)$ hereafter. Their experimental values are depicted in the left part in the yellow-shaded area of Fig. 2b. In the right part, shown are $E_x(J)$'s in the rotor limit,

$$E_x(J^P) = \kappa J(J+1), \quad (3)$$

where the value of κ is adjusted to the measured 2^+ level energy, yielding a salient agreement for $J^P=4^+$ and 6^+ . The $J(J+1)$ dependence of $E_x(J)$ in eq. (3) can be explained by quantizing the rotation of axially-symmetric classical rigid body, such as a symmetric top. Note that this explanation is obtained by replacing a quantum many-body system with a classical rigid body. Apart from this issue to be addressed later in this article, we come up with the image that a strongly deformed ellipsoid like the lower part of panel a “rotates” with $J^P=2^+, 4^+, 6^+, \dots$. Similar rotational bands have been observed in many heavy nuclei. The systematics shown in Fig. 2c exhibits many of heavy nuclei with the first 2^+ state, denoted as 2_1^+ , at a very low excitation energy. This implies large moments of inertia indicative of strong ellipsoidal deformation.

The green shaded area of Fig. 2b displays observed level energies of ^{124}Sn nucleus ($Z=50, N=74$), where the $Z=50$ proton closed shell results in a spherical shape for its ground state. Its $J^P=2_1^+$ level is lying high, partly because of the absence of a mechanism like Fig. 2a. This feature is depicted by closed green circles in Fig. 2c, forming a minor fraction of the points.

Figure 3 exhibits observed 2_1^+ excitation energies, $E_x(2_1^+)$, for the nuclei filtered by the criterion $3.00 \leq E_x(4_1^+)/E_x(2_1^+) \leq 3.33$, as of the year 2023 [8]. Note that eq. (3) produces this ratio=10/3. Few nuclei fulfill this condition for the mass number, $A = Z + N \leq 42$, comprising stable ^{24}Mg nucleus ($Z=N=12$) and exotic ^{42}S nucleus ($Z=16, N=26$), as well as very neutron-rich exotic nuclei $^{34,36,38}\text{Mg}$ ($Z=12, N=22, 24, 26$). The next group consists of just nine nuclei, $^{100,102,104,106}\text{Zr}$ ($Z=40, N=60, 62, 64, 66$), ^{106}Mo ($Z=42, N=64$), ^{122}Ce ($Z=58, N=64$), $^{128,130}\text{Nd}$ ($Z=60, N=68, 70$) and ^{132}Sm ($Z=62, N=70$). Between $A=150$ and 208, however, a large number (66) of nuclei fulfill this severe condition with low $E_x(2_1^+)$ values, mostly below 0.125 MeV. This overall trend suggests that strong shape deformation primarily occurs in heavy nuclei with $A > 150$. Naturally, the focus of this study is placed upon these nuclei, while the shapes of lighter nuclei are also interesting in the view to be presented and will be discussed elsewhere from the present perspectives.

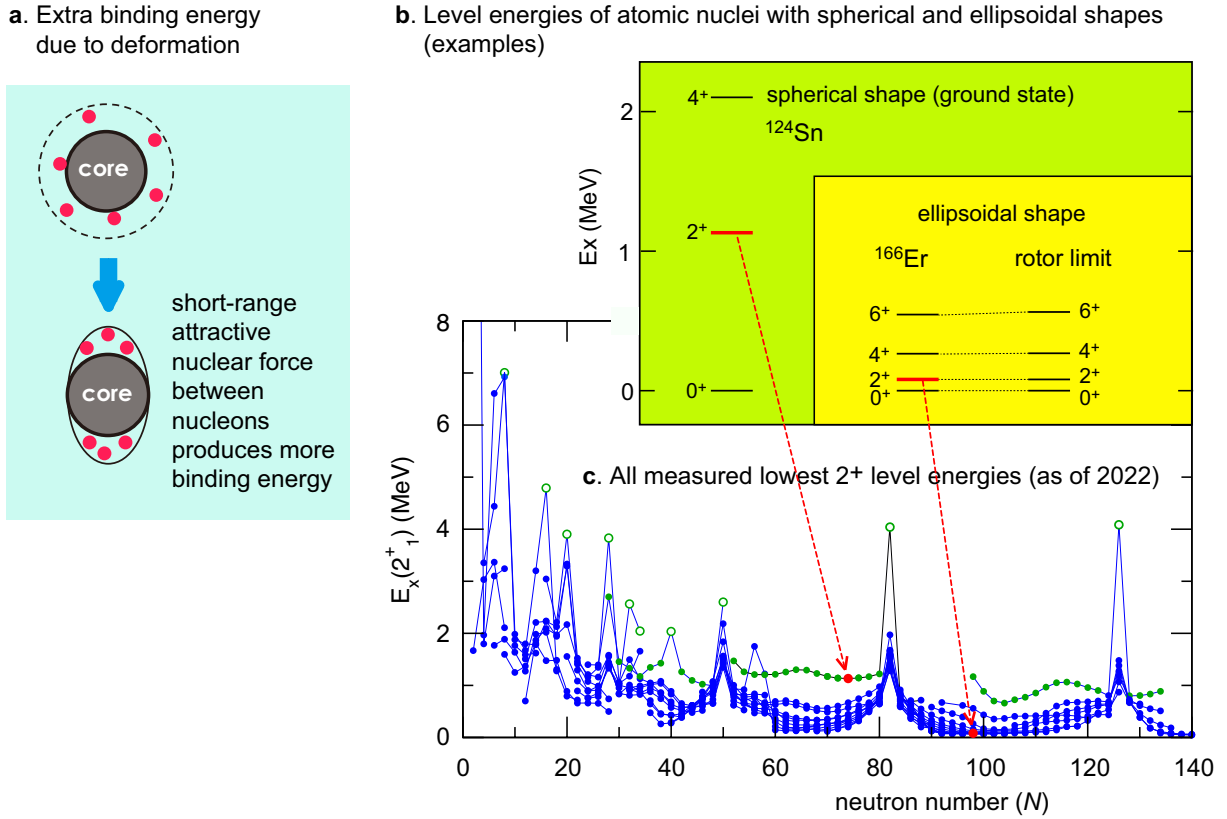


FIG. 2. Overview of the 2^+_1 states. **a** Intuitive picture of the major mechanism to drive ellipsoidal deformation. **b** Examples of spherical and deformed cases with the rotational level energies. **c** All measured lowest 2^+ level energies of even-even nuclei as of the year 2022, based on the data taken from NuDat 3.0 [8]. The open and closed circles indicate the individual 2^+ levels. The circles within a given isotope chain are connected by lines to guide the eye.

3. MULTI-NUCLEON STRUCTURE OF ^{166}Er NUCLEUS CLARIFIED BY CI CALCULATIONS

3.1. Rotational states of axially-symmetric and triaxial ellipsoids

Figures 1c, d display two cases of the shape deformation. Between the two, the axially symmetric shape (panel c) has been considered to occur in the majority of deformed heavy ($A > 150$) nuclei, such as those with low $E_x(2^+_1)$ values in Fig. 3, since Bohr and Mottelson suggested [5, 6]. This picture has been a textbook item over 70 years [4, 10, 12], and many works were made on top of it, for instance, the fission mechanism [13, 14]. As an example, Möller *et al.* presented, based on the finite-range liquid-drop model [15, 16], effects of the axial-symmetry breaking on the nuclear mass, covering the Segrè (nuclear) chart, but no notable effects were found for the deformed heavy nuclei mentioned above (see Fig. 2 of [16]).

The axially symmetric ellipsoid can rotate about one axis as shown in Fig. 1c, with the corresponding angular momentum, \vec{R} . This is nothing but the total angular momentum $\vec{J} (= \vec{R})$. Its magnitude, J , and one of its components are conserved by the Hamiltonian. If the triaxial shape sets in, another rotation of

the ellipsoid emerges, because of an ellipse in the right part of Fig. 1d, and is shown by \vec{K} , the angular momentum about the z axis of the body-fixed frame. The total angular momentum is intuitively expressed as $\vec{J} = \vec{R} + \vec{K}$. The conservation law holds for \vec{J} , but not for \vec{R} or \vec{K} separately. The \vec{K} is pointing in the z direction of the body-fixed frame, with its z component denoted by K as usual. Because the rotation by \vec{K} actually occurs in the xy plane of the body-fixed frame, it is essentially two-dimensional rotation and only the z -component K is relevant. The value of K seems to be approximately conserved (or not mixed significantly) in actual triaxial cases discussed in this article, primarily due to larger excitation energies caused by this particular rotation. Note that although positive values of K are mentioned in many cases, it can be negative, as it is a z component. The phrases, K rotation and K quantum number, will appear in these senses.

The surface tension of a liquid drop generally tends to minimize its surface area, ending up with a sphere in an extreme case. The nuclear shape may be considered to be an equilibrium between this surface tension and the force causing the deformation *à la* Fig. 2a. An axially-symmetric ellipsoid is then favored over a triaxial one, because of the constant curvature in the xy plane. The rotation of such rigid bodies is described, for instance, in textbooks [10, 12]. As a multi-

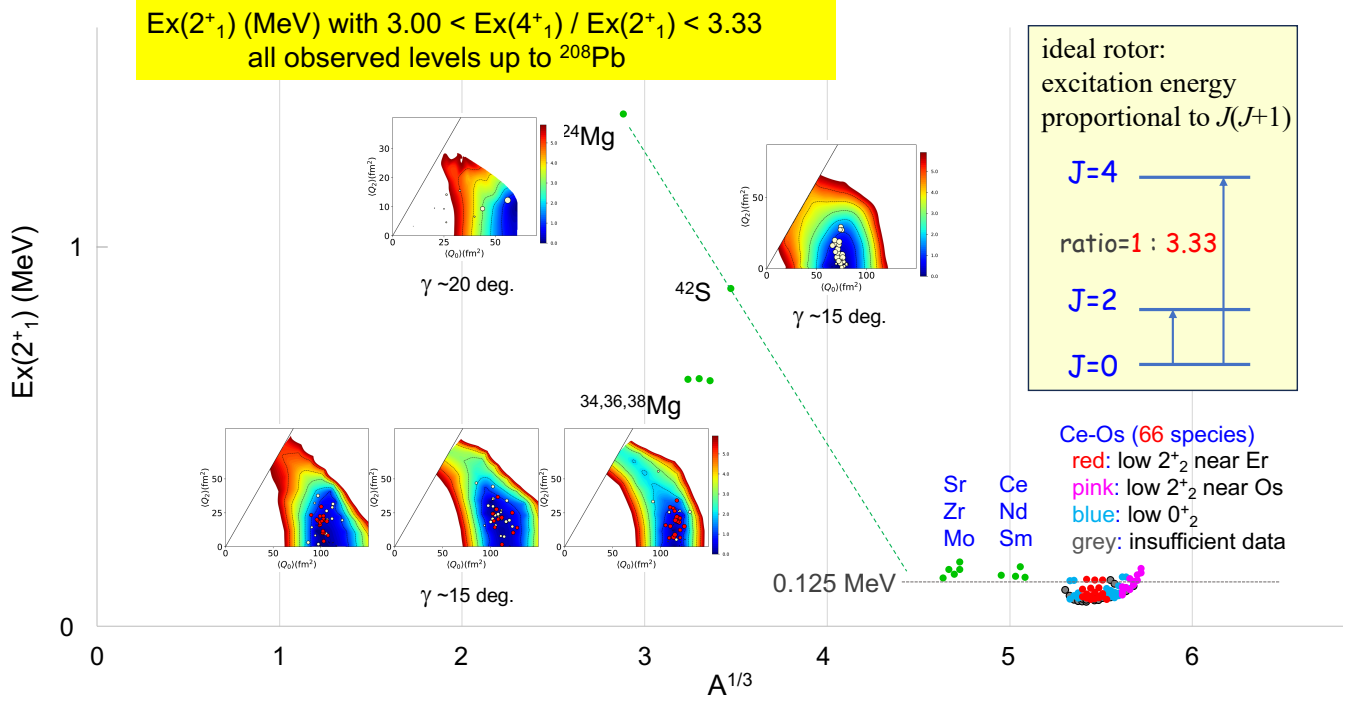


FIG. 3. Observed appearance of low-lying first 2^+ level energy as a function of mass number, A , as scaled by $A^{1/3}$. All cases of even-even nuclei up to ^{208}Pb are included as of 2023. The first 2^+ level energy is shown by a circle for each nucleus. Nuclei heavier than $A > 140$ ($A^{1/3} > 5.2$) are classified by their level structure as described in the figure. The line of the excitation energy of 0.125 MeV is displayed to guide the eye. T-plot is displayed for the five lightest nuclei. The inset shows the basic picture of rotational band.

nucleon problem, Kumar and Baranger [17] performed the “pairing-plus-quadrupole model” calculation, as a then most advanced many-body calculation, and advocated the “preponderance of axially symmetric shapes” for many species of nuclei. A similar work was reported by Bes and Sorensen [18]. These works indicated that once many nucleons in many single-particle orbits of a mean potential coherently contribute, the axially-symmetric prolate deformation likely occurs. The SU(3) model is a symmetry-based many-body approach, and favors the same feature in some cases [19, 20], as well as its approximate extensions [21].

Figure 4a shows a schematic picture of the prolate deformed ground state and its rotational excitations. Figure 4a includes another type of excitation, called γ vibration [5, 6]. In this mode, the circle in the lower part of Fig. 1c is distorted to an ellipse. However, the distortion is not static, and is a vibrational motion. This vibration occurs in the excited state shown in the right upper part of Fig. 4a, but not in the members of the ground-state band (i.e., the rest of Fig. 4a). This vibrational excitation is represented by γ phonon in a quantum mechanical description, thus denoted as “ γ phonon excitation” in Fig. 4a. The 2_2^+ state is then identified as the one- γ -phonon state on top of the deformed equilibrium [5, 6].

3.2. Properties of ^{166}Er nucleus by the present CI calculation

Figure 4c depicts measured excitation energies as well as electromagnetic decays and moments [22], for ^{166}Er ($Z=68$, $N=98$) as an example. The decays are actually electric quadrupole (E2) transitions, and their strengths are expressed by squared E2 strengths called $B(E2; J^+ \rightarrow J'^+)$ [4, 11, 12]. The 2_2^+ state decays to the ground state through relatively strong transition with $B(E2; 2_2^+ \rightarrow 0_1^+) = 5.17 \pm 0.21$ (W.u.) (see panel c), where W.u. implies the single-particle (Weisskopf) unit [11]. Such a moderately large $B(E2)$ value was interpreted as an indication that the 2_2^+ state is a phonon excitation which is collective to a certain extent [6].

We present a recent work on this subject from a modern viewpoint combined with state-of-the-art configuration interaction (CI) calculations with a realistic effective nucleon-nucleon (NN) interaction. The CI calculation in nuclear physics is called *shell model*, and some introductory details are found in Appendix A. The CI calculation here means Monte Carlo Shell Model (MCSM) [23–26], which enabled us to carry out CI calculations far beyond the limit of the conventional CI approaches, on contemporary subjects [27–37]. Some details of the MCSM are presented in Appendix B. A large number of single-particle orbits are taken as activated orbitals so that the ellipsoidal deformation can be described, 8 for protons and 10 for neutrons. It is pointed out that the

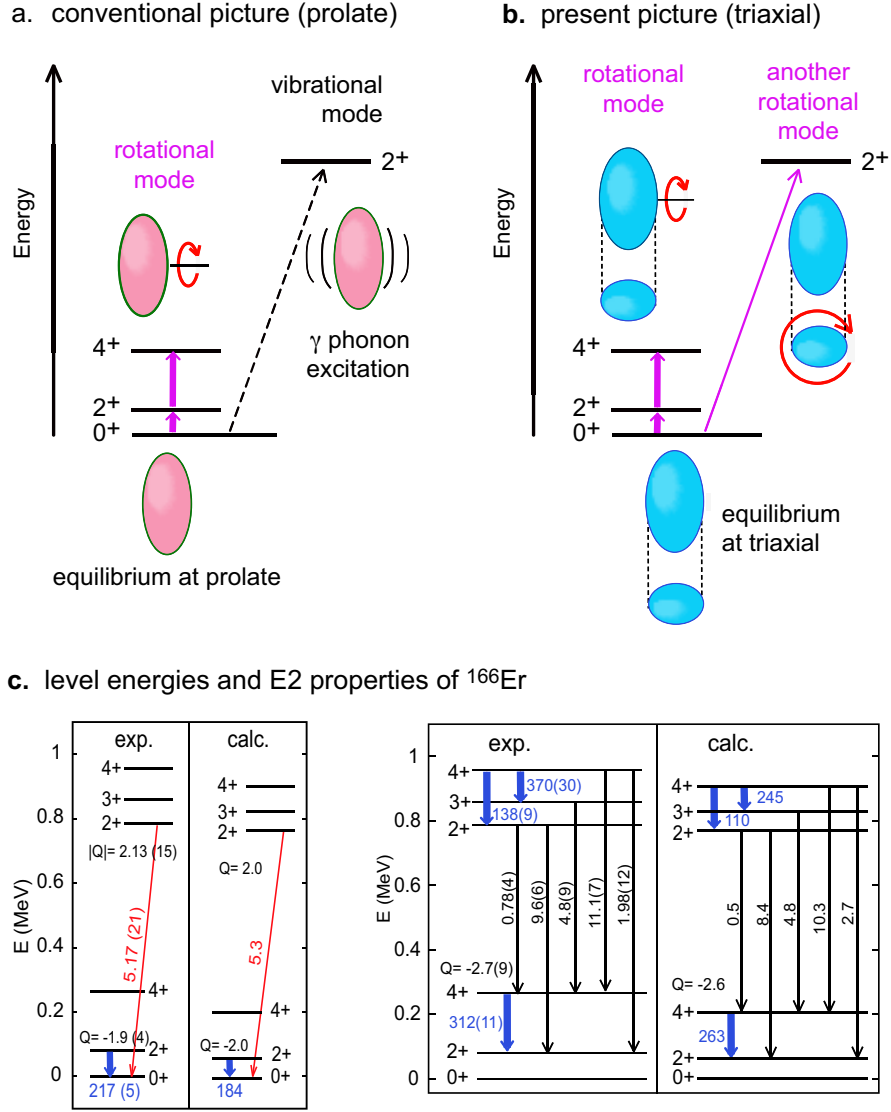


FIG. 4. Schematic pictures of rotational motion and actual features. **a** Conventional picture (prolate shape) and γ vibration from it. **b** Present picture (triaxial shape). **c** Levels and E2 properties of ^{166}Er ($Z=68$, $N=98$) compared to experimental data [22]. $B(E2)$ values are in W.u., and spectroscopic electric quadrupole moments, Q , are in e barn.

energetically lower part of the activated orbitals belong to the closed shell in usual shell-model calculations, meaning that a smaller closed inert core is taken in this work. The nucleus ^{166}Er is first discussed as a typical example, with 28 active protons and 28 active neutrons. The present work goes far beyond the earlier paper [33], as new developments will become clear after all novel features are depicted. The present CI calculations are carried out by the most advanced methodology in the MCSM, called Quasiparticle Vacua Shell Model (QVSM) [38], where the number-projected quasiparticle vacua are used as basis vectors, instead of Slater determinants adopted in usual MCSM calculations. The number-projected quasiparticle vacua can be described, in simple terms, as the Hartree-Fock-Bogoliubov-type states with controlled u and v amplitudes [38]. Namely, the particle-number projection is incor-

porated in the sense of the variation-after-projection. The basis vectors are selected from a large group of candidate states generated stochastically, so that the possible maximal lowering of the energy eigenvalues of interest can be obtained. The selected basis vectors are further optimized by variational procedures [23, 38]. Some details of the computational methodology are presented in Appendix B.

The Hamiltonian for the present CI calculations is a slight modification of its prototype used in the earlier work [33]. The proton-neutron (interaction) part was obtained from the monopole-based-universal interaction, V_{MU} [39], which consists of the central force and the tensor force. The central force is a Gaussian interaction, where the parameters were fixed so as to simulate the shell-model and microscopic (G -matrix) interactions [39], and has been used in many studies, up to Hg

isotopes [30]. The tensor force was taken from [40], where the strengths were obtained from π -nucleon scattering data in the free space. The proton-proton and neutron-neutron interactions were fixed in [33] mainly based on the microscopic interactions used in [41]. In the earlier work, the pairing correlations in wave functions may have been underestimated because of the Slater-determinant basis vectors in the original MCSM, and the strengths of pairing interactions were likely taken to be stronger, in order to compensate the possible underestimation of their effects. This problem vanishes in the present calculation to a large extent, because the pairing energy can be better carried by individual basis vectors being of HFB (Hartree-Fock-Bogoliubov) (or BCS) type. The pairing strengths are rescaled to be somewhat weaker. The SPE values are also changed slightly. Although the basic outcomes of the earlier work [33] remain in the present work, many novel features emerge in the underlying theories and in the range of nuclei, and, in some cases, traditional arguments are corrected under new views.

Figure 4c depicts calculated level energies and E2 properties of ^{166}Er , in a good agreement with experiment, including both large and small values of $B(E2)$. The present value of $B(E2; 2_2^+ \rightarrow 0_1^+)$ is 5.3 W.u. in a salient agreement with experiment, and urges us to look into underlying multi-nucleon structure of the eigenstates.

3.3. Triaxiality of ^{166}Er nucleus and its clarification by T-plot

For unveiling the underlying structure, deformation parameters β_2 and γ are introduced [5] to indicate how the sphere with the radius R_0 is deformed to ellipsoids (see textbook for example [4]). The three axes of the ellipsoid in the classical uniform-density model are expressed as

$$R_z = \{1 + 0.63\beta_2 \cos \gamma\} R_0, \quad (4)$$

$$R_x = \{1 + 0.63\beta_2 \sin(\gamma - 30^\circ)\} R_0, \quad (5)$$

$$R_y = \{1 - 0.63\beta_2 \cos(60^\circ - \gamma)\} R_0. \quad (6)$$

Prolate shapes ($R_x=R_y$) correspond to $\gamma=0^\circ$, while triaxial shapes emerge for $0^\circ < \gamma < 60^\circ$. Usually, $\beta_2 \geq 0$ and $0^\circ \leq \gamma \leq 60^\circ$ are considered, implying $R_y \leq R_x \leq R_z$. The quadrupole moments, Q_0 and Q_2 , are calculated for a given ellipsoid specified by β_2 and γ , with R_0 properly taken.

In quantum multi-nucleon approaches, quadrupole moments Q_0 and Q_2 are obtained from relevant matrix elements of the state of interest. The corresponding β_2 and γ values are obtained so that the classical uniform-density model yields the same Q_0 and Q_2 values with appropriate β_2 and γ values. We will use such β_2 and γ values in the quantum many-body studies.

The β_2 parameter obviously stands for the magnitude of the quadrupole deformation, and the relation, $\beta_2^2 \propto (Q_0^2 + 2Q_2^2)$, holds in the lowest order. In practical studies, this approximation appears to be sufficiently good and is adopted, also

in the present work. Typically, β_2 is about 0.3 for heavy deformed nuclei being discussed. The deformation parameter (also called triaxial parameter) γ is usually given by the simple relation (e.g., eq. (5-82) in [5]),

$$\tan \gamma = \sqrt{2} \frac{Q_2}{Q_0}. \quad (7)$$

This relation is also taken in this article. We note that in the present work, in-medium polarization corrections to shell-model Q_0 and Q_2 values are incorporated [42, 43], in order to obtain β_2 and γ values.

A constrained mean-field (more concretely HFB) calculation is carried out by imposing various values of (β_2, γ) as constraints. The obtained energy expectation value is displayed by contour plot in Fig. 5b, with a legend in Fig. 5a. This plot is usually called the potential energy surface (PES). The same Hamiltonian as in the present CI (i.e. MCSM (more precisely QVSM)) calculations is consistently used. The PES in Fig. 5b suggests that the bottom part of the PES spreads over finite γ values, and the precise inspection actually indicates that the minimum is not at $\gamma=0^\circ$ but around $\gamma \sim 9^\circ$. This contradicts the prolate preponderance hypothesis believed over seven decades. For $\beta_2 = 0.30$ and $\gamma=9^\circ$, the values of $R_{x,y,z}/R_0$ are 0.93, 0.88 and 1.19, respectively.

The wave functions of the MCSM are expanded by so-called MCSM basis vectors, which are presently number-projected quasiparticle vacua [38]. Each of the basis vectors has quadrupole moments, from which the corresponding (β_2, γ) value is obtained, after properly aligning the three axes for each basis vector. The individual basis vector can be represented by a circle pinned down on the PES according to this (β_2, γ) value, which now serves as a ‘‘partial labeling’’ of the basis vector. The importance of each basis is depicted by the circle’s area proportional to the overlap probability with the eigenstate. This visualization is called T-plot [44], and turned out to be very useful (see Appendix B for details).

If K quantum number is conserved, E2 matrix elements follow certain regularities [5]. The actual values indeed follow them remarkably well. For instance, the spectroscopic quadrupole moment vanishes for $K=2$ and $J=3$, and this is the case for the 3_1^+ state. Combining such properties with strong E2 transitions expected within individual rotational bands, the band structure is assigned as $K \approx 0$ for the 0_1^+ , 2_1^+ , 4_1^+ states forming the so-called *ground band*, $K \approx 2$ for the 2_2^+ , 3_1^+ , 4_2^+ states forming the so-called *γ band*, and $K \approx 4$ for the 4_3^+ state. The approximate conservation of K quantum number is a well-known feature, for instance, [45], and is discussed for ^{166}Er also in [46].

Figure 5c displays the T-plots for the 0_1^+ , 2_1^+ , 4_1^+ states (ground-band members), and the 2_2^+ , 3_1^+ , 4_2^+ states (γ -band members), as well as the 4_3^+ state. All of them exhibit remarkably similar T-plot patterns, i.e., the mean position and spreading pattern around it. Because the T-plot displays the corresponding shapes of individual basis vectors in the body-fixed (or intrinsic) frame, this similarity suggests a rather common intrinsic (i.e., body-fixed-frame) structure, which includes triaxial shape. This observation is consistent with the picture shown in Fig. 4b: all these states can be generated, to a very

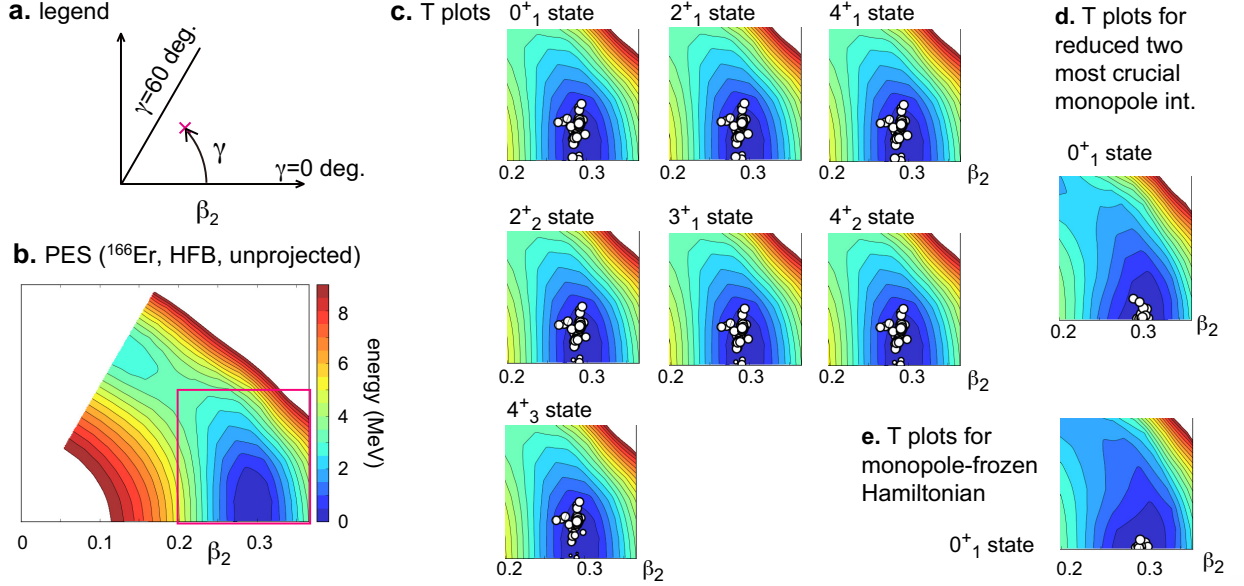


FIG. 5. PES and T-plots for ^{166}Er . **a** Legend. **b** PES. **c** T-plots of ground and low-lying states for the red-square region of **b**. **d** T-plots for reduced crucial monopole interactions. **e** T-plots for monopole-frozen Hamiltonian.

large extent, by rotating a common triaxial ellipsoidal state in multiple ways.

The mean value of γ is calculated, by the method described in [43], to be 8.2° for each member of the ground band, 9.1° for each member of the γ band, and 9.5° for the 4^+_3 state, where small variations within a band (beyond two digits) are ignored. These values are almost the same, and in particular, are almost exactly so within a band. This fact suggests that a fixed triaxial shape governs ^{166}Er . Fine details are consistent with the present band assignment of individual states. This property holds up to the 4^+_3 state, where the CI calculation stopped due to the computer resource.

We stress that the values of β_2 and γ can be evaluated, within the Kumar invariant approach, from quadrupole matrix elements between low-lying eigenstates [47]. An application with the outcome of the present CI calculation shows $\beta_2 \sim 0.3$ and $\gamma \sim 9.2^\circ$, which are similar to the T-plot values mentioned above, implying that the present way for estimating β_2 and γ values is basically consistent with the Kumar invariant method.

Very importantly, Davydov and his collaborators made a pioneering theoretical work of the systematic appearance of triaxial shapes in a number of nuclei, including strongly deformed ones such as ^{166}Er , already around 1958 [48, 49]. Some discussions on this Davydov model will be presented in Subsec. 8.3. We mention that triaxial shapes have been studied extensively for medium-mass nuclei with weaker ellipsoidal deformations, as exemplified by works on $^{74,76}\text{Zn}$ [51], ^{76}Ge [52] or ^{78}Se [53], and also that this article is focused on strongly deformed and clearly rotational nuclei depicted in Fig. 3. In fact, none of $^{74,76}\text{Zn}$, ^{76}Ge or ^{78}Se nuclei appears in Fig. 3.

3.4. Governing triaxiality over the ground and γ bands

The mean value of the deformation parameter γ is quite close between the ground and γ bands, with a minor difference of about 1° . This difference reflects a slight structure change from the ground band to the γ band, and its impact on the relative energy between these two bands is of a certain interest. While the energy of the 0^+_1 state is calculated with many basis vectors (see Appendix B for details), the first basis vector, denoted ξ_0 here (ϕ_1 in eq. (B1) for 0^+_1), is most important among them: it indeed shows a large overlap probability with the final solution, 89% after the projections and normalization. We next look at the 3^+_1 member of the γ band. This state has no counterpart in the ground band and should well represent features of the γ band. We first calculate its energy by using ξ_0 alone, similarly to the 0^+_1 state. Although the obtained energy of 3^+_1 state is not too bad, its difference from the 0^+_1 -state value is 1.27 MeV, which is notably larger than the 3^+_1 excitation energy by the present MCSM calculation shown in Fig. 4c, that is 0.83 MeV. However, instead of ξ_0 , by using another state, ξ_3 , determined by solely lowering the energy of the 3^+_1 state, the obtained 3^+_1 state comes down from 1.27 MeV to 0.76 MeV above the 0^+_1 state obtained from ξ_0 . This difference is apparently closer to the calculated 3^+_1 level energy (0.83 MeV in Fig. 4c). The overlap probability with the final solution becomes as high as 88%. Thus, the most optimum basis vector is slightly different between the 0^+_1 and 3^+_1 states. By including additional basis vectors into the actual MCSM calculation, the energies of the 0^+_1 and 3^+_1 states come down approximately in parallel, and their difference swiftly reaches the value shown in Fig. 4c.

The value of γ is 8.5° and 9.8° for ξ_0 and ξ_3 , respectively, being similar to the mean γ values of the ground and γ bands. The analysis above indicates that this difference lowers the

γ -band excitation energy by ~ 0.5 MeV. Once this lowering is incorporated, additional basis vectors do not substantially change the γ -band excitation energy, ending up with a 0.07 MeV shift in the final solution. These features suggest that the γ -band excitation energy is substantially lowered due to this enlargement (i.e., from 8.5° to 9.8°) of the triaxial deformation. This lowering will be discussed in Subsec. 5.6 from a different viewpoint. We stress that this effect is an outcome of NN interactions contained in the MCSM calculation.

4. UNDERLYING MECHANISM OF THE TRIAXIALITY, SYMMETRY RESTORATION

4.1. Implication of K quantum number for rotational bands

We here begin to discuss by what underlying mechanism the triaxiality is favored. The triaxial intrinsic state (i.e., body-fixed-frame state) ϕ is considered, and the state ξ_0 discussed in Sec. 3.4 is used as an illustrative example for it, while the argument is rather general. Assuming that various eigenstates can be generated from a single ϕ in a good approximation, we extract, from ϕ , the state of definite J and M , that are the total angular momentum and its z -projection in the laboratory frame. This projection can be achieved, as usual, by rotating ϕ in the three-dimensional space with three Euler angles α, β and γ , and by integrating it with an appropriate weighting factor. The process can be expressed by the following well-known equation,

$$\Psi[\phi, J, M, K] = (2J+1)/(8\pi^2) \int_0^{2\pi} d\alpha \int_0^\pi d\beta \sin\beta \int_0^{2\pi} d\gamma \{D_{M,K}^J(\alpha, \beta, \gamma)\}^* e^{i\alpha\hat{J}_z} e^{i\beta\hat{J}_y} e^{i\gamma\hat{J}_z} |\phi\rangle, \quad (8)$$

where D is the Wigner's function. For the D function and other related quantities, we adopt the convention of Edmonds [54], which is also used in [4] with a summary in its Appendix A. Note that γ here is different from the deformation parameter γ , but no confusion is expected in this traditional usage of the character. (Note that the deformation parameter γ will be mentioned in the unit of degrees, whereas the Euler angle γ in radian.) Equation (8) implies that the three-fold rotation of ϕ generates states with good (J, M) pairs. One notices an additional index of K . In fact, there can be different and independent states from the same ϕ for a given pair (J, M) , and K specifies them. This K arises from the J_z rotation ($e^{i\gamma\hat{J}_z}$) with the weighting factor,

$$D_{M,K}^J(\alpha, \beta, \gamma) = e^{iM\alpha} d_{M,K}^J(\beta) e^{iK\gamma}, \quad (9)$$

with $d_{M,K}^J(\beta)$ being the (small) d function. This K in eq. (9) is identified as the z -component K for the rotation about the z axis in the body-fixed frame (see the red circular arrow in the right drawing of Fig. 1d). Although the K quantum number is not conserved in a rigorous sense, it serves as an approximate quantum number at least for strongly deformed nuclei, as we shall see. Moreover, the states of $J = 0$ can be extracted only from $K = 0$ components.

We first decompose ϕ according to K value. This is straightforward because of the factorization in eq. (9): the integration with the Euler angle γ is separated, and the projected state can be obtained by rotating ϕ about the z axis as,

$$\Phi[\phi, K] = \frac{1}{N_K} \frac{1}{2\pi} \int_0^{2\pi} d\gamma e^{i\gamma(\hat{J}_z - K)} \phi, \quad (10)$$

where N_K is a normalization constant.

4.2. $K^P = 0^+$ cases

We begin with the $K = 0$ state, which is particularly simple, because the contributions from all γ angles are equally superposed:

$$\Phi[\phi, K = 0] = \frac{1}{N_0} \frac{1}{2\pi} \int_0^{2\pi} d\gamma e^{i\gamma\hat{J}_z} \phi. \quad (11)$$

The idea behind these complex mathematical expressions can be visualized in Fig. 6 (a), where the rotated states are explicitly displayed for discretely sampled angles $\gamma = 0, \pi/4, \pi/2, 3\pi/4$. We see that all rotated states are uniformly superposed.

The expectation value of the Hamiltonian H with respect to the state in eq. (11) is given by

$$\begin{aligned} h_{K=0} &= \langle \Phi[\phi, K = 0] | H | \Phi[\phi, K = 0] \rangle \\ &= \frac{1}{|N_0|^2} \frac{1}{2\pi} \int_0^{2\pi} d\gamma \langle \phi | H | e^{i\gamma\hat{J}_z} \phi \rangle. \end{aligned} \quad (12)$$

This summation is visualized in Fig. 6 (d) again for selected discrete angles. It is clear that all combinations are summed up with the same factor. The nuclear forces can connect $|\phi\rangle$ to $|e^{i\gamma\hat{J}_z} \phi\rangle$, state rotated by angle γ . The integrand is largely negative (strong binding) at $\gamma=0^\circ$, and it is expected to continuously decrease in magnitude as γ moves away from 0. The integrated contributions are then considered to be also negative with realistic nuclear forces, giving additional binding energy to the nucleus. Beyond $\gamma = \pi/2$, because of approximate symmetry between γ and $\pi - \gamma$, the contribution will be bounced back to a good extent. This feature is general, and its effect as additional binding energy is robust.

We now evaluate how much this K projection changes the energy, as the rest of the total effect of eq. (8) will be discussed in the next section. The ξ_0 state is taken as an example. Its energy without the K projection (i.e., “unprojected” energy) is -391.6 MeV. (Note that parity projection lowers this energy by 1.2 MeV.) Related quantities discussed hereafter are supposed to be projected onto the positive parity if not explicitly mentioned, except for “unprojected” quantities unless otherwise mentioned.

The $K^P = 0^+$ projection of ξ_0 lowers the energy down to -397.3 MeV. The energy obtained by projecting this $K^P = 0^+$ state further onto $J^P = 0^+$ turns out to be -399.3 MeV. In other words, the K^P projection lowers the energy by 5.7 MeV, while the J -projected energy is less than 2 MeV away.













Euler angle γ	0	$\pi/4$	$\pi/2$	$3\pi/4$
state				
(a) $K = 0$	$\Phi \propto$ 	$+ \dots +$ 	$+ \dots +$ 	$+ \dots +$ 
(b) $K = 2$	$\Phi \propto$ 	$+ \dots + i$ 	$+ \dots -$ 	$+ \dots - i$ 
(c) $K = -2$	$\Phi \propto$ 	$+ \dots - i$ 	$+ \dots -$ 	$+ \dots + i$ 
Expectation value of H				
(d) $K = 0$ (diagonal)				
$\langle K=0 H K=0 \rangle \propto \langle \text{horizontal ellipse} H \text{horizontal ellipse} \rangle + \dots + \langle \text{horizontal ellipse} H \text{vertical ellipse} \rangle + \dots + \langle \text{horizontal ellipse} H \text{vertical ellipse} \rangle$ $+ \dots + \langle \text{horizontal ellipse} H \text{vertical ellipse} \rangle + \dots +$				
(e) $K = 2 + K = -2$ (diagonal)				
$\langle K=2 \& -2 H K=2 \& -2 \rangle \propto \langle \text{horizontal ellipse} H \text{horizontal ellipse} \rangle + \dots + 0 \langle \text{horizontal ellipse} H \text{vertical ellipse} \rangle + \dots - \langle \text{horizontal ellipse} H \text{vertical ellipse} \rangle$ $+ \dots + 0 \langle \text{horizontal ellipse} H \text{vertical ellipse} \rangle + \dots +$				

FIG. 6. Schematic illustrations of K-projected states

We stress that any state with $\gamma=0^\circ$ remains the same by the rotation about the z axis, implying $|\phi\rangle = |e^{i\gamma J_z} \phi\rangle$ [55]. The resultant absence of couplings between different states means that there is no way to generate additional binding energy. In the example case, if the state ξ_0 were not triaxial at all, the K projection would yield no effect, meaning no binding energy gain. Thus, the triaxiality may not be treated properly unless the K projection is included. In the present case, the ξ_0 state is taken from the MCSM calculation, where the K -projection is implemented, and thereby this problem does not occur. However, if one starts from mean-field approach without K projection, a false solution likely emerges.

In order to see how a triaxial intrinsic state appears, we carry out an HFB calculation for the same Hamiltonian. Although the HFB approach may not provide very accurate solutions, we can grasp certain aspects relatively easily. The HFB calculation is performed only with the projection for the particle numbers, and the projected energies shown below are calculated after the variation (like VBP) for parity, K and J .

Figure 7 shows the dependence of the calculated energies

on the deformation parameter γ : its value is varied as a constraint to the HFB calculation, while another deformation parameter β_2 is fixed to the value of the minimum point. The unprojected energy only with the parity projection is basically flat from $\gamma=0^\circ$ up to $\gamma \sim 10^\circ$. The state projected onto $K^P=0^+$ captures additional binding through the mechanism presented above with Fig. 6 (d), and exhibits the energy minimum located around $\gamma=10^\circ$. The additional binding gives a definite impact in drawing the shape of the nucleus, with the pronounced energy minimum around $\gamma=10^\circ$. This γ value is in good agreement with the one from the T-plot. Figure 7 shows that the additional binding is saturated beyond $\gamma \sim 10^\circ$, and the unprojected and K -projected energies are raised in parallel. Figure 7 also depicts that further projection onto $J^P=0^+$ basically lowers the K -projected energies by about the same amount up to $\gamma=40^\circ$, and that it does not change the location of the energy minimum. Thus, for the location of the minimum, the K projection is really crucial, and the induced shift of the γ value at the energy minimum implies that the intrinsic structure and the restoration of rotational symmetry is not

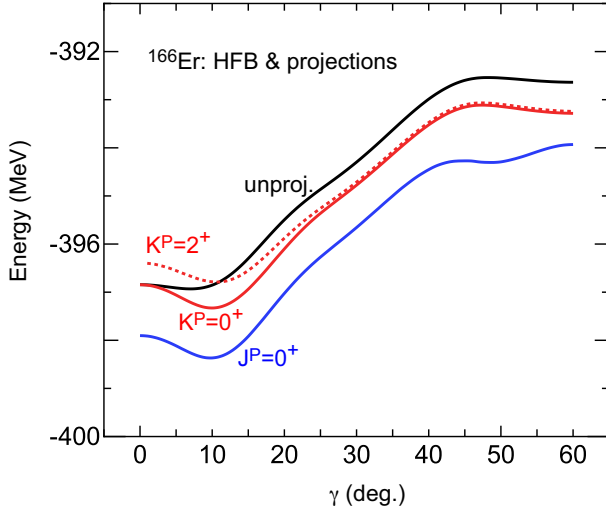


FIG. 7. Energies of the ground state of ^{166}Er given by HFB calculations as a function of deformation parameter γ (deg.) as a constraint. The energies are given by (black solid line) unprojected, (red solid line) K projected, and (blue solid line) J projected calculations. The particle number is projected before variation, while parity, K and J are projected after the variation. The $K^P=2^+$ energies are shown by red dotted line. Deformation parameter β_2 is fixed to the minimum point with actual value $\beta_2=0.30$.

decoupled.

4.3. $K^P = 2^+$ cases

The case of $K^P = 2^+$ is slightly more complicated, as both $K^P = +2^+$ and $K^P = -2^+$ must be considered because of time reversal symmetry in stationary states. As the parity projection is included unless otherwise stated, the parity is not displayed in some of the positive-parity cases, for the sake of brevity. Figure 6 (b) ((c)) depicts how the superposition of rotated ϕ occurs for $K = 2$ ($K = -2$). The multiplication factor becomes imaginary at Euler angle $\gamma = \pi/4$, and is negative at $\gamma = \pi/2$. So, around $\gamma = \pi/2$, the multiplication factors of $K = \pm 2$ projections show opposite signs to those of $K = 0$.

The expectation value of the Hamiltonian is evaluated similarly to the $K=0$ projection. We take equally-weighted linear combination of normalized K -projected states, $|K = 2\rangle$ and $|K = -2\rangle$: $\tilde{\Phi}[\phi, K] = (|K = 2\rangle + |K = -2\rangle)/\sqrt{2}$, and define

$$\begin{aligned} \tilde{h}_K &= \langle \tilde{\Phi}[\phi, K] | H | \tilde{\Phi}[\phi, K] \rangle \\ &\propto \int_0^{2\pi} d\gamma \cos(K\gamma) \langle \phi | H | e^{i\gamma J_z} \phi \rangle. \end{aligned} \quad (13)$$

The Hamiltonian does not couple a state of $K=K_1$ with a state of $K=K_2$ if $K_1 \neq K_2$. Because of time-reversal symmetry, in the example of $K = \pm 2$, the values of $\langle K = 2 | H | K = 2 \rangle$ and $\langle K = -2 | H | K = -2 \rangle$ should be the same or approximately so, if $|\phi\rangle$ generates a dominant component of the state of interest. This means $\tilde{h}_K \sim \langle K = 2 | H | K = 2 \rangle \sim \langle K = -2 | H | K = -2 \rangle$. Figure 6 (e) displays the contributions to $\tilde{h}_{K=2}$ from selected

values of the Euler angle γ . We find a vanished contribution at $\gamma = \pi/4$ (cf. $\cos(\pi/2)=0$) and a contribution opposite to the one for $K = 0$ at $\gamma = \pi/2$ (cf. $\cos(\pi)=-1$). This means that the $K = \pm 2$ projections yield no additional binding energy from the contributions at $\gamma = \pi/4$, and that the contribution at $\gamma = \pi/2$ even diminishes the binding energy. Thus, the triaxiality generally decreases the binding energy gains of the $K = \pm 2$ states compared to that of the $K = 0$ state, locating $K = \pm 2$ states above $K = 0$ state. This effect is concretely discussed in the next section.

This energy splitting is reduced in general, if the triaxiality becomes stronger. This is because for stronger triaxiality, $\langle \phi | H | e^{i\gamma J_z} \phi \rangle$ and $\langle \phi | e^{i\gamma J_z} \phi \rangle$ reduce faster as Euler angle γ moves away from 0. The faster reduction implies smaller differences of $K=0$ result from $K = \pm 2$ results, as exemplified in Subsec. 5.6. This is one of the reasons why the ξ_3 basis vector is better than ξ_0 basis vector as a single basis vector for calculating the energy of the 3_1^+ (and also 2_2^+) state of ^{166}Er .

4.4. Relation to symmetry restoration and other remarks

Coming back to general aspects, the K projection of triaxial intrinsic state can be viewed from the symmetry restoration. The triaxial intrinsic state has a particular orientation in the xy plane, which violates the rotational symmetry about the z axis. This symmetry is restored by rotating the intrinsic state about the z axis, as shown in the previous two subsections, so that the z -component of the angular momentum takes an integer K . As such K value is conserved to a good approximation (exactly in some cases) for strongly deformed nuclei as discussed later, it is a transparent and appropriate way to treat K as a conserved quantum number. We stress that this restoration mechanism is independent of actual nuclear forces. In other words, the energy of such symmetry-restored state is a superposition of matrix elements of nuclear forces, and the weight factor is not determined by the forces but by the quantum-mechanical rotation procedure, in contrast to eigenvalue problems. This feature makes the significance of the K projection robust.

We note that the MCSM calculation naturally includes possible K mixings in the eigen solutions, independently of the amount of the mixing.

A systematic survey in terms of the Skyrme Hartree-Fock calculation indicated the dominance of the prolate nuclear shapes [94]. The universal finite-range liquid-drop model (FRLDM) similarly predicted no triaxial ground states for the deformed nuclei being discussed (see Fig. 2 of Ref. [16] as mentioned earlier). These are examples of the conventional picture for the deformed nuclear shapes of heavy nuclei, where the properties of unprojected states were discussed. Naturally, the triaxiality brought in by K projection was absent.

The matrix element $\langle \Phi[\phi, K=0] | H | \tilde{\Phi}[\phi, K=2] \rangle$ vanishes because of different K values between bra and ket vectors. When the total angular momentum J is restored as discussed in the next section, this property is broken. This breaking, however, is rather small with strong deformation and vanishes at the limit of extremity.

Some details of the K projection will be given in Appendix C.

5. A QUANTUM THEORY OF THE ROTATION OF MULTI-NUCLEON SYSTEM

After the discussions of the crucial consequence of the K projection, it is worth showing how the excitation energy at the rotor limit (see eq. (3)) is obtained within the quantum many-body framework, without resorting to the quantization of the free rotational motion of a classical rigid body.

5.1. Formulation

We here discuss the projection onto a good J value. The state ϕ_0 is assumed to be a $K=0$ and normalized intrinsic state, from which J -states are projected out. The state ϕ_0 is actually the state discussed in the previous section. The state ϕ_0 is assumed to be of positive parity for simplicity, while the parity projection does not affect the following formulation.

Based on eq. (8), we consider J -projected matrix elements and overlaps. Because of the rotational invariance of the Hamiltonian, M can be taken to be 0 without losing the generality. The norm of the J -state component (with $M=0$) contained in ϕ_0 is given by,

$$\begin{aligned} |\mathcal{N}_J|^2 &= \frac{2J+1}{8\pi^2} \int_0^{2\pi} d\alpha \int_0^\pi d\beta \sin\beta \int_0^{2\pi} d\gamma \\ &\quad \langle \phi_0 | \{ D_{0,0}^J(\alpha, \beta, \gamma) \}^* e^{i\alpha \hat{J}_z} e^{i\beta \hat{J}_y} e^{i\gamma \hat{J}_z} | \phi_0 \rangle \\ &= \frac{2J+1}{2} \int_0^\pi d\beta \sin\beta d_{0,0}^J(\beta) \langle \phi_0 | e^{i\beta \hat{J}_y} | \phi_0 \rangle, \end{aligned} \quad (14)$$

where it is considered that ϕ_0 is a $K=0$ state and the bra state is ϕ_0 which is an $M=0$ state.

We introduce the norm kernel,

$$n_y(\beta) = \langle \phi_0 | e^{i\beta \hat{J}_y} | \phi_0 \rangle. \quad (15)$$

Although this quantity is a complex number for a general state, here it is a real number because of $K, M = 0$ for $|\phi_0\rangle$. Equation (14) becomes

$$|\mathcal{N}_J|^2 = \frac{2J+1}{2} \int_0^\pi d\beta \sin\beta d_{0,0}^J(\beta) n_y(\beta). \quad (16)$$

Similarly, the expectation value of the Hamiltonian H for a projected state is given by

$$\begin{aligned} E_J &= \frac{2J+1}{2|\mathcal{N}_J|^2} \int_0^\pi d\beta \sin\beta \langle \phi_0 | H d_{0,0}^J(\beta) e^{i\beta \hat{J}_y} | \phi_0 \rangle, \\ &= \frac{2J+1}{2|\mathcal{N}_J|^2} \int_0^\pi d\beta \sin\beta d_{0,0}^J(\beta) h_y(\beta), \end{aligned} \quad (17)$$

where the energy kernel is introduced as,

$$h_y(\beta) = \langle \phi_0 | H e^{i\beta \hat{J}_y} | \phi_0 \rangle. \quad (18)$$

The following identity is known

$$d_{0,0}^J(\beta) = P_J(\cos\beta), \quad (19)$$

where $P_J(\cos\beta)$ stands for a Legendre function. The $P_J(\cos\beta)$ function satisfies

$$\frac{d}{d(\cos\beta)} \left\{ (1 - \cos^2\beta) \frac{d}{d(\cos\beta)} P_J(\cos\beta) \right\} + J(J+1) P_J(\cos\beta) = 0. \quad (20)$$

We now restrict ourselves to $\beta \approx 0$, because the values of $n_y(\beta)$ and $h_y(\beta)$ are reduced quickly as β moves away from 0 as a consequence of strong deformation. At the limit of $\beta \rightarrow 0$, eq. (20) produces the derivative at $\beta = 0$,

$$\left. \frac{d}{d(\cos\beta)} P_J(\cos\beta) \right|_{\beta=0} = \frac{J(J+1)}{2}, \quad (21)$$

from which we obtain a linear approximation near $\beta = 0$

$$P_J(\cos\beta) \approx 1 + F_J(\cos\beta - 1) \quad \text{for } \beta \approx 0, \quad (22)$$

with

$$F_J = J(J+1)/2. \quad (23)$$

The function $d_{0,0}^J(\beta) = P_J(\cos\beta)$ in eqs. (16) and (17) is now approximated by this function.

The range of β runs from 0 to π . Sizable contributions to the quantities in eqs. (16) and (17) are also expected for β close to π , as the overlap is generally restored. For $\beta \sim \pi$, the linear and other approximations starting from $\beta = \pi$ back to smaller values work well also. These contributions can be evaluated in the same way as those from $\beta \sim 0$. Although they will not be explicitly discussed, they will be included in actual cases to be presented.

We define

$$n_0 = \int d(\cos\beta) n_y(\beta), \quad (24)$$

and

$$n_1 = \int d(\cos\beta) n_y(\beta) (\cos\beta - 1). \quad (25)$$

Likewise, similar quantities for the Hamiltonian are defined as

$$e_0 = \int d(\cos\beta) h_y(\beta), \quad (26)$$

and

$$e_1 = \int d(\cos\beta) h_y(\beta) (\cos\beta - 1). \quad (27)$$

The projected energy of the state of J is then given by

$$E_J \approx \frac{e_0 + F_J e_1}{n_0 + F_J n_1}, \quad (28)$$

which produces the excitation energies from the $J=0$ state,

$$E_J - E_0 \approx \frac{F_J(e_1 n_0 - e_0 n_1)}{(n_0 + F_J n_1) n_0}. \quad (29)$$

5.2. Contributions of leading and next-to-leading orders

The quantities n_0 and e_0 are averages over the range of $\cos\beta$, and are relevant to the $J = 0$ ground state as $P_{J=0}(\cos\beta) = 1$. As n_y and h_y are reduced quickly as β moves away from $\beta = 0$ (also from $\beta = \pi$), the magnitudes of n_1 and e_1 are smaller, respectively, than n_0 and e_0 , due to the factor, $\cos\beta - 1$. We introduce n_k and e_k ,

$$n_k = \int d(\cos\beta) n_y(\beta) (\cos\beta - 1)^k, \text{ for } k = 2, 3, \dots, \quad (30)$$

and

$$e_k = \int d(\cos\beta) h_y(\beta) (\cos\beta - 1)^k, \text{ for } k = 2, 3, \dots \quad (31)$$

The magnitudes of n_2 and e_2 are smaller, respectively, than $|n_1|$ and $|e_1|$, and this trend may remain for certain higher k 's. We then evaluate contributions of n_k 's and e_k 's ($k=0, 1, 2$) according to the order k , with the order of their product being the sum of the order of individual n_k or e_k . The leading-order (LO) contribution is given by e_0/n_0 (see eq. (28)) for the states of all J values to be considered. It is also the exact J -projected energy of the $J=0$ state, $E_{J=0}$.

The excitation energy of the state with J (see eq. (29)) is given in the next-to-leading order (NLO) of $(\cos\beta - 1)$ by

$$E_x^{(k=1)}(J) = \frac{F_J(e_1 n_0 - e_0 n_1)}{n_0^2}, \quad (32)$$

where the $F_J n_1/n_0$ term in the denominator of eq. (29) is dropped off because the numerator of eq. (29) is already of the NLO, and n_0 in the denominator is of the LO. Eq. (32) is rewritten as

$$E_x^{(1)}(J) = \frac{1}{2} J(J+1) \frac{e_0}{n_0} \left\{ \frac{e_1}{e_0} - \frac{n_1}{n_0} \right\}. \quad (33)$$

Note that at the LO, $E_x^{(0)}(J) = 0$, as stated above.

The quantity n_0 is positive near $\beta=0$, where n_1 is negative. As h_y represents attractions from nuclear forces, e_0 is negative, and e_1 is positive. As β increases from zero, both $n_y(\beta)$ and $h_y(\beta)$ damp, but $h_y(\beta)$ damps more slowly than $n_y(\beta)$ does, because the Hamiltonian can connect two states oriented at more different angles. This difference is expected to and indeed does result in an inequality $|e_1/e_0| > |n_1/n_0|$, while e_1/e_0 and n_1/n_0 are both negative. Combining all these features, the quantity after $J(J+1)$ in eq. (33) becomes positive. Thus, a perfect rotational excitation energy emerges. Equation (33) indicates that rotational excitation energies are generated by the Hamiltonian including nuclear forces. This feature is robust and general. For instance, the nuclear force does not have to be of any particular types and can include various terms even three-nucleon forces, for instance. What is needed is a strongly deformed state in the body-fixed frame shared by members of the band.

The present picture exhibits the ‘‘quantum mechanical rotation’’ of the nucleus. The state observed in the laboratory is a superposition of this object pointing to different angular

orientations. The angular momentum, as a conserved quantum number, defines how the superposition occurs, and the multiplication factor for the $(\cos\beta - 1)$ term indeed follows the $J(J+1)$ gradient. This superposition provides us, in ideal cases, with the exact $J(J+1)$ excitation spectrum within a given rotational band.

The origin of the rotational spectrum is the coupling between the same intrinsic state in two different angular orientations, originating in interactions between constituents (nucleons for atomic nuclei). This is not the same as the increase of the kinetic energy of the free rotation of a rigid body in the conventional picture. In the present view, the nuclear forces create a deformed intrinsic state, require the restoration of the rotational symmetry, and consequently produce the (nearly) $J(J+1)$ excitation spectrum, irrespectively of details of dynamics.

5.3. Contributions of next-to-next-to-leading order

The Legendre function can be expanded for $\beta \approx 0$ up to $(\cos\beta - 1)^2$ as

$$P_J(\cos\beta) \approx 1 + F_J(\cos\beta - 1) + G_J(\cos\beta - 1)^2. \quad (34)$$

The coefficient G_J is given as

$$G_J = \frac{1}{16} J(J-1)(J+1)(J+2) = \frac{1}{16} \left\{ (J(J+1))^2 - 2J(J+1) \right\}, \quad (35)$$

as proven by expanding $P_J(x)$ in terms of the polynomials of $(x-1)$.

The projected energy of the state of J is then given by

$$E_J = \frac{e_0 + F_J e_1 + G_J e_2}{n_0 + F_J n_1 + G_J n_2}, \quad (36)$$

with the excitation energies from the $J=0$ state,

$$E_J - E_0 = \frac{F_J(e_1 n_0 - e_0 n_1) + G_J(e_2 n_0 - e_0 n_2)}{(n_0 + F_J n_1 + G_J n_2) n_0}. \quad (37)$$

Expanding the denominator in terms of NLO term n_1/n_0 and next-to-next-to-leading order (NNLO) term n_2/n_0 , we obtain the NNLO term from eq. (37),

$$\begin{aligned} E_x^{(2)}(J) &= F_J^2 \frac{n_1}{n_0} \left\{ \frac{e_0 n_1}{n_0^2} - \frac{e_1}{n_0} \right\} + G_J \frac{e_0}{n_0} \left\{ \frac{e_2}{e_0} - \frac{n_2}{n_0} \right\}, \\ &= -F_J E_x^{(1)}(J) \frac{n_1}{n_0} + G_J \frac{e_0}{n_0} \left\{ \frac{e_2}{e_0} - \frac{n_2}{n_0} \right\}. \end{aligned} \quad (38)$$

The first term in the RHS is positive and raises the excitation energies, while the second term is likely negative and lowers the excitation energies.

It is worth pointing that as the two terms of the RHS of eq. (38) cancel each other to a large extent, a large fraction of the remaining effects includes the $J(J+1)$ dependence because of $J^2(J+1)^2 - J(J-1)(J+1)(J+2) = 2J(J+1)$.

It is also emphasized that the effects at the NNLO are expressed by the two terms, $J(J+1)$ and $\{J(J+1)\}^2$. This finding seems to be related to various empirical fits not only for nuclei but also for molecules [7].

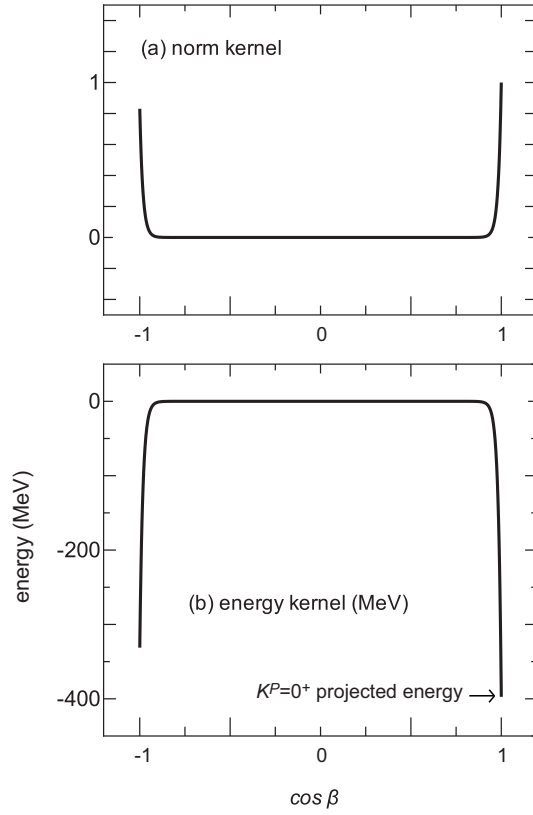


FIG. 8. (a) norm kernel and (b) energy kernel as functions of the $\cos \beta$. The case of ^{166}Er is taken.

5.4. Verification Examples

Figure 8 shows the norm and energy kernels, n_y and h_y , as functions of $\cos \beta$ for the ξ_0 state for ^{166}Er . The damping as $\cos \beta$ deviates from 1 or -1 is shown to be fast as anticipated, while a closer look indicates that the damping is slower for the energy kernel in panel (b) than for the norm kernel in panel (a). We point out that the energy at $\cos \beta = 1$ (i.e., $\beta = 0$) in Fig. 8 (b) is the energy obtained by the $K=0$ projection (-397.348 MeV) discussed in the previous section. The energy comes further down for lower J values (certainly for $J=0$) by restoring the quantum number, J .

In this figure, the reflection symmetry with respect to $\cos \beta = 0$ appears to a good extent, although this is not guaranteed with realistic NN interactions. It is pointed out that the figure is for one selected basis vector ξ_0 (see Subsec. 3.4), but this symmetry is already fulfilled rather well, in accordance to the assumption of collective models.

Table I depicts the values of various quantities discussed in this section. The values are obtained with the ξ_0 state introduced in Subsec. 3.4 for ^{166}Er . In later section, we will discuss the feature of ^{154}Sm ($Z=62$, $N=92$). Table I includes the values obtained for ^{154}Sm , which will be discussed later.

Table I exhibits the rapid damping from n_0 to n_2 and that from e_0 to e_2 . The binding energy gain due to the couplings among different angles β evaluated by the J^π projection amounts to about 2 MeV, which is quite significant. The next-

TABLE I. Examples of ground-state rotational bands. Energies are in MeV.

quantity \ nucleus	^{166}Er	$^{154}\text{Sm } 0_1^+$
n_1 / n_0	-0.01731	-0.01654
n_2 / n_0	0.00061	0.00056
e_1 / e_0	-0.01736	-0.01661
e_2 / e_0	0.00061	0.00056
energy of ϕ_0	-397.35	-319.32
energy of $J^\pi=0^+$ state	-399.30	-321.30
$\text{Ex}^{(1)} (J=2^+)$	0.0644	0.0622
$(J=4^+)$	0.2147	0.2072
$(J=6^+)$	0.4510	0.4351
$\text{Ex}^{(2)} (J=2^+)$	0.0011	0.0010
$(J=4^+)$	0.0037	0.0029
$(J=6^+)$	0.0076	0.0046
	NNLO	exact proj.
$\text{Ex}^{(T)} (J=2^+)$	0.0655	0.0655
$(J=4^+)$	0.2184	0.2182
$(J=6^+)$	0.4586	0.4572
$\text{Ex}(J=4^+) / \text{Ex}(J=2^+)$	3.333	3.326
$\text{Ex}(J=6^+) / \text{Ex}(J=2^+)$	6.997	6.962

to-leading order excitation energies are shown to dominate the excitation energies. The excitation energies up to the NNLO are in good agreement with the corresponding exact (or direct) projection.

It is of interest, in which situation $E_x(4_1^+)/E_x(2_1^+)=3$ may arise, as this is a possible border value for differentiating strongly deformed nuclei, as has been adopted in this paper. A similar question can be raised for $E_x(4_1^+)/E_x(2_1^+)=2.5$, which is more like the border to so-called gamma-soft nuclei, maybe combined with a proper criterion for other excited states. By applying and extending the present ideas, we will be able to find solutions to those questions.

5.5. Finite K values

The formulation for the $K=0$ rotational band can be generalized to rotational bands with finite K values with certain formal complexities. The final result of this subsection is shown in eq. (64), which appears to be very simple and useful. Even if one skips detailed derivation and jumps into eq. (64), it does not prevent from understanding the rest of this paper. We keep the derivation however, as it indicates some interesting and essential features of the collective motion.

We mainly discuss the case of $K=2$, as other cases can be treated in the same way. The wave function of the intrinsic state, from which relevant states are projected out, is supposed to have an invariance property with respect to angle- π rotation about the y axis,

$$|\phi\rangle = e^{i\pi J_y} |\phi\rangle. \quad (39)$$

If not, it can be achieved by redefining $|\phi\rangle$ by $|\phi\rangle + e^{i\pi J_y} |\phi\rangle$ with a proper normalization. Note that the $J=0$ -projected state remains unchanged by this substitution, as this superposition is a part of the J -projection.

As stated in Sec. 4, $K=2$ projection involves the projections onto $K=2$ and $K=-2$ subspaces. The parity is always positive here and is not explicitly specified hereafter. We introduce $|\phi_K\rangle$ denoting the state projected from ϕ onto K (see eq. (10)):

$$|\phi_K\rangle = \frac{1}{2\pi} \int_0^{2\pi} d\gamma e^{i\gamma(\hat{J}_z-K)} |\phi\rangle. \quad (40)$$

This is a part of the process shown in eq. (8). The π rotation about the y -axis of ϕ_K is expressed as

$$\begin{aligned} e^{i\pi\hat{J}_y} |\phi_K\rangle &= \frac{1}{2\pi} \int_0^{2\pi} d\gamma \left\{ e^{i\pi\hat{J}_y} e^{i\gamma(\hat{J}_z-K)} e^{-i\pi\hat{J}_y} \right\} \left\{ e^{i\pi\hat{J}_y} |\phi\rangle \right\} \\ &= \frac{1}{2\pi} \int_0^{2\pi} d\gamma \left\{ e^{i\gamma(-\hat{J}_z-K)} \right\} \left\{ e^{i\pi\hat{J}_y} |\phi\rangle \right\} \\ &= \frac{1}{2\pi} \int_0^{2\pi} d\gamma e^{i\gamma(\hat{J}_z+K)} |\phi\rangle = |\phi_{-K}\rangle, \end{aligned} \quad (41)$$

implying that ϕ_K and ϕ_{-K} are exchanged in this rotation.

The state of J , $M(=J_z)$ projected from the K component of ϕ is expressed, with the projection operator $\mathcal{P}_{J,M,K}$, as

$$|J, M, K\rangle = \mathcal{P}_{J,M,K} |\phi\rangle, \quad (42)$$

with

$$\mathcal{P}_{J,M,K} = \frac{2J+1}{8\pi^2} \int_0^{2\pi} d\alpha \int_0^\pi d\beta \sin\beta \int_0^{2\pi} d\gamma \left\{ D_{M,K}^J(\alpha, \beta, \gamma) \right\}^* e^{i\alpha\hat{J}_z} e^{i\beta\hat{J}_y} e^{i\gamma\hat{J}_z}, \quad (43)$$

where a Wigner function $D_{M,K}^J(\alpha, \beta, \gamma)$ is shown in eq. (9). These two equations combined are essentially the same as eq. (8), but the operator $\mathcal{P}_{J,M,K}$ is explicitly introduced for later purposes. The state in eq. (42) is then rewritten as

$$\begin{aligned} |J, M, K\rangle &= \frac{1}{2\pi} \int_0^{2\pi} d\alpha e^{i\alpha(\hat{J}_z-M)} \frac{2J+1}{2} \int_0^\pi d\beta \sin\beta d_{M,K}^J(\beta) e^{i\beta\hat{J}_y} \\ &\quad \frac{1}{2\pi} \int_0^{2\pi} d\gamma e^{i\gamma(\hat{J}_z-K)} |\phi\rangle, \\ &= \frac{1}{2\pi} \int_0^{2\pi} d\alpha e^{i\alpha(\hat{J}_z-M)} \frac{2J+1}{2} \int_0^\pi d\beta \sin\beta d_{M,K}^J(\beta) e^{i\beta\hat{J}_y} |\phi_K\rangle. \end{aligned} \quad (44)$$

We point out that the state $|J, M, K\rangle$ is obtained simply by the projection, and is not normalized. All $|J, M, K\rangle$ states have the same (J, M) quantum numbers with different origins specified by K values. There is no orthogonality in general between $|J, M, K\rangle$ states with different K values. The integer K can be interpreted as a kind of additional quantum number.

It is now of interest to look into the relation between $|J, M, K\rangle$ and $|J, M, -K\rangle$. The latter is given by

$$\begin{aligned} |J, M, -K\rangle &= \frac{1}{2\pi} \int_0^{2\pi} d\alpha e^{i\alpha(\hat{J}_z-M)} \frac{2J+1}{2} \int_0^\pi d\beta \sin\beta d_{M,-K}^J(\beta) e^{i\beta\hat{J}_y} \end{aligned}$$

$$\begin{aligned} &\frac{1}{2\pi} \int_0^{2\pi} d\gamma e^{i\gamma(\hat{J}_z+K)} |\phi\rangle, \\ &= \frac{1}{2\pi} \int_0^{2\pi} d\alpha e^{i\alpha(\hat{J}_z-M)} \frac{2J+1}{2} \int_0^\pi d\beta \sin\beta d_{M,-K}^J(\beta) e^{i\beta\hat{J}_y} |\phi_{-K}\rangle. \end{aligned} \quad (45)$$

The d function in the integral can be transformed as

$$d_{M,-K}^J(\beta) = d_{-K,M}^J(-\beta) = (-1)^{J-M} d_{M,K}^J(\pi - \beta). \quad (46)$$

The integral with β is then rewritten as

$$\int_0^\pi d\beta \sin\beta (-1)^{J-M} d_{M,K}^J(\pi - \beta) e^{i\beta\hat{J}_y} |\phi_{-K}\rangle, \quad (47)$$

By substituting $(\pi - \beta)$ with β' , this integral becomes

$$\begin{aligned} &\int_0^\pi d\beta' \sin\beta' (-1)^{J-M} d_{M,K}^J(\beta') e^{i(\pi-\beta')\hat{J}_y} |\phi_{-K}\rangle, \\ &= \int_0^\pi d\beta' \sin\beta' (-1)^{J-M} d_{M,K}^J(\beta') e^{-i\beta'\hat{J}_y} |\phi_K\rangle, \end{aligned} \quad (48)$$

where eq. (41) is used. The \hat{J}_y operator comprises angular-momentum raising, \hat{J}_+ , and lowering, \hat{J}_- , operators, and always changes the value of J_z by one unit. Both $e^{i\beta'\hat{J}_y}$ and $e^{-i\beta'\hat{J}_y}$ connect the state of M to the state of K and *vice versa*, because they contain, in their expanded forms, the \hat{J}_y operator from the 0-th up to infinite powers. The terms contributing to this connection includes the $|K-M|$ -power of \hat{J}_y multiplied by various even-power \hat{J}_y terms. In comparison between the contributions of $e^{i\beta'\hat{J}_y}$ and $e^{-i\beta'\hat{J}_y}$, the difference is represented by a single phase factor $(-1)^{K-M}$. Thus, the integral in eq. (48) is rewritten as

$$\int_0^\pi d\beta' \sin\beta' (-1)^{J-K} d_{M,K}^J(\beta') e^{i\beta'\hat{J}_y} |\phi_K\rangle. \quad (49)$$

Putting this integral back to eq. (45), we obtain

$$|J, M, -K\rangle = (-1)^{J-K} |J, M, K\rangle. \quad (50)$$

This equation clearly indicates that the state $(-1)^{J-K} |J, M, -K\rangle$ is identical to $|J, M, K\rangle$. We stress that, for the ‘‘additional (approximate) quantum number K ’’, $K < 0$ are redundant, and $K \geq 0$ are sufficient. We shall refer only to $K \geq 0$ hereafter.

The present formulation is consistent with the conventional approach (see, for instance, [4]), with the state,

$$\Omega_{M,K}^J \propto \left\{ |J, M, K\rangle + (-1)^{(J+K)} |J, M, -K\rangle \right\}, \quad (51)$$

where J and K are assumed to be integers. As this state is built on a general intrinsic state without the symmetry in eq. (39), the phase factor $(-1)^{(J+K)}$ is needed to make the state unchanged against the π -rotation about the y axis in the body-fixed frame. This phase factor $(-1)^{(J+K)}$ makes the expression in eq. (51) invariant also with respect to the time reversal operation in the body-fixed frame. The state of J and M is changed by the time-reversal operation, but its emerging

mechanism defined in the body-fixed frame is supposed to be time-reversal invariant. The same argument holds for the rotation about the y -axis in the body-fixed frame. As mentioned already, this phase factor is not necessary in the present work.

In order to obtain the energy of the state $|J, M, K\rangle$, $M=K$ can be taken without losing the generality, because the energy does not depend on M . The energy of $|J, K, K\rangle$ is then written as

$$E_{J,K} = \frac{\langle \phi | H \mathcal{P}_{J,K,K} | \phi \rangle}{\langle \phi | \mathcal{P}_{J,K,K} | \phi \rangle}. \quad (52)$$

Note that the K dependence originates in the K projection of the state ϕ in the body-fixed frame, and this K dependence naturally remains in the following arguments. We now calculate the numerator and denominator. The latter is given by

$$\begin{aligned} & \langle \phi | \mathcal{P}_{J,K,K} | \phi \rangle \\ &= \langle \phi | \frac{1}{2\pi} \int_0^{2\pi} d\alpha e^{i\alpha(\hat{J}_z - K)} \frac{2J+1}{2} \int_0^\pi d\beta \sin\beta d_{K,K}^J(\beta) e^{i\beta\hat{J}_y} | \phi_K \rangle \\ &= \frac{2J+1}{2} \langle \phi_K | \int_0^\pi d\beta \sin\beta d_{K,K}^J(\beta) e^{i\beta\hat{J}_y} | \phi_K \rangle. \end{aligned} \quad (53)$$

We generalize the definition of norm kernels from eq. (15) to

$$n_y^{(K)}(\beta) = \langle \phi_K | e^{i\beta\hat{J}_y} | \phi_K \rangle. \quad (54)$$

The norm kernel for $K=0$ is then expressed as $n_y^{(0)}(\beta)$. The individual norm fraction is denoted by

$$n_J^{(K)} = \frac{2J+1}{2} \int_0^\pi d\beta \sin\beta d_{K,K}^J(\beta) n_y^{(K)}(\beta). \quad (55)$$

Likewise, we obtain the numerator in eq. (52). For evaluating this quantity, we extend the energy kernels for $K=0$ to a more general form,

$$h_y^{(K)}(\beta) = \langle \phi_K | H e^{i\beta\hat{J}_y} | \phi_K \rangle. \quad (56)$$

The individual energy fraction is written as

$$e_J^{(K)} = \frac{2J+1}{2} \int_0^\pi d\beta \sin\beta d_{K,K}^J(\beta) h_y^{(K)}(\beta). \quad (57)$$

Equations (55) and (57) are precise, but we handle those quantities in a different way. For strongly deformed nuclei, norm and energy kernels are considered to be swiftly reduced as β moves away from $\beta=0$ or $\beta=\pi$. So, the behaviors of relevant integrands are discussed near $\beta=0$ and $\beta=\pi$. Utilizing the definition of the Wigner small d function and the Jacobi function, we expand the following small d functions near $\beta=0$ (i.e., $\cos\beta=1$) as,

$$d_{K,K}^J(\beta) = 1 + F_{J,K}(\cos\beta - 1) + (\text{higher order terms}), \quad (58)$$

with

$$F_{J,K} = \frac{1}{2} (J(J+1) - K^2). \quad (59)$$

Note that F_J in eq. (23) implies $F_{J,K=0}$. On the other hand, near $\beta=\pi$, $d_{K,K}^J(\beta)$ with $K \neq 0$ behaves in proportion to

$(\cos(\beta-\pi)-1)^K$ + higher-order terms, and thereby their contributions do not appear in the LO or NLO for $K \geq 2$. Similarly to the $K=0$ case, norms are categorized in the hierarchy of the k -th power of the $(\cos\beta - 1)$ term as,

$$\tilde{n}_k^{(K)} = \int d(\cos\beta) n_y^{(K)}(\beta) (\cos\beta - 1)^k. \quad (60)$$

where the tilde is placed in order to clearly distinguish from kernels. The corresponding quantities for the energy, $\tilde{e}_k^{(K)}$, are similarly defined, by replacing $n_y^{(K)}(\beta)$ with $h_y^{(K)}(\beta)$, as

$$\tilde{e}_k^{(K)} = \int d(\cos\beta) h_y^{(K)}(\beta) (\cos\beta - 1)^k. \quad (61)$$

with $h_y^{(K)}(\beta)$ defined in eq. (56). We will focus on the two lowest terms of $k=0$ (LO) and $k=1$ (NLO).

We obtain, up to the NLO,

$$\langle \phi | \mathcal{P}_{J,K,K} | \phi \rangle = \tilde{n}_0^{(K)} + \tilde{n}_1^{(K)} F_{J,K}. \quad (62)$$

The contributions to the energy are treated in the same way, and are represented by $\tilde{e}_0^{(K)}$ for the LO and by $\tilde{e}_1^{(K)}$ for the NLO. We thus obtain up to the NLO,

$$\langle \phi | H \mathcal{P}_{J,K,K} | \phi \rangle = \tilde{e}_0^{(K)} + \tilde{e}_1^{(K)} F_{J,K}. \quad (63)$$

Similarly to $K=0$ case, the contributions from a given order k can be obtained, and $E_{J,K}$ in eq. (52) is expressed for the LO and NLO combined as,

$$E_{J,K}^{(0+1)} = \frac{\tilde{e}_0}{\tilde{n}_0} + \frac{1}{2} \left\{ J(J+1) - K^2 \right\} \frac{\tilde{e}_0}{\tilde{n}_0} \left\{ \frac{\tilde{e}_1}{\tilde{e}_0} - \frac{\tilde{n}_1}{\tilde{n}_0} \right\}, \quad (64)$$

where the factor $F_{J,K}$ is explicitly depicted, with $J = K, K+1, K+2, \dots$. Here, $\tilde{n}_{0,1}$ and $\tilde{e}_{0,1}$ are defined in eqs. (60) and (61), respectively. The superscript K for \tilde{n} 's and \tilde{e} 's is omitted here for brevity, while they are K dependent.

This equation implies that rotational bands specified by K are built on top of the $J=K$ state with the $J(J+1)-K^2$ dependence of the excitation energy. This is exact at the NLO, and is consistent with the features shown for $K=0$ in Subsec. 5.2.

It is remarkable that such a $(J(J+1)-K^2)$ dependence is obtained within a quantum many-body scheme, without using the quantization of the classical rigid-body rotor with an intrinsic angular momentum K , as many textbooks show. It is noted that the ‘‘moment of inertia’’ of the ground band and that of other bands appear to be different in general. Although the K quantum number is not conserved exactly, the K mixing is generally suppressed rather well in strongly deformed nuclei.

We just note the contribution from the NNLO as

$$E_{J,K}^{(2)} = -(F_{J,K})^2 \frac{\tilde{e}_0}{\tilde{n}_0} \frac{\tilde{n}_1}{\tilde{n}_0} \left\{ \frac{\tilde{e}_1}{\tilde{e}_0} - \frac{\tilde{n}_1}{\tilde{n}_0} \right\} + G_{J,K} \frac{\tilde{e}_0}{\tilde{n}_0} \left\{ \frac{\tilde{e}_2}{\tilde{e}_0} - \frac{\tilde{n}_2}{\tilde{n}_0} \right\}, \quad (65)$$

where $G_{J,K}$ is defined as

$$G_{J,K} = \frac{1}{16} \left\{ (J(J+1))^2 - 2(K^2+1)J(J+1) + K^2(K^2+3) \right\}. \quad (66)$$

All terms in eq. (65) are expressed again by polynomials of $J(J+1)$.

5.6. Sketch for projected energy levels for K and J quantum numbers

We here sketch the energies of the states projected for K and J quantum numbers. The states ξ_0 and ξ_3 introduced in Subsec. 3.4 are taken. They are the most optimized single basis vectors in the MCSM calculation for $K=0$ and $K=2$ states, respectively. As already indicated, the states ξ_0 and ξ_3 show $\gamma=8.5^\circ$ and 9.8° , respectively.

These two states are symmetrized so as to fulfill the condition in eq. (39) (see the process shown below eq. (39)). We hereafter denote such symmetrized states simply as ξ_0 and ξ_3 , for the sake of brevity, except for the three unprojected energy levels as they are calculated from the original ξ_0 and ξ_3 states (i.e., no symmetry in eq. (39)). We indicate the magnitude of this symmetrization effect by noting that it lowers the energies of K^P projected states by ~ 0.7 MeV for ξ_0 .

The states $|\phi_K\rangle$ and $|\phi_{-K}\rangle$ now carry basically the same intrinsic structure. Consequently, their energies $\langle\phi_K|H|\phi_K\rangle$ and $\langle\phi_{-K}|H|\phi_{-K}\rangle$ are equal. Here, they will simply be denoted “ $K=2$ energy”, *etc.* The left part of Fig. 9 displays this energy projected from ξ_0 as well as the corresponding energies of $K=0$ and 4. It is reminded that ξ_0 is the most important basis vector of the present CI calculation for the ground state of ^{166}Er (see Subsec. 3.4). The unprojected energy (no parity projection either) is shown at the top of column **a** of Fig. 9. All other states in Fig. 9 are projected to positive parity. The projected $K=0$ energy is lowered by more than 5 MeV from the unprojected energy, as shown in column **a**. The subsequent $J=0$ projection further lowers the energy by more than 1 MeV.

Column **b** depicts the energies of the states projected to $K=2$ located about 4 MeV below the unprojected state. The $K=2$ state is projected to $J=2$ with the energy ~ 1.2 MeV above the $J=0$ level. This $J=2$ level energy is too high compared to the observed excitation energy ~ 0.8 MeV, which is shown in column **g**.

The energies of the states projected from ξ_3 are displayed in panels **d-f** of Fig. 9. Between two panels **a-c** and **d-f**, the lower energy level of a given quantum number is shown by a solid horizontal bar, while the higher one is by the dashed bar. So, the sequence of the solid bars represents the actual situation. The $J=K=2$ level energy in column **e** (solid red bar) indicates a good agreement with the experiment. Thus, the increase of the deformation parameter γ in the $K^P=2^+$ (γ) band gives a notable improvement. The CI calculations with additional basis vectors provide more accurate results, while the basic trend of the level structure remains unchanged, as exhibited in Fig. 5.

Figure 9 also displays that the excitation energies of $K=2$ and 4 states relative to the $K=0$ state are more compressed for the larger γ value (columns **d, e, f**) than those energies with the smaller γ value (columns **a, b, c**). This illustrates the γ -induced level-energy compression discussed in Subsec. 4.3.

Figure 9 exhibits the energies of $K=4$ states, which will be discussed in Subsec. 8.2 in detail.

5.7. Remarks on earlier approaches

The nuclear rotation has been extensively studied over decades from different angles. Comparatively recent overviews can be found, for example, in [56, 57] as well as in the textbook [4]. We comment on the following two works. The generator coordinate method (GCM) was applied by Peierls and Yoccoz to the rotation in [58] with the following trial wave function in the laboratory frame,

$$\Psi = \int d\theta d\phi \chi(\theta, \phi) \Phi(R_{\theta\phi}\mathbf{x}), \quad (67)$$

where θ and ϕ are angles, χ stands for the generating function to be chosen, Φ is the wave function in the body-fixed frame with many-body coordinates shown collectively by \mathbf{x} , and $R_{\theta\phi}$ means the rotation operator by angles θ and ϕ . The generating function was taken to be proportional to spherical harmonics $Y_{lm}(\theta, \phi)$ so that stationary solutions are obtained for the variational equation. Although the quantity l is discussed as if it is the angular momentum of the nucleus, the angular momentum is carried by the coordinates \mathbf{x} . So, this expression does not seem to correspond to the present work. On the other hand, as Y_{lm} happens to be equal to the function $d_{m,0}^l$, the projection onto l incidentally occurs in this expression, with no statement in [58]. This method was limited to $K=0$, and the general formula for the $J(J+1)$ - K^2 rule is outside the scope of this approach. Thus, there seems to be no idea of the application of J projection in [58]. We also demonstrated that the $J(J+1)$ rule arises exactly at the NLO in the power counting with the $(\cos\beta - 1)^k$ terms, in contrast to the arguments on the polynomial expansion of β in [58]. Nevertheless, it is somewhat of interest that the result exhibits an apparent resemblance to a part of the present results.

The so-called Kamlah expansion was introduced by Kamlah in [59] by assuming that the energy kernel h_y can be represented well by the norm kernel n_y and its derivatives with some factors adjusted at $\beta=0$. The important feature found by the present work is the difference between n_y and h_y apart from their scales (and units). In fact, in the present work, no relations between them are assumed. In this sense, the present work may not have any direct connection to the Kamlah expansion. The $J(J+1)$ - K^2 rule does not come up in the approach [59].

6. SECOND MAJOR SOURCE OF TRIAXIALITY: NUCLEAR FORCES

6.1. Introduction

We showed, in Sec. 4, that triaxial shapes arise as a consequence of the symmetry restoration represented by K quantum number. We show, in this section, that there is another source to produce the triaxiality: characteristic components of nuclear forces.

Figure 7 shows that the unprojected PES at $\gamma=10^\circ$ is as low as that at $\gamma=0^\circ$, with a shallow minimum of this PES between

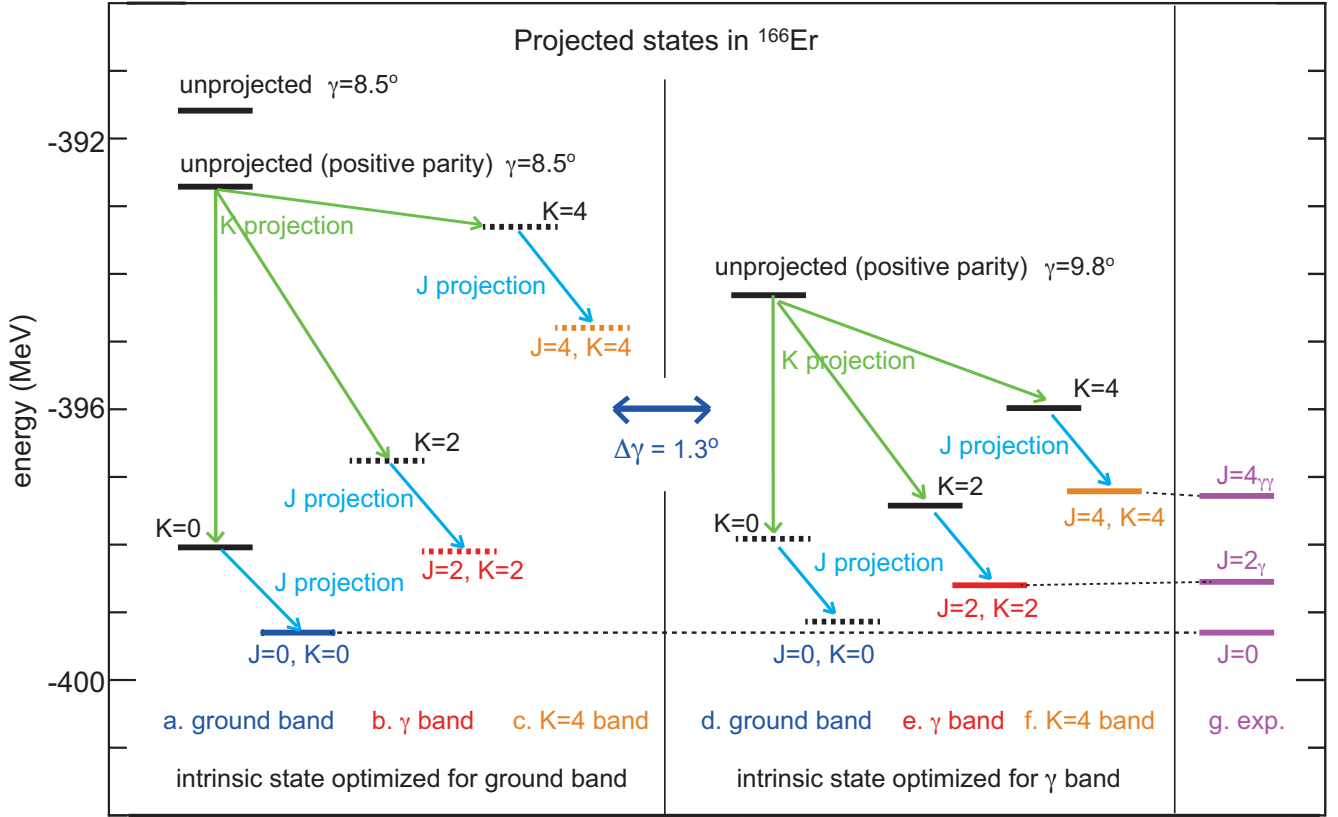


FIG. 9. Energies of projected states of ^{166}Er and related experimental level energy. All theoretical states are projected from the ξ_0 or ξ_3 state introduced in Subsec. 3.4. Parity is positive for all the states but unprojected state at the top. Columns **a** and **d** are for the ground band, columns **b** and **e** are for the γ band, and columns **c** and **f** are for the $K=4$ state. Column **g** is the observed excitation energies of 2_γ^+ and $4_{\gamma\gamma}^+$ states. Between two panels **a-c** ($\gamma=8.5^\circ$) and **d-f** ($\gamma=9.8^\circ$), the lower energy level of a given quantum number is shown by a solid horizontal bar, while the higher one by the dashed horizontal bar. Green arrows imply energy gains due to K projections, while blue arrows those due to J projections.

$\gamma=0^\circ$ and 10° . As this widely spread minimum becomes the profound minimum after the K projection, the understanding of the origin of this wide minimum is of great importance for the clarification of the triaxiality. So, we first focus on it.

A decomposition of the unprojected energy is carried out by calculating the expectation values of the proton-neutron (pn) central-force and tensor-force components of the Hamiltonian, with respect to the unprojected state specified by the deformation parameter γ as a constraint. The relative changes of their values from those at $\gamma=0^\circ$ are shown in Fig. 10a as functions of γ . The corresponding value of the rest of the Hamiltonian is also displayed. The sum of these decomposed values is nothing but the unprojected PES energy, and is also plotted by the dashed-dotted line in Fig. 10a.

Figure 10a indicates that the pn central and tensor forces produce more binding energies for $\gamma=0-15^\circ$, while the rest of the Hamiltonian works oppositely, raising the energy in the whole region of Figure 10a. We restrict ourselves to the region of $\gamma=0-15^\circ$ now. The opposite trends between the pn forces and the rest part is crucial in producing the minimum around $\gamma=7^\circ$, which is shown, in Fig. 7, as the seed of the profound minimum generated by the $K=0$ projection around $\gamma=10^\circ$.

6.2. Monopole and multipole interactions: a brief overview

In order to explore underlying mechanisms for the variations shown in Fig. 10a, we further decompose the pn central-force and tensor-force effects into their monopole and multipole contributions: A given two-body interaction, denoted by \hat{v} , can be decomposed into monopole and multipole interactions or components [60]. We here present a quick sketch of monopole interaction (for more details, see, for instance, a review [61] or a brief note [62]). When two nucleons are in single-particle orbitals j and j' , their orbital motions occur about certain axes. The monopole interaction implies averaged effect of \hat{v} over all possible axis orientations. To be more concrete, monopole matrix element is defined as

$$v_{j,j'}^{\text{mono}} = \frac{\sum_{m,m'} \langle j, m, j', m' | \hat{v} | j, m, j', m' \rangle}{\sum_{m,m'} 1}, \quad (68)$$

where m (m') refers to a magnetic quantum state of the orbital j (j'), and ket $|j, m, j', m'\rangle$ (and its bra) is normalized as usual. Thus, the monopole matrix element literally represents an average effect with respect to the angular coupling of two interacting particles. The monopole interaction between a proton

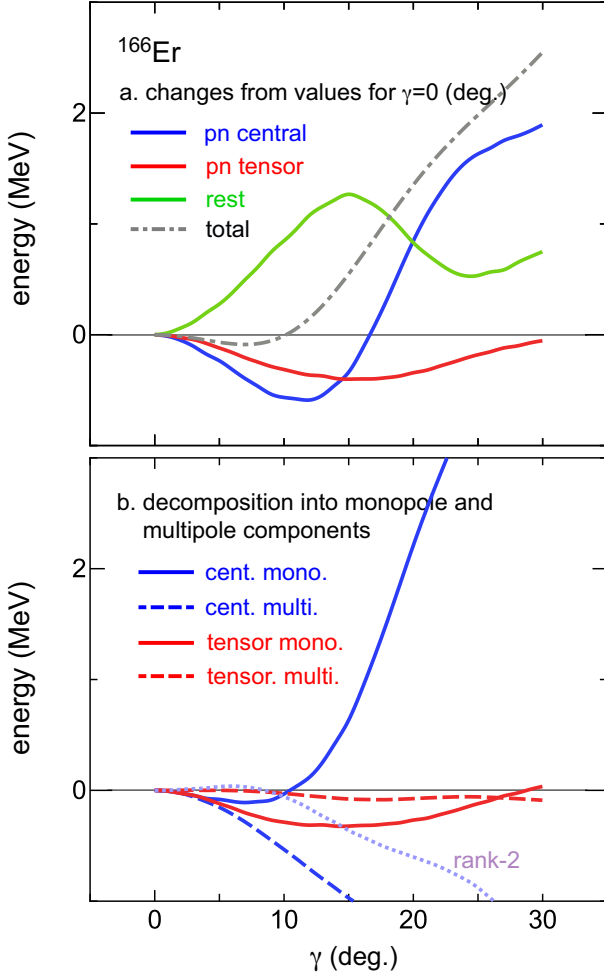


FIG. 10. Properties of the unprojected PES of ^{166}Er as a function of the deformation parameter γ as a constraint. **a.** Decomposition into contributions of proton-neutron central (blue) and tensor (red) forces and the rest (green) of the Hamiltonian. **b.** Decomposition of proton-neutron interaction effects into monopole and multipole components.

and a neutron is then expressed as

$$\hat{v}_{pn;mono} = \sum_{j,j'} v_{j,j'}^{mono} \hat{n}_j^{(p)} \hat{n}_{j'}^{(n)} \quad (69)$$

where $\hat{n}_j^{(p)}$ ($\hat{n}_{j'}^{(n)}$) denotes the number of protons in orbital j (neutrons in j'). The neutron single-particle energy (SPE) of the orbital j' is effectively shifted by $\sum_j v_{j,j'}^{mono} \hat{n}_j^{(p)}$, and vice versa. Evidently, these effects are configuration dependent or dynamically vary. If the monopole interaction is particularly strong between specific j and j' (i.e., $|v_{j,j'}^{mono}|$ is larger than many others), its impacts on the structure of the nucleus can be crucial. The monopole interaction between two protons and that between two neutrons are formulated similarly. Because of their modest effects and also for the sake of brevity, they are not explicitly discussed in this article.

The mean effects of the proton-neutron (pn) monopole interaction in eq. (69) are factorized by the occupation numbers $\langle n_j^{(p)} \rangle$ and $\langle n_{j'}^{(n)} \rangle$, where $\langle \rangle$ implies the expectation value with

respect to the state of interest. Thus, in general, monopole(-interaction) contributions can linearly grow with particle numbers in a particular orbital, and can be quite large. Note that $\langle n_j^{(p,n)} \rangle$ can reach a value of $(2j+1)$.

We next discuss the multipole interaction defined as $\hat{v}_{multi} = \hat{v} - \hat{v}_{mono}$ [60]. The multipole(-interaction) contribution does not have this linear-dependence aspect and is saturated (vanished) if the orbital is about half-filled (fully-occupied). Thus, the systematic trend of the multipole contributions differs from that of the monopole contributions.

A given pn interaction can be expressed as

$$\hat{v}_{pn} = \sum_K \hat{v}_{pn}^{(K)}, \quad (70)$$

with

$$\hat{v}_{pn}^{(K)} = \sum_{j_p, j'_p, j_n, j'_n} f_{j_p, j'_p, j_n, j'_n, K} (\hat{o}_{j_p, j'_p}^{(K)} \hat{o}_{j_n, j'_n}^{(K)}), \quad (71)$$

where K stands for angular momentum called rank, f is strength coefficient, $(\)$ means a scalar product, and j_p and j'_p (j_n and j'_n) are proton (neutron) orbitals. Here, $\hat{o}_{j,j'}^K$ implies the unit operator that annihilates a nucleon in the orbital j' and creates a nucleon in the orbital j with angular momentum K transferred from j' to j . (As the parity, $P = \pm 1$, can be transferred, K implicitly includes it.) The $K=0^+$ part, $\hat{v}_{pn}^{(K=0^+)}$, is equal to the monopole interaction if the summation in eq. (71) is restricted to $j=j'$ including all possible additional quantum numbers. This condition is actually fulfilled in the present orbitals, as in many other studies. If so, the pn multipole interaction is given by $K \neq 0^+$ terms in eq. (70). Among many such terms, the term most relevant to the ellipsoidal shape deformation is $\hat{v}_{pn}^{(K=2^+)}$ term, a quadrupole term, as we shall discuss later. The multipole interaction is the origin of the shape deformation in general, because the monopole interaction effectively changes single-particle energies without mixing different configurations.

We note that the notation of “rank K ” follows the standard convention, and this article is prepared so that it should not be confused with the quantum number K .

6.3. Central-force contribution

We begin with the contributions of the central force. Figure 10b shows that the central-force multipole(-component) contribution remains negative (more binding). Its monopole contribution is weakly negative for $\gamma < 10^\circ$, but becomes strongly repulsive for $\gamma > 10^\circ$. These phenomena are explained as follows. As the triaxiality increases, the wave function becomes more complex in general. With higher complexity, wider types of correlations seem to be involved or developed in wave functions, which may increase energy gain by the central-force multipole interaction. Namely, as a general feature, larger multipole contributions to the binding energy are expected for larger γ , as it is the case in Fig. 10b. Such correlations induce, in general, more occupations of some orbitals disfavored by the monopole interaction. This is considered to be the main reason why the rapid rise (less binding)

of the central monopole contribution occurs. Up to $\gamma=10^\circ$, however, this rising trend is suppressed, because the nuclear system finds appropriate configurations so that the monopole contributions can keep gaining binding energy against growing γ . This effect is one example of the self-organization by the monopole interaction in nuclei, which implies the optimization of configurations for a given triaxiality [33].

Figure 10b displays, by dotted line labeled “rank-2”, the difference of the contribution of $\hat{v}_{pn}^{(K=2^+)}$ of the central force from its value for $\gamma=0^\circ$. This contribution stays nearly constant from $\gamma=0^\circ$ to 10° , meaning vanished difference. We now discuss how this vanishing occurs, as it looks peculiar at the first glance. The deformation parameter β_2 is kept constant for the plots, and the relation, $\beta_2^2 \propto Q_0^2 + 2Q_2^2$ holds in the lowest-order, where Q_0 and Q_2 are the quadrupole moments (i.e., quantum versions of eqs. (1) and (2)). This β_2^2 can be compared to the expectation value of $\hat{v}_{pn}^{(K=2^+)}$: this value is considered to be approximately proportional to a scalar product of the expectation value of $(\hat{Q} \hat{Q})$ where Q is total quadrupole (moment) operator, assuming also that proton quadrupole moments are approximately proportional to the neutron ones, because of strong pn attraction. The expectation value of $(\hat{Q} \hat{Q})$ with respect to the unprojected state is $Q_0^2 + 2Q_2^2$, in the approximation that only diagonal matrix elements of \hat{Q} contribute. Thus, within these approximations, for the states with a fixed value of β_2 , the expectation value of $\hat{v}_{pn}^{(K=2^+)}$ ($\propto \beta_2^2$) stays constant as a function of γ . It is thus inferred that the pn $K=2^+$ interaction may not notably contribute to a triaxial minimum at the stage of the unprojected state. Figure 10b confirms this feature in the actual case, and more importantly suggests that the lowering of the energy of triaxial states occurs partly due to the pn multipole central interaction excluding its $K=2^+$ component. A detailed inspection shows that this interaction is dominated by $K=4^+$ component or the hexadecupole component. This new finding can have crucial implications.

We stress that the actual expectation values of the quadrupole ($K=2^+$) component of the pn central interaction is an order of magnitude larger than those of the hexadecupole ($K=4^+$) component with respect to low-lying states being discussed, because of stronger coherence effects. Note that the quadrupole and hexadecupole components do not show such a large difference at the level of matrix elements of the states with one proton and one neutron. It is of interest and importance that the hexadecupole interaction nevertheless produces substantial effects on the triaxiality.

6.4. Tensor-force contribution

We now move on to the tensor-force contributions and mention some background. After the prediction of meson-mediated nuclear forces by Yukawa [69], Bethe formulated the tensor force [70] in the form we use now. If one π meson is emitted from a nucleon and is absorbed by another nucleon, a tensor force arises between these two nucleons. In fact, the one- π -exchange process is the major origin of the tensor force working between nucleons, with the cancellation

by a factor of about a quarter due to ρ meson exchange, a resonance of two π mesons. The pn interaction is presently given by the V_{MU} interaction as mentioned earlier, and the V_{MU} interaction includes this tensor force (see [40]). The NN interaction between nucleons in nuclei undergoes substantial renormalizations in general and is changed. Although this is the case for the central forces, the tensor force, particularly its monopole interaction, remains rather unchanged by such in-medium renormalizations. This unique property is referred to as the renormalization persistency [71]. Thus, the π meson exchange remains the major origin of the tensor force in nuclei. It is amazing if such tensor force is directly connected to the triaxial nuclear shape.

Figure 10b includes the monopole and multipole contributions of the pn tensor forces. The multipole contribution of the tensor force appears to be very minor. Although individual terms in the multipole interaction of tensor force are not negligible in general, this has been expected from the viewpoint of the high complexity of the tensor force resulting in cancellations among various contributions. The present study provides definite cases of minor contributions of tensor multipole interaction.

On the contrary, the monopole tensor contribution yields a steady substantial gain of the binding energy. This novel feature is one of the crucial factors for the triaxial minimum, as clarified below.

6.5. High- j orbitals, triaxiality and tensor force

Figure 11b shows a major shell comprising $1h_{11/2}$, $1g_{7/2}$, $2d_{5/2,3/2}$ and $3s_{1/2}$ orbitals. The energies of single-particle orbitals in this figure are schematic. The magnetic substates belonging to the same orbital j are degenerate because the mean potential is isotropic, as shown in Fig. 11b.

In the intrinsic state in the body-fixed frame, a deformed shape can emerge, and it produces energy shifts of those magnetic substates, lifting the degeneracies, as well as other possible changes. This energy shift arises, because different magnetic substates depict different angular distributions, even if they belong to the same j . In order to grasp, somewhat intuitively, resultant changes in single-particle properties, we here introduce a schematic model. If the shape deformation is quadratic, the changes can be assumed to be generated by an additional term to the mean single-particle potential [4, 5],

$$U_q \propto -\beta_2 \left\{ \hat{Q}_0 \cos \gamma + \frac{1}{\sqrt{2}} (\hat{Q}_2 + \hat{Q}_{-2}) \sin \gamma \right\}, \quad (72)$$

where β_2 and γ are deformation parameters introduced already, and $\hat{Q}_{0,2,-2}$ stand for one-body quadrupole operators.

We diagonalize U_q with one or two orbitals and obtain eigenstates denoted by μ , assuming that the other orbitals are not mixed in the present schematic explanation. The parameter values are chosen so that the result facilitates intuitive understanding. The energies of these eigenstates are shown by horizontal bars in Fig. 11. We then investigate how non-vanishing expectation values of the \hat{Q}_2 and \hat{Q}_{-2} operators emerge. Such expectation values are hereafter referred to as

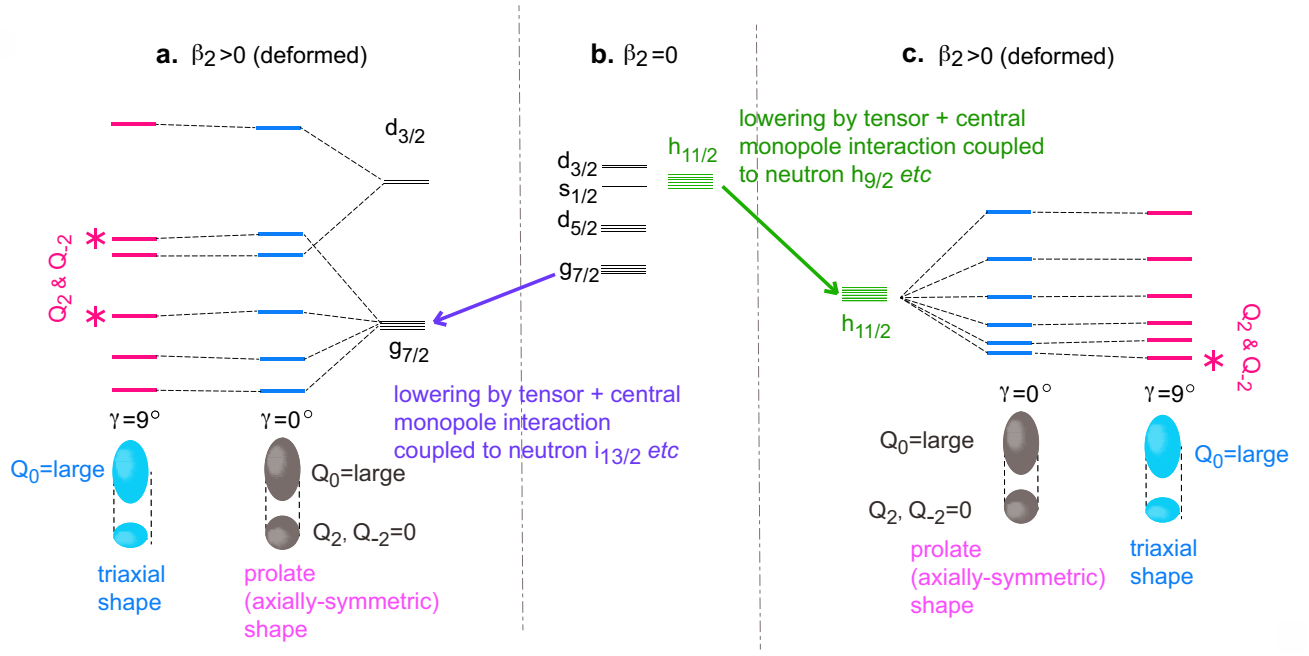


FIG. 11. Triaxiality development with proton single-particle orbitals $g_{7/2}$ and $h_{11/2}$. The major shell comprising $1g_{7/2}$, $2d_{5/2,3/2}$, $3s_{1/2}$ and $1h_{11/2}$ orbitals is displayed in **b**, where $\beta_2 = 0$. **a** Deformed case ($\beta_2 > 0$) ($\gamma = 0$ and 9°) for the orbitals $g_{7/2}$ and $d_{3/2}$. **c** Deformed case ($\beta_2 > 0$) ($\gamma = 0$ and 9°) for the orbital $h_{11/2}$. In **a** and **c**, single-particle states after the splitting and mixing are shown by blue ($\gamma = 0^\circ$) and red ($\gamma = 9^\circ$) horizontal bars. The red asterisks imply that the occupation of these states can enlarge the triaxiality of the nucleus.

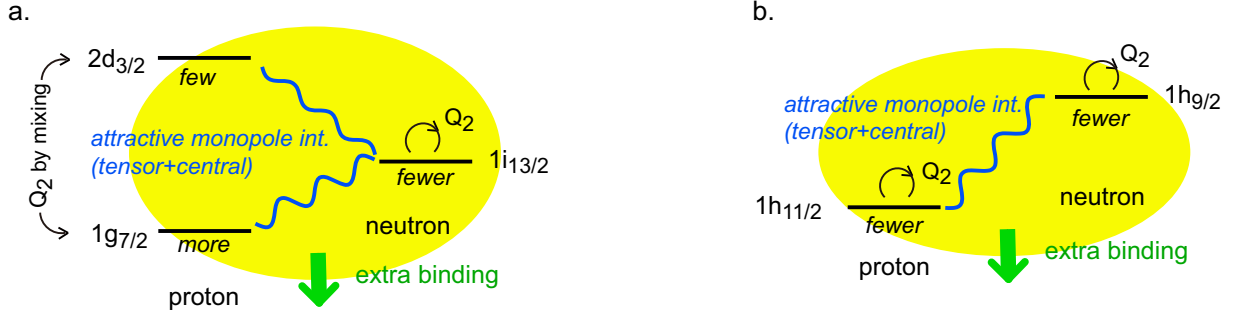


FIG. 12. Two basic modes giving more binding energies to states of triaxial shapes. The blue wavy line indicates proton-neutron monopole interaction (see eq. (69)) which is particularly strongly attractive due to coherent contribution from tensor and central interactions. The enhancement of the Q_2 (implicitly including Q_{-2}) quadrupole moment is indicated by arrows.

Q_2 and Q_{-2} moments of the eigenstates of U_q in eq. (72), and are considered to be parts of the total Q_2 and Q_{-2} moments of the intrinsic state. The energies of such μ states are degenerate for $\beta_2 = 0$, as shown Fig. 11b. Once the deformation sets in with $\beta_2 > 0$, those energies are split. An example is shown in Fig. 11c, where the energies of the μ states of the $1h_{11/2}$ orbital are displayed for $\gamma = 0^\circ$ and 9° .

For $\gamma = 0^\circ$ (shown in gray in Fig. 11c), a prolate (i.e., axially symmetric) ellipsoid arises, and only the Q_0 term in eq. (72) is activated. The degeneracy is lifted, but j_z , the z component of j , is conserved for each μ state. This means that Q_2 and Q_{-2} moments vanish. The energies of these states follow the ascending order: $j_z = \pm 1/2$, $j_z = \pm 3/2$, ..., $j_z = \pm 11/2$. The degeneracy between positive and negative signs is due to the time-reversal symmetry.

There are sizable matrix elements of the \hat{Q}_2 and \hat{Q}_{-2} operators, for instance, between the states of $j_z = 1/2$ and $5/2$, as these operators can change the j_z by two units. With $\gamma \neq 0^\circ$, single-particle states of different j_z 's are mixed in each μ state, with its eigenenergy somewhat shifted from $\gamma = 0^\circ$. Such a case is depicted, for $\gamma = 9^\circ$ in the far right column of Fig. 11c above " $\gamma = 9^\circ$ ". The lowest state produces Q_2 and Q_{-2} moment so as to increase those of the nucleus. The energy shift by changing γ appears to be minor, for the same reason that the quadrupole interaction does not give notable additional binding energy in the present range of γ , as shown in Fig. 10b with the plot "rank-2" (or almost equivalently due to $\cos \gamma$ and $\sin \gamma$ in eq. (72)). However, some other interactions, e.g. hexadecupole interaction, favor states with larger Q_2 and Q_{-2} moments, and if such interactions are included, the two lowest

states can enlarge the values of Q_2 and Q_{-2} moments of the nucleus. This is a general feature for high- j orbitals like $1h_{11/2}$ due to general properties of Clebsch-Gordan coefficients, giving a substantial contribution toward triaxial shapes.

In order that this mechanism produces substantial effects, the relevant orbital, that is $1h_{11/2}$ in Fig. 11c, must be occupied with appropriate numbers of nucleons. Obviously this is not trivial but in the example of ^{166}Er , it is materialized due to an additional binding given by a strongly attractive monopole interaction between a proton in the $1h_{11/2}$ orbital and a neutron in the $1h_{9/2}$ orbital. This situation is illustrated in Fig. 12b. Such a strong monopole interaction is partly due to the tensor force, as explained now.

The monopole interaction of the tensor force generates an attraction between a proton in the $j_> = l + 1/2$ orbital and a neutron in the $j'_< = l' - 1/2$ orbital, where j and j' (l and l') denote the total (orbital) angular momenta, and $1/2$ implies the intrinsic spin of a nucleon [63]. Here, the symbols $j_>$ and $j'_<$ are general notations to specify the particular couplings between orbital and spin angular momenta, as described just above. The attraction is quite strong if angular momenta j and j' are large [61–63]. This feature holds in opposite combinations (proton $j_>$, neutron $j'_<$), too. The tensor monopole interaction is, however, repulsive for $(j_>, j'_>)$ or $(j_<, j'_<)$ combination [63].

The central monopole interaction is strongly attractive for combinations between high- j orbitals in general, owing to large radial overlaps of single-particle wave functions (see examples in [39]). Consequently, the total pn monopole interaction is strongly attractive for $(j_>, j'_<)$ or $(j_<, j'_>)$ combination, if both j and j' are high- j orbitals. Strong coupling between proton $j_>$ and neutron $j_<$ orbitals was pointed out by Federman and Pittel [64], on the basis of the $^3\text{S}_1$ channel of the central interaction. A related feature was discussed in [65], too. The present tensor force effect was not mentioned in either of them, however.

For ^{166}Er , the strong coupling mentioned above is materialized in the combination of (proton $1h_{11/2}$, neutron $1h_{9/2}$). The monopole matrix element of the tensor force is strongly attractive as $v_{1h_{11/2}, 1h_{9/2}}^{\text{mono}} = -0.08$ MeV. Combined with the contribution from the central force [39], the total monopole interaction becomes strongly attractive with $v_{1h_{11/2}, 1h_{9/2}}^{\text{mono}} = -0.39$ MeV, well beyond the overall average value of $v_{j,j'}^{\text{mono}}, -0.25$ MeV, in the present model space. The tensor force contribution is more than half the extra monopole effect. Because the monopole effect is linearly dependent on both $n_j^{(p)}$ and $n_{j'}^{(n)}$ (see eq. (68)), its magnitude can be magnified by large factors. For instance, in the above case, if four protons are in $h_{11/2}$ and four neutrons are in $h_{9/2}$, the extra monopole effect over the average effect amounts to $-0.14 \times 16 = -2.2$ MeV, which is quite substantial, for instance, being more than the usual pairing gap. This linear scaling is a unique property absent in any component of the interaction but the monopole interaction. If such occupancies occur, they can yield certain Q_2 and Q_{-2} moments by the mechanism discussed above, and the shape is driven towards triaxiality. On the other side, if this monopole mechanism is absent, proton $1h_{11/2}$ orbital and/or neutron $1h_{9/2}$ orbital are

lying too high in energy, and their occupancies are not high enough, resulting in smaller values of Q_2 and Q_{-2} moments. This is a basic scenario of triaxiality of low-lying states driven by the tensor+central monopole force, and is one of the self-organization processes as touched upon in the next section. We mention that this process is general and is applicable to other cases with j large, e.g., $h_{11/2,9/2}$ or $i_{13/2,11/2}$, and that high- j orbitals are crucial for larger contributions of higher multipole central interactions, such as hexadecupole one.

There is another type of such a connection, as exemplified in Fig. 11a. The combination (proton $1g_{7/2}$, neutron $1i_{13/2}$) fulfills the afore-mentioned rule of the attractive tensor monopole interaction, with $v_{1g_{7/2}, 1i_{13/2}}^{\text{mono}} = -0.32$ MeV including the central-force contribution. Figure 12a exhibits how this $1g_{7/2}$ orbital comes down in energy. The proton $1g_{7/2}$ orbital then contributes to Q_2 and Q_{-2} moments mainly through the coupling to the $2d_{3/2}$ orbital, when $1g_{7/2}$ is substantially occupied. This is because higher lying magnetic substates with $j_z = \pm 7/2, \pm 5/2$ of the proton $1g_{7/2}$ orbital can be strongly coupled with the states of the proton $2d_{3/2}$ orbital, by the \hat{Q}_2 and \hat{Q}_{-2} terms in eq. (72). This is an actual case of the general trend between an orbital j and another $j - 2$, originating in Clebsch-Gordan coefficient. The orbitals $1g_{7/2}$ and $2d_{3/2}$ can thus be mixed in such a way to yield certain Q_2 and Q_{-2} moments. This is schematically displayed in Fig. 11a, and those magnetic substates are marked asterisks.

The two patterns shown in Fig. 12 may present the typical building blocks for a number of actual couplings for gaining binding energies and promoting triaxiality, although variations can occur. In summary for this topic, the triaxiality can be enlarged in a self-consistent interplay among (i) energy-lowering of high- j orbitals to be involved, due to tensor and central monopole interactions, (ii) nucleon occupancies in states yielding substantial Q_2 and Q_{-2} , (iii) energy-lowering of states with higher triaxiality due to high multipole, particularly hexadecupole, central interaction. In ^{166}Er , these three are present, as an ideal example, while certain variations of the interplay are explored in the next subsection. It is worth mentioning that the involvement of high- j orbitals is essential for this interplay, but low- j orbitals also produce Q_2 and Q_{-2} once the triaxiality is present.

The significance of the (proton $1h_{11/2}$, neutron $1h_{9/2}$) coupling and the (proton $1g_{7/2}$, neutron $1i_{13/2}$) coupling for the case of ^{166}Er is assessed by reducing the monopole interactions for the combinations (proton $1h_{11/2}$, neutron $1h_{9/2}$) and (proton $1g_{7/2}$, neutron $1i_{13/2}$) in Appendix D, or by removing the monopole interaction at all in Appendix E.

It is commented that the tensor force is known to be one of the major driving forces for various shape coexistence phenomena by lowering deformed intruder states, for instance, in $^{64,66,68}\text{Ni}$ ($Z=28, N=36,38,40$) [28, 34, 44, 66] or in $^{181-185}\text{Hg}$ ($Z=80, N=101-105$) [30, 67], where the triaxiality is not necessarily a key aspect.

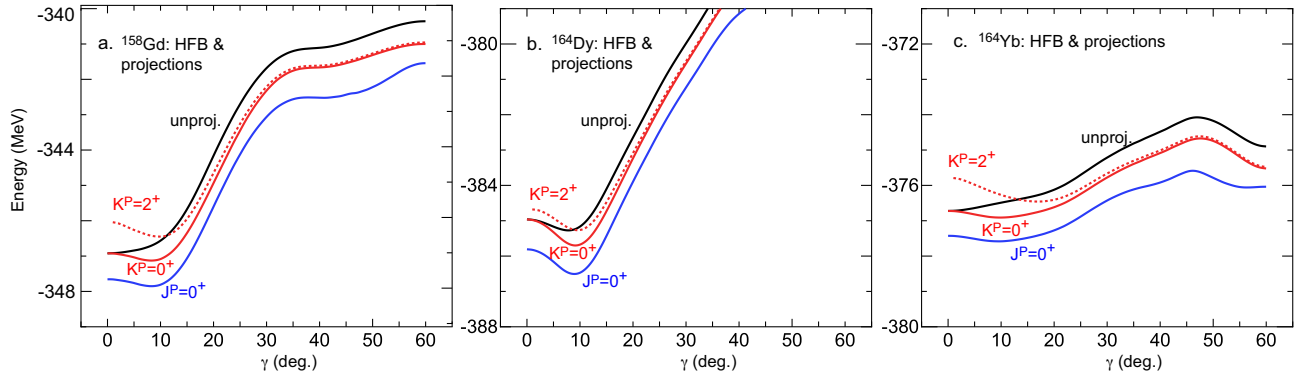


FIG. 13. PES of a. ^{158}Gd ($Z=64$, $N=94$), b. ^{164}Dy ($Z=66$, $N=98$) and c. ^{164}Yb ($Z=70$, $N=94$) obtained by constrained HFB calculation. See the caption of Fig. 7.

6.6. Explorations of triaxiality in other nuclei

It is now of interest to explore other nuclei from the perspectives gained so far. We consider three samples, ^{158}Gd ($Z=64$, $N=94$), ^{164}Dy ($Z=66$, $N=98$) and ^{164}Yb ($Z=70$, $N=94$), located near ^{166}Er ($Z=68$, $N=98$) in the Segrè chart. The triaxiality of these nuclei is confirmed in the CI results (by the QVSM calculation) for the ground and low-lying states. Details of such CI results are presented in Sec. 9. Figure 13 shows the PES obtained by the constrained HFB calculation in the same manner as in Fig. 7.

In Fig. 13, the unprojected PES (black solid line) shows no triaxial minimum for ^{158}Gd or ^{164}Yb , but the slope is slow enough so that a triaxial minimum appears in the $K^P=0^+$ PES (red solid line). The unprojected PES of ^{164}Dy exhibits a minimum, and it becomes quite profound after $K^P=0^+$ projection. This minimum is deeper than the one for ^{166}Er . The unprojected PES of ^{164}Yb is not far from being flat for $\gamma < 20^\circ$, which suggests that the structure of this nucleus may be somewhat closer to that of so-called “gamma-soft nuclei”. For ^{164}Yb , the minimum arises after $K^P=0^+$ projection, although it is shallower than the other two or ^{166}Er . In all the cases, the minimum in the $J^P=0^+$ projected PES is obvious, and will be shown, in Sec. 9, to be consistent with the results of the CI (presently QVSM) calculations.

Figure 14a-c display the same types of plots as the ones in Fig. 10a. The contribution of the pn tensor interaction in ^{158}Gd and ^{164}Dy is as substantial as in ^{166}Er , but it is vanished or repulsive for ^{164}Yb . It is reminded that the tensor monopole interaction can be repulsive depending on the orbital combination. As other terms also produce low PES values for ^{164}Yb up to $\gamma \sim 10^\circ$, the characteristics of gamma-soft nuclei are seen. Further inspections of this feature are an interesting future project, including other gamma-soft nuclei with modest deformation.

The pn central force favors a triaxial minimum in ^{164}Dy but does not for ^{158}Gd . The triaxiality of ^{158}Gd is owing largely to the pn tensor force and somewhat to the rest term.

Figure 14d-f display the analysis by decomposing pn-force effects into monopole and multipole contributions, like Fig. 10b. One notices that multipole central interaction is cru-

cial, and that its rank-2 part shows a small variation around zero. This is the same phenomenon as in Fig. 10b. The monopole tensor interaction is also important, but it does not contribute to the triaxiality of ^{164}Yb . Thus, there are several combinations of the origins of the triaxiality, while pn tensor monopole and pn central hexadecupole interactions appear to be more relevant, and at least, one of them must be actively involved for the emergence of substantial triaxiality in low-lying states.

6.7. Contributions to $K=0$ lowering

The K projection is shown to be crucial in facilitating the substantial triaxiality of the ground band of deformed nuclei. We then conceive a question as to what parts of the Hamiltonian are particularly involved. Figure 15 shows major contributions such as (i) pn central(-force) monopole contribution, (ii) pp pairing contribution, (iii) nn pairing contribution, (iv) pn central(-force) multipole contribution as well as the total contribution, for ^{158}Gd , ^{164}Dy , ^{166}Er and ^{164}Yb . The pairing interaction refers to pp and nn interactions coupled to $J^P=0^+$, after the removal of monopole components which is rather small. It is very natural that the pairing contributions increase the binding energy after the K projection, as they can attractively connect wave functions oriented in different angles. We point out that the pairing contributions to the unprojected states become less attractive as γ increases from 0° , because the xy -plane cross section becomes more deformed. This tendency remains in the $K^P=0^+$ projected states as a function of γ , but the repulsive tendency is weakened as γ grows, lowering the energies from the unprojected values. This is an interesting aspect of the pairing interaction because the pairing interaction contributes to the stabilization of the triaxial minimum of $K^P=0^+$ projected states. It can be taken into account when the pair transfer reaction is studied: pair correlations can be somewhat stronger than in unprojected states.

The pn multipole central contribution produces less binding energy for γ larger after the $K^P=0^+$ projection. This is interpreted as a result of the effective smearing of deformed shape in the xy plane by this projection. In contrast to this, the pn

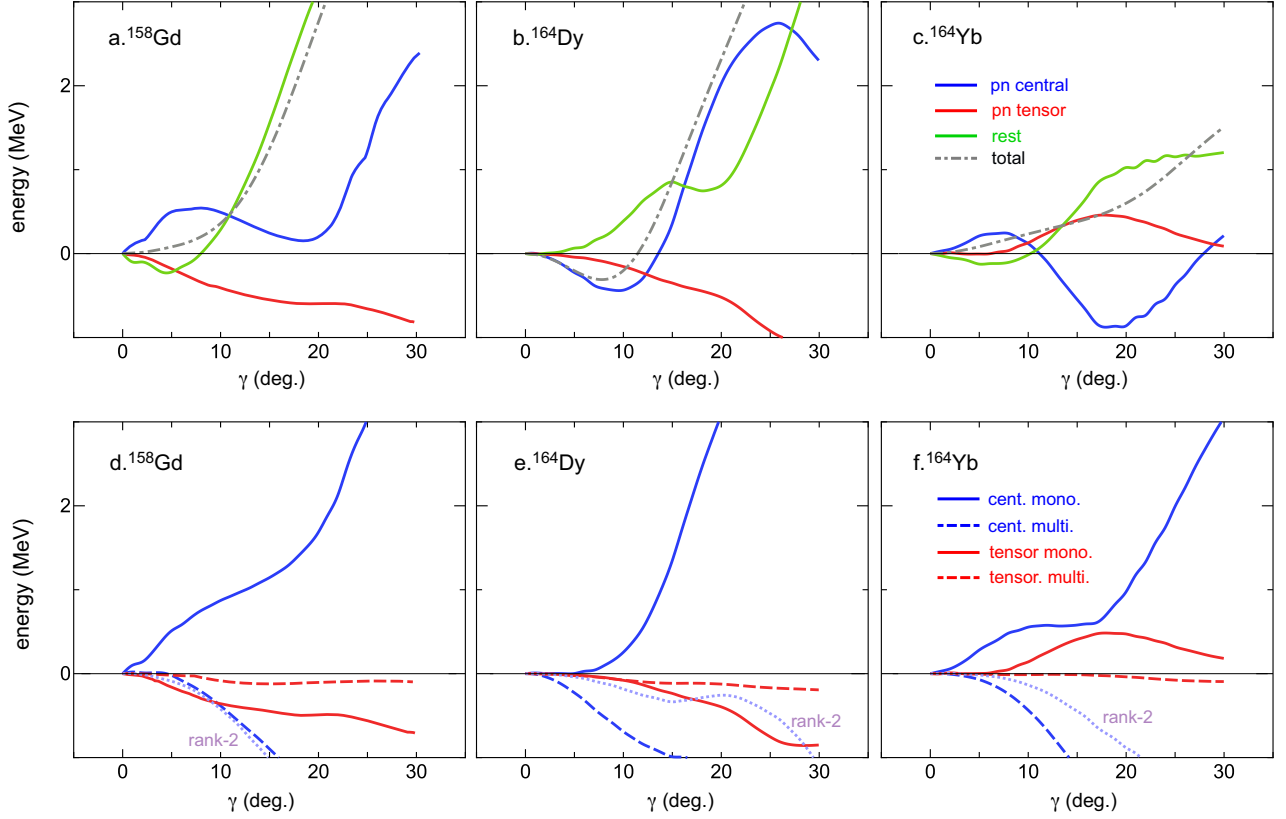


FIG. 14. Properties of the PES of (a.,d.) ^{158}Gd , (b.,e.) ^{164}Dy and (c.,f.) ^{164}Yb as a function of the deformation parameter γ as a constraint. (Upper panel) Decomposition into contributions of proton-neutron central (blue) and tensor (red) forces and the rest (green) of the Hamiltonian. (Lower panel) Decomposition of proton-neutron interaction effects into monopole and multipole components. The rank-2 contribution of the multipole interaction is shown by a dashed line.

monopole central contribution becomes more attractive, because the occupation of more favored orbitals can increase. Although the $K^P=0^+$ projected state may give an impression of slightly weaker deformation (or correlation) energy, the basic building block remains to be the same unprojected state.

We point out that the pairing effect is considerably constant among ^{158}Gd , ^{164}Dy , ^{166}Er and ^{164}Yb .

The same quantities for ^{154}Sm are also shown, and will be discussed in Sec. 10.

7. INTERIM SUMMARY FOR THE TRIAXIALITY AND THE ROTATION

The discussions presented above indicate that there are two major underlying mechanisms for triaxiality. Both originate in the NN interaction, but the effects emerge in different ways. One of them is due to the restoration of broken rotational symmetry caused by $\gamma \neq 0$. The restoration is materialized by the K projection. This is expected to appear virtually in all cases, as the restoration gives additional binding energies to the projected states with $\gamma \neq 0$. For $\gamma=0$, no additional binding energy of this kind arises by definition [55]. If there is this mechanism alone, the resulting triaxiality does not seem

to be so large, as we will see a concrete example in Sec. 10. This triaxiality can then be referred to as “basic modest triaxiality created by symmetry restoration” or simply as “basic triaxiality”. This triaxiality may exist in eigenstates in many CI calculations, but may not show up in unprojected calculations, i.e., what standard DFT approaches normally do. The K projection unveils it. We stress that the present K -projection effect occurs for any isolated deformed composite objects including non-nuclear cases, because the symmetry restoration is universal. It is an intriguing question whether or not this mechanism is related to the bending of triatomic molecules and polymers.

The other origin is specific components of nuclear forces. In the example of ^{166}Er , a pronounced energy minimum arises around $\gamma=9^\circ$ in the PESs (see Fig. 7). This kind of triaxiality will be referred to as “specific-interaction-induced prominent triaxiality”, or simply as “prominent triaxiality”. In a broader scope, such specific interactions include two primary contributors: pn tensor monopole interaction and pn central multipole interaction. Regarding the latter, the rank-2 (i.e., quadrupole) interaction is crucial for the deformation (i.e., large β_2), but is now shown not to generate the triaxiality within the same β_2 value, at least near the actual minimum. Thus, the primary contributor to the latter is ascribed to

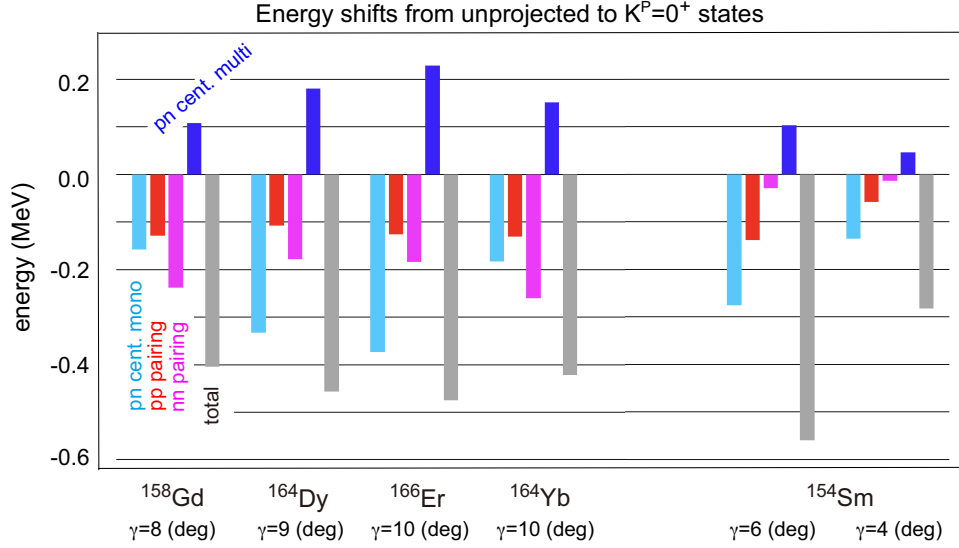


FIG. 15. Contributions of selected components of the interaction for the energy change from the unprojected state to the $K=0$ projected state for ^{158}Er , ^{164}Dy , ^{166}Er and ^{164}Yb , obtained by utilizing the constrained HFB calculation. The selected components comprise the pn central monopole interaction, the pp and the nn pairing interactions, and the pn central multipole interaction, as indicated in the figure. The total change is also displayed. The γ taken for this analysis is shown below each nuclear symbol. A similar analysis is presented for ^{154}Sm with two γ values.

higher rank components, predominantly the rank-4 (i.e., hexadecupole) component of the pn central multipole interaction.

The pn tensor monopole and the pn central multipole (excluding rank 2) interactions can produce substantial effects in many nuclei; in some cases both do, but one of them may do in others. Because of this general relevance, the prominent triaxiality arises in a large number of deformed nuclei (as further presented in Sec. 9), and produces additional binding energy of the order of magnitude of 1 MeV. There are thus a variety of origins of the prominent triaxiality, and they can act coherently. This finding is an intriguing outcome of this study, and may have an impact on future studies on heavier nuclei and fission processes [72–76]. Other components of the interaction may also contribute depending on cases. Note that neither of the two primary contributors was included in the traditional Pairing + QQ model.

We mention that the energy-minimum point of the K projected PES and that of the J projected PES (see, for instance, Fig. 7) depict about the same value of the deformation parameter γ , as an indicator of a stable triaxiality within a given rotational band labeled by K values.

There are also so-called gamma-soft nuclei where the triaxiality is so strong that the γ value can be near 30° and the 2_2^+ level energy is around or below the 4_1^+ level energy. The gamma-soft nuclei are of high interest. However, because they are often characterized by $\beta_2 < 0.25$ and/or $E_x(4_1^+)/E_x(2_1^+) < 3.00$, they are outside the present scope, and will be discussed elsewhere. We anticipate substantial K mixing in many of the gamma-soft nuclei. It is also an intriguing question as to how the concept of the prominent triaxiality will be evolved for gamma-soft nuclei, including its major origin.

We now comment on the monopole interaction. Although it

directly favors no specific shape, the story does not stop there. The monopole interaction effectively changes single-particle energies, and different shapes are associated with different occupation patterns. Monopole interactions can thus produce different binding energies for different shapes. Moreover, the unique linearity of the monopole effect as functions of occupation numbers can make such effects quite substantial (see Subsec. 6.2). In other words, the single-particle environment can be tailored for certain shapes if circumstances allow, and this can yield significant consequences. This mechanism is referred to, in general, as (the quantum mechanical version of) the self-organization [33, 62]. In actual cases, the final shape may emerge from a pool of possible shapes with more or less similar deformation (or correlation) energies. As the binding energy includes both monopole and multipole contributions, the monopole-interaction effect can be crucial for “choosing” the actual shape. It is also noted that monopole and multipole effects can be cooperative with positive feedback between them in the self-organization. In the case of ^{166}Er , certain configurations favoring triaxiality indeed gain more binding energy due to this mechanism.

This emergence of the triaxiality is related to the proper numbers of nucleons in the relevant large- j orbitals. If they are too few or too many, the Q_2 moment cannot become large enough, and the shape remains less triaxial. The near-prolate shapes in Hg isotopes [30] turn out to be an example of too many neutrons in the $1i_{13/2}$ orbit for triaxial shapes.

8. RELATED PROPERTIES AND MODELS

8.1. γ vibration model

The picture described above is confronted with the interpretation in terms of the γ vibration raised [2] and stressed [5, 6] by A. Bohr. The γ vibration is a vibrational distortion of the circular cross section (view B) of Fig. 1f, leading to the intuitive image in Fig. 4a, where the 2_2^+ state carries one γ phonon. This interpretation contradicts the present picture, as this cross section is not a circle but an ellipse displayed in Fig. 1f. The excitation from the ground state to the 2_2^+ state is considered, presently, to be a rotation of the same entity in the quantum mechanical sense (see Fig. 4b), with the change of K quantum number from 0 to 2.

It is reminded that the terminology, γ band, is used in the present work also, just for referring to the rotational band built on the lowest 2^+ state with $K=2$, which naturally excludes the 2_1^+ state. The γ band in the present study has nothing to do with the γ vibration. The band head of the γ band is sometimes called the 2_γ^+ state in literature and also in the present work. We just report that the present MCSM calculation shows no evidence or hint of a γ vibration thus far.

Microscopic investigation on the presence of the γ vibration, without explicitly assuming an axially-symmetric ground state, has been very difficult. As a related work, in [77], this question was indirectly argued, among other issues, from a broader microscopic manner with the Gogny interaction, a well-accepted mean-field model. In this approach [77], the Bohr Hamiltonian was derived microscopically and was diagonalized. It successfully described the excitation energies of the first 2^+ states of many nuclei. The vast majority of second 2^+ states were considered as γ vibrations, but their excitation energies are systematically overestimated [77], casting a mystery to date.

A Relativistic Hartree-Bogoliubov (RHB) calculation by Li *et al.* [78] shows the PES for ^{166}Er with the energy minimum at $\gamma = 6^\circ$. This deviation from the prolate minimum is assessed as “the calculated PES is soft in the γ direction but, as shown below, not soft enough ...” (excerpt from [78]), and a softer PES works against the γ -phonon picture. The calculated value of $B(E2; 2_2^+ \rightarrow 0_1^+)$ is smaller by about a factor of 1/2 than the experimental one, as another indication of the necessity of a softer PES. The triaxial deformation seems to be suggested also from the description of the so-called double γ -phonon state (to be discussed in the next subsection), with a statement “the potential surface might have a minimum for $\gamma \neq 0^\circ$ ” (excerpt from [78]). Although the RHB calculation does not include the tensor force because of the missing Fock term, the scheme may produce reasonable results because the adopted interaction was fitted to a large number of deformed nuclei. If the tensor force could have been included somehow, the energy minimum would have moved to a point with stronger triaxiality. The properties described in [78] and related works, e.g. [79], thus appear to be in a basically consistent passage towards the present study, despite some apparent differences.

From the experimental side, low-energy vibrational modes

from the deformed ellipsoid were extensively reviewed with existing data by Sharpey-Schafer *et al.* [80], casting a doubt over the γ vibration picture for the second 2^+ states, as described in the next subsection.

It is noted that the so-called β vibration was proposed by Aage Bohr together with the γ vibration [2, 5]. Although it is one of the traditional pictures, the existence of the β -vibrational mode has been widely investigated as reviewed, for instance, by Garrett *et al.* [83] and by Sharpey-Schafer *et al.* [80], indicating the negative likelihood of this mode. Although this is an important and somewhat related subject, it lies outside the scope of this study, and will not be discussed in this article.

8.2. Double γ phonon state

With the γ phonon, the double γ -phonon (i.e., $\gamma\gamma$) state can be considered, and we now discuss such $\gamma\gamma$ $J^\pi=4^+$ state. A simple estimation of its level energy is twice that of the γ -phonon $J^\pi=2^+$ state, resulting in $2 \times 0.79 \text{ MeV} = 1.58 \text{ MeV}$ for ^{166}Er . Its experimental candidate state has been identified based on $E2$ decay to the 2_2^+ state, which should be relatively strong due to one-phonon annihilation. The observed excitation energy, 2.03 MeV (see [22, 46, 81, 82]), however, appears to be substantially higher than the value estimated above. This discrepancy has attracted attention over decades.

The $\gamma\gamma$ -phonon state was a focus of the review paper by Sharpey-Schafer *et al.* [80], pointing out that there are candidates for this state among experimentally observed states, but that certain measured properties do not match characteristics of $\gamma\gamma$ -phonon states, such as excitation energies and transfer reaction cross sections. This argument was first made for the nucleus ^{190}Os , which was once believed to be the best candidate for the γ -phonon picture. A similar argument was presented in the case of ^{166}Er [80]. We can quote “There is now doubt about the identification of the first excited $K^\pi = 2_\gamma^+$ bands in all deformed nuclei as arising from γ shape vibrations of the nuclear mean field.” [80], and it is clear that the present study endorses this doubt.

The present theoretical 4_3^+ state is primarily the $K=4$ member of almost the same triaxial shape as that of the ground state. The triaxiality is slightly enlarged for K larger (see Figs. 5c and 9). Its excitation energy is 2.22 MeV by the CI calculation, being closer to the observed value, 2.03 MeV [22, 81, 82]. The calculated value $B(E2; 4^+ \rightarrow 2_2^+) = 10.4 \text{ W.u.}$ is also in agreement with the experimental value $8 \pm 3 \text{ W.u.}$ [22]. Thus, the calculated 4_3^+ state appears to correspond to the 4^+ state assigned traditionally as the $\gamma\gamma$ -phonon state. The difficulty of too high excitation energy then disappears, after the $\gamma\gamma$ -phonon assignment is replaced by the $K=4$ triaxial rotation. Note that in the present MCSM calculation, other 4^+ states may exist below the present 4_3^+ state, with shapes far different, but they are skipped because of limited computational resources.

Figure 9 depicts essential features of $K=4$ states from the viewpoint of the projected energies. The comparison between the left (columns a-c) and right (columns d-f) parts of Fig. 9

suggests that as γ increases from 8.5° to 9.8° , the energy gain by K -projection becomes smaller for $K=0$ and 2, whereas larger for $K=4$. Consequently, the change $\Delta\gamma=1.3^\circ$ reduces excitation energies of $K=4$. These features, visible in Fig. 9, result in a salient agreement between the $J=K=4$ level in column **f** and the experimental $J=4_{\gamma\gamma}^+$ level in column **g**. This trend remains in the MCSM calculation with more basis vectors.

8.3. Davydov model

The triaxial nuclear shape was intensively discussed by Davydov and his collaborators already around 1958 [48, 49]. They proposed a rigid-triaxial-rotor model (Davydov model) that is a special case of the Bohr Hamiltonian [2, 3, 5, 85, 86]. Their systematic studies were an indispensable achievement in the study of nuclear structure. For $\gamma = 9^\circ$, the ratio $B(E2; 2_2^+ \rightarrow 0_1^+)/B(E2; 2_1^+ \rightarrow 0_1^+)$ is calculated to be 0.0233 in the Davydov model [46], reproducing the experimental value (0.0238). As electromagnetic properties directly scan the shapes, the degree of the triaxiality shown by the Davydov model appears to be consistent with the present scheme.

Excitation energies are another story, however. Experimentally $E_x(2_2^+)/E_x(2_1^+) = 9.8$ has been measured. The Davydov model yields this ratio ~ 20 for $\gamma = 9^\circ$, and requires $\gamma \sim 13^\circ$ to reproduce this experimental value. Thus, the Davydov model depicts an internal inconsistency within the model. This is probably because the Davydov model describes the structure of the nucleus in terms of the free rotation of a rigid body with a fixed triaxial shape, and because the excitation energies are due to increased kinetic rotational energies. This view clearly differs from the present picture of deformed nuclei and their energies, where the excitation energies are due to the total Hamiltonian including NN interactions, and a small change of the triaxiality is a natural consequence. The present CI calculation, which incorporates such features, reproduces the observed γ -band excitation energy, as presented in Figs. 4 and 9. The Davydov model is, on the other hand, too rigid and simple to handle such effects, and fails in predicting excitation energies. We emphasize, on the other hand, that the concept of triaxial shapes, one of the two main messages by Davydov and his collaborators [48, 49], is definitely appropriate from the present view, and deserves high appreciation.

We here depict a related new feature about the rigid-triaxial-rotor model based on the present work.

Figure 9 shows the excitation energies measured from the $K=0$ state for $\gamma=8.5^\circ$ and 9.8° . They are calculated based on the right-hand side of eq. (13). By utilizing the expansion, $\cos(K\gamma) \sim 1 - (1/2)K^2\gamma^2 + \dots$, the integral can be expanded by a power series, K^0 , K^2 and higher-power terms. By handling the norm in a similar way, and by expanding the normalized matrix elements in terms of the powers of K^2 , the energies are expressed by a polynomial comprising K^0 , K^2 , and higher-power terms. The K^0 term obviously gives the energy of the $K=0$ state. The K^2 and higher-power terms provide the excitation energies. For a certain triaxiality, the energy kernel in eq. (13) damps more quickly as γ increases, and higher-power

terms become negligibly small. We here restrict ourselves to the limit consisting of the K^0 and K^2 terms; the former is nothing but the energy of the $K=0$ state, and the latter gives the excitation energies proportional to K^2 .

This K^2 dependence can be examined by the ratio $\{E(K=4) - E(K=0)\}/\{E(K=2) - E(K=0)\}$, that is four in the limit. Its actual value by the full K projection calculation is 3.69 and 3.93 for left ($\gamma=8.5^\circ$) and right ($\gamma=9.8^\circ$) parts of Fig. 9, respectively. A similar trend is found in the other sequence of $J=K$ being 0-2-4, with slightly smaller values of the ratio. The K^2 dependence of the excitation energy thus holds to a rather good extent. If γ is fixed, the present case somewhat corresponds to the rigid triaxial rotor.

Figure 9 indicates that the K^2 term with a fixed value of γ turns out to produce too high $K=2$ and 4 excitation energies. Figure 9 suggests that the change of $\gamma=8.5^\circ$ for $K=0$ to $\gamma=9.8^\circ$ for $K=2$ and 4 substantially lowers the excitation energies, which become closer to experimental values, as stated in the previous subsection. Thus, even a small variation of γ can be crucial. This variation is not an adjustable parameter, however, and it is a consequence of the quantum many-body calculation with a Hamiltonian. We comment that in the rigid rotor modeling (see for instance [84]), the K^2 term may have been interpreted as rotational kinetic energy in the xy plane, and the $K=4$ state appears at 4 times excitation energy of $K=2$ state [84]. This was argued to be an evidence against the triaxiality, but what to be excluded is the excessively perfect rigidity of the triaxiality.

8.4. Staggering

Triaxial shape deformation has been discussed also from the viewpoint of the staggering of level energies, an effect due to odd or even integer of the angular momentum J . The signature of the staggering is quantified for a given band by [87, 88]

$$S(J, J-1, J-2) = \frac{\{E(J) - E(J-1)\} - \{E(J-1) - E(J-2)\}}{E_x(2_1^+)}, \quad (73)$$

where $E(J)$ denotes the energy of spin- J member of the band, and $E_x(2_1^+)$ is used for the normalization purpose of the energy scale. The actual value of S thus obtained from experimental energies of ^{166}Er turned out to be 0.290 and 0.269 for $J=4$ and 6, respectively [22]. These values seem to be shown also in Fig. 3 of [88]. They turned out to be 0.326 and 0.302, after replacing $E_x(2_1^+)$ with the corresponding quantity obtained from the level-energy difference between the 6^+ and 2^+ members of the γ band. This value is close enough to the ideal value $S=1/3$, suggesting no notable degree of staggering nor K mixing.

8.5. Deformed Shell Model and other approaches

Quite a few calculations were performed by Sun *et al.* with the deformed shell model for the description of the structure of many heavy nuclei, including triaxial shapes [89, 90]. The

value of the deformation parameter γ was assumed somehow *a priori*, and basis vectors are generated for the deformed single-particle field. They were used for the diagonalization of the Hamiltonian. The actual values of γ appear to be larger than the ones obtained in the present work, and the connection between the two approaches is an open question.

Some other approaches to triaxial shapes were reviewed by Frauendorf in [91] including the Tidal Wave approach [92] and Triaxial Projected Shell Model [93]. The latter seems to have the same root as the deformed shell model.

9. NUCLEI AROUND ^{166}Er IN THE SEGRÈ CHART

9.1. Trends

We next apply the present study to some nuclei around ^{166}Er in the Segrè (nuclear) chart.

One of the experimentally measurable signatures for the substantial triaxiality can be the observed 2_2^+ level below the observed 0_2^+ level, and we adopt it. Figure 16 displays a part of the Segrè (nuclear) chart (even-even nuclei with $Z=50-82$ and $N=82-122$), where red star symbols (including those with orange inner part) indicate 18 deformed nuclei ($3.00 \leq E_x(4_1^+)/E_x(2_1^+) \leq 3.33$) with this signature [8, 22]. These 18 nuclei are traditionally supposed to have prolate ground states, as already stated. The purple star symbols form a separate group, some of which may have been considered, in the past, to be triaxial. In fact, one of them, ^{188}Os , was considered, theoretically, to have $\gamma=30^\circ$ [95]. Missing star symbols do not necessarily imply prolate-like shapes but rather mean insufficient experimental data for judgment.

The CI calculations discussed in this article require huge computer resources, and thereby we have performed them for some selected ones. Figure 17 **a-i** show primary results of such calculations in comparison to the corresponding experimental values. These panels show the level energies of low-lying states, the values of $B(E2; 2_1^+ \rightarrow 0_1^+)$, $B(E2; 2_2^+ \rightarrow 0_1^+)$ (in W.u.), and spectroscopic electric quadrupole moments (in e barn). Considering also that the same Hamiltonian is used for these nuclei, the agreement to experiment [22] is rather good. For instance, the 2_2^+ , 3_1^+ and 4_2^+ states of ^{162}Er (panel **d**) are shifted upwards by the almost same amounts between theory and experiment, compared to those of ^{166}Er (panel **e**). A further shift is seen in ^{158}Gd similarly between experiment and theory (panels **h** and **e**). All shown levels remain quite unchanged between ^{164}Dy and ^{166}Er (panels **g** and **e**), but the $B(E2; 2_2^+ \rightarrow 0_1^+)$ value differs between these two nuclei also similarly in both theory and experiment. Thus, a good overall agreement is obtained between theory and experiment, except for the underestimation of $B(E2; 2_2^+ \rightarrow 0_1^+)$ value of ^{168}Yb . As the changes of the $B(E2; 2_2^+ \rightarrow 0_1^+)$ value by up to a factor of two from nucleus to the nucleus is reproduced rather well in the present calculation, the discrepancy for ^{168}Yb needs to be remedied by improving the Hamiltonian in a future project with a wider coverage of nuclei. The $N=96$ isotones, ^{160}Gd , ^{162}Dy , ^{164}Er and ^{166}Yb , are described similarly well but are not included in Fig. 17 for brevity. The nuclei shown in Fig. 17

and these four fulfill the experimental criteria of the substantial triaxiality mentioned above.

The T-plots for the nuclei, $^{158-162}\text{Gd}$, $^{160-164}\text{Dy}$, $^{162-166}\text{Er}$ and $^{164-168}\text{Yb}$, ^{168}Hf , exhibit large values of deformation parameter γ , mostly being above around 6° . The values are close to (though somewhat smaller than) those of the PES minima by the HFB calculation displayed in Figs. 7 and 13. These nuclei thus exhibit prominent triaxiality in the present MCSM (more precisely QVSM) calculation as well as in the present HFB calculation. In other words, the prominent triaxiality emerges in a wider region of the Segrè (nuclear) chart, and shows a large overlap with the region of substantial triaxiality designated by the experimental criterion stated above.

As these nuclei are located in the middle of the deformed rare-earth region in the Segrè chart and are traditionally supposed to have prolate ground states, the present picture gives a strong impact to the overall understanding of nuclear shape, with a suggestion of the prominent triaxiality prevailing in a number of heavy deformed nuclei, combined with their robust mechanisms.

It is of interest how the excitation energies and $B(E2)$ values can be plotted as functions of the γ value of the 0_1^+ state, where the γ value is extracted from MCSM calculations filtered by good agreement to experiment. Figure 18 displays such a plot of 2_2^+ level energies for $^{158,160,162}\text{Gd}$, $^{160,162,164}\text{Dy}$, $^{162,164,166}\text{Er}$, $^{164,166}\text{Yb}$ and ^{168}Hf . Likewise, Fig. 19 displays the $B(E2; 0_1^+ \rightarrow 2_2^+)$ values for the same nuclei. The systematic trends emerge surprisingly well. These two figures show the values for ^{154}Sm , and we will discuss them in Sec. 10.

If one moves away from these nuclei in the Segrè (nuclear) chart, the triaxiality generally changes from the ranges shown in Figs. 18 and 19. This is an interesting project to be pursued in the future, and we will touch upon the structure of ^{154}Sm in Sec. 10, as an entry point to it.

9.2. Re-visit to early experiments

Quite a few experiments were conducted decades ago for some nuclei of current interest, yielding extensive data by various probes. Examples are found in [96] for ^{168}Er , in [97] for ^{166}Er , in [98] for ^{158}Gd and ^{164}Dy , where the value of the deformation parameter γ was deduced from the data of Multiple Coulomb Excitation experiments *à la* Cline [96, 99], with some variations, based on the Kumar invariant approach [47]. The typical indication is represented by excerpts from [96], “The asymmetric rigid rotor using $\gamma=9^\circ$ reproduces the data well ...” and “The individual E2 matrix elements and the rotational invariants for the ground and γ bands in ^{168}Er all are consistent with rotation of a quadrupole deformed rotor with asymmetry centroid of $\gamma \approx 9^\circ$, ...”. Despite such clear experimental message, there was no statement to suggest a triaxial ground state instead of prolate one, which might be due to the paradigm of the “preponderance of axially symmetric shapes” [17]. The observed features of ^{168}Er resemble those of ^{166}Er , where the MCSM calculation points to $\gamma \sim 9^\circ$ as discussed so far. The value of γ is reported as $\gamma \approx 10^\circ$ for ^{166}Er [97], $\gamma=6(2)^\circ$ for ^{158}Gd and $\gamma=7(4)^\circ$ for ^{164}Dy [98]. The present

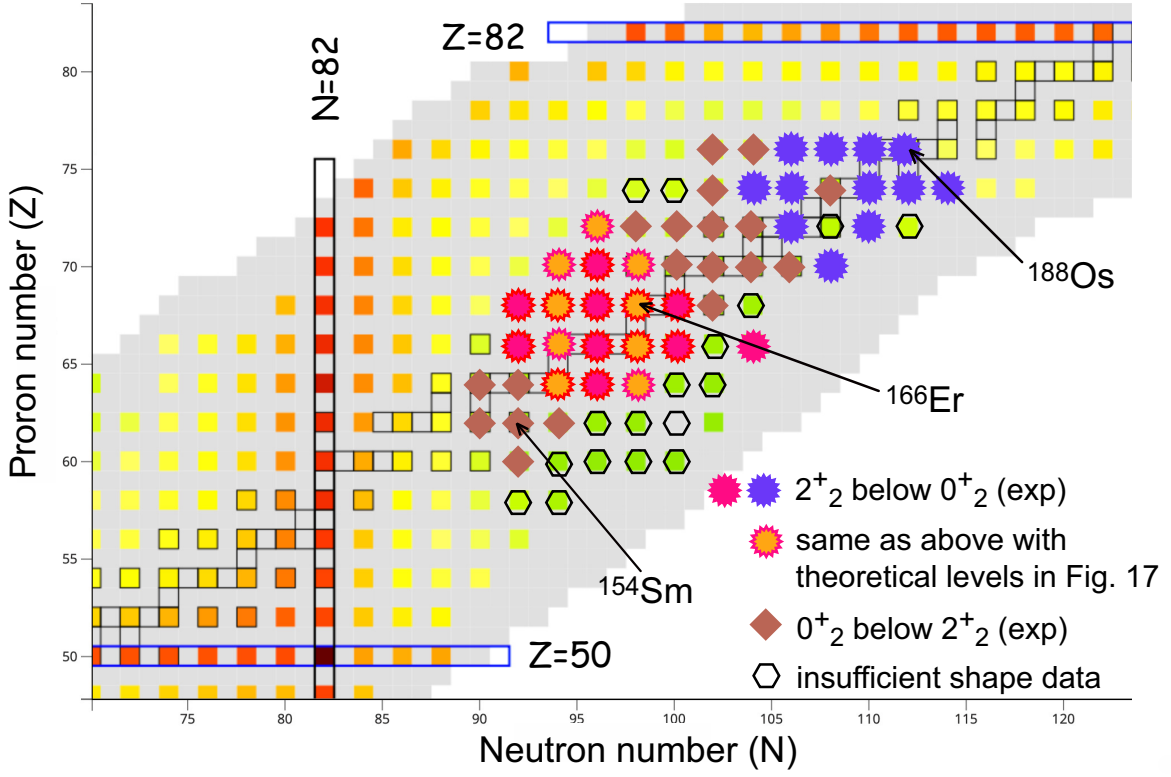


FIG. 16. Nuclear chart (part) and deformed nuclei with substantial triaxialities (red and purple star symbols). Brown diamonds imply the nuclei with the 0_2^+ level below the 2_2^+ level. If not covered by stars or diamonds, red squares indicate the lowest 2^+ states with higher level energies (> 1 MeV), while green squares stand for those with lower 2^+ level energies (< 0.1 MeV). The squares with colors in between indicate intermediate cases. The background is given by NuDat 3.0 [8]. The nuclei with theoretical descriptions shown in Fig. 17 are red stars with orange inside.

MCSM calculation shows $\gamma=5.9^\circ$ for ^{158}Gd and $\gamma=7.3^\circ$ for ^{164}Dy , in a salient agreement with the values deduced from the experiment. Thus, with unbiased eyes, there were experimental evidences supporting the present view that these nuclei depict prominent triaxiality.

As other existing experimental data are also consistent with the present calculation, prominent triaxiality appears to occur in a large number of nuclei in the region of the Segré chart being discussed. Note that this is additional to the basic (modest) triaxiality expected in all deformed nuclei. The idea of “preponderance of axially symmetric shapes” [17] was supported by microscopic calculations in the 1950s [17, 18]. Such calculations did not include either the tensor interaction or the pn central high-multipole interaction, as literally shown by the name of the approach, the Pairing+QQ model [17, 18]. The tensor force effect had been practically overlooked for decades also in the systematic study of the shell structure [61]. A similar history may have been repeated for the shapes, leading to a possible misvaluation of precious experimental data.

10. STRUCTURE OF ^{154}Sm

We now move on to the structure of ^{154}Sm , which has been considered to have the ground state in a (axially-symmetric)

prolate shape and exhibit β and γ vibrational excitations. The structure of this nucleus was discussed by an MCSM approach prior to this work [33], with the statement “the T-plot circles for the ground state are concentrated around $\beta_2=0.28$ and $\gamma=0^\circ$, a prolate shape”. This was our understanding at that time. Note that the picture presented in [33] for side bands was already different from the traditional one. This nucleus has now been studied by an advanced version of the MCSM, i.e., QVSM [38], and the results are presented in [105]. We expand this calculation with some new insights shown below. We focus on the triaxiality of ^{154}Sm in this article, partly because many other important aspects were discussed in [33].

10.1. Energies

Figure 20 shows level energies of low-lying states of ^{154}Sm with some additional states than in [105]. The level energies of the ground band, the so-called β band (on top of the 0_2^+ level) and the γ band (on top of the 2_3^+ level) are well described there.

Such a salient agreement brings us to an analysis using the HFB calculation similar to the one shown in Fig. 7. The outcome is displayed in Fig. 21. The unprojected energy starts to rise at $\gamma=0^\circ$, and keeps rising with a rate, ~ 5 MeV from $\gamma=10^\circ$

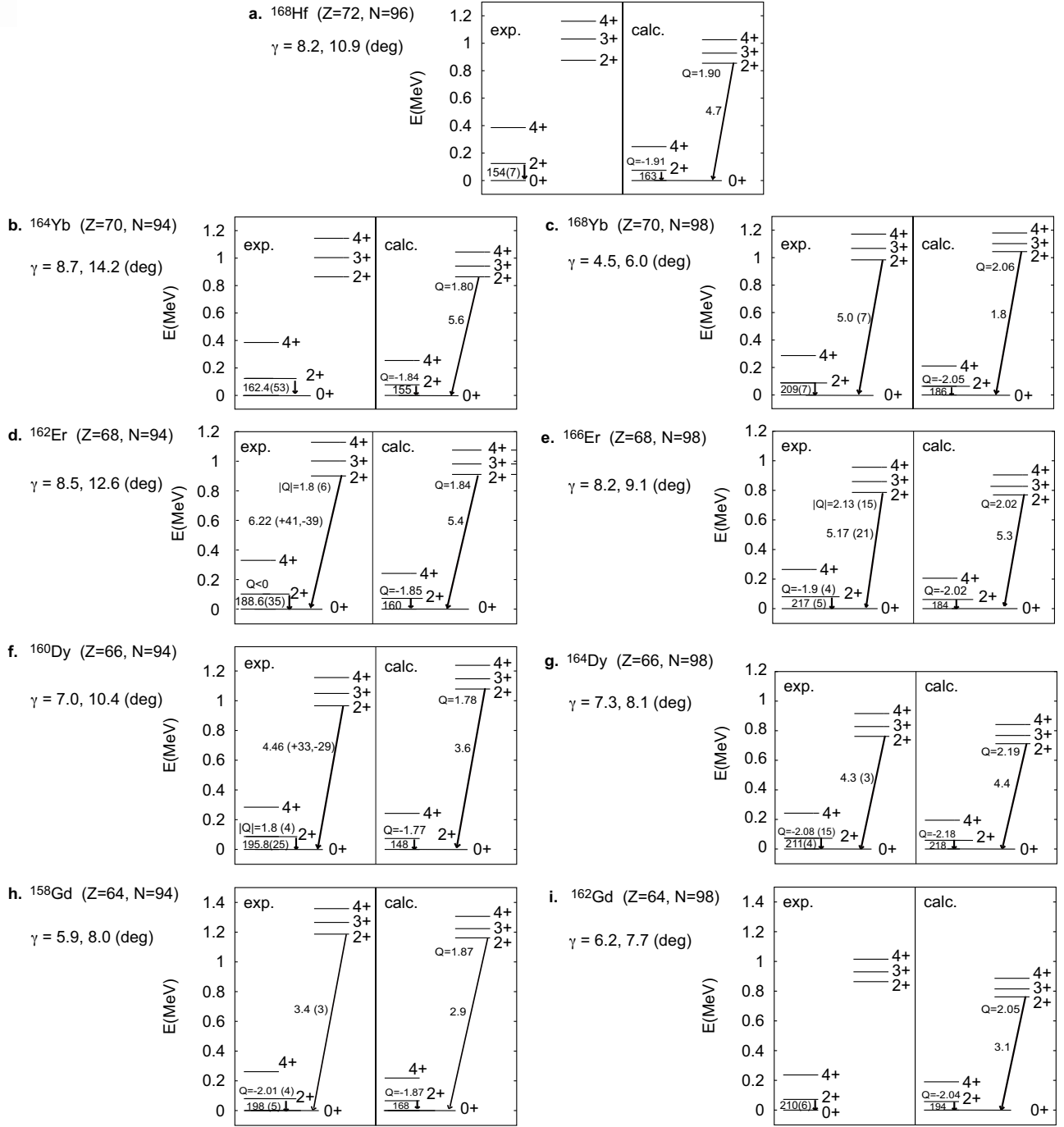


FIG. 17. Lowest level energies of **a** ^{168}Hf , **b** ^{164}Yb , **c** ^{168}Yb , **d** ^{162}Er , **e** ^{166}Er , **f** ^{160}Dy , **g** ^{164}Dy , **h** ^{158}Gd , and **i** ^{162}Gd . Theoretical and experimental [22] values of $B(E2; 2_1^+ \rightarrow 0_1^+)$ and $B(E2; 2_2^+ \rightarrow 0_1^+)$ (see arrows) are shown in W.u., if available. The spectroscopic electric quadrupole moment is shown (see "Q") in the unit of e barn for the 2_1^+ and 2_2^+ states: all theoretical values and available experimental values [22]. The mean values of the deformation parameter γ of the 0_1^+ and 2_2^+ states are shown for each nucleus below the nucleus name.

to 30° , which is about twice faster than the corresponding rate of ^{166}Er in Fig. 7 (~ 3 MeV from $\gamma=10^\circ$ to 30°). Nevertheless, the K projection locates its minimum around $\gamma=6^\circ$, as a consequence of the underlying mechanism described in Sec. 4. The J projection does not cause any major change besides an overall shift of the energy downwards. Note that the correla-

tions incorporated by the QVSM calculation place the T-plot circles with mean value $\gamma \sim 3.7^\circ$. It has been seen for ^{166}Er and other nuclei that additional correlations incorporated by QVSM calculations reduce the HFB γ values by 1-2°, and the same trend appears here.

The unprojected PES in Fig. 21 monotonically increases by

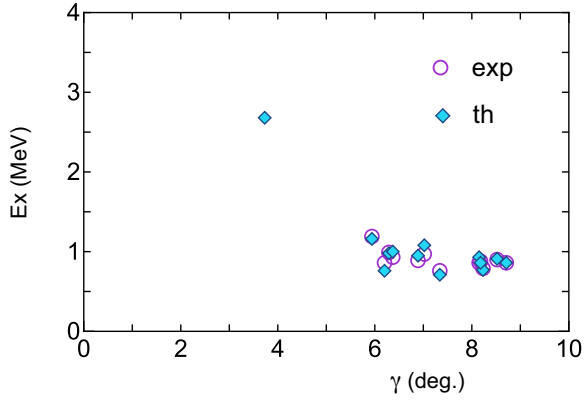


FIG. 18. Systematics of experimental (open circle) and theoretical (blue diamond) 2_2^+ excitation energy as a function of the deformation parameter γ , except for the far left blue diamond, which represents the 2_2^+ state of ^{154}Sm to be discussed in Subsec. 10.2. The symbols represent, from right to left, ^{164}Yb ($\gamma=8.7^\circ$), ^{162}Er (8.5°), ^{166}Er (8.2°), ^{168}Hf (8.2°), ^{164}Er (8.2°), ^{164}Dy (7.3°), ^{160}Dy (7.0°), ^{162}Dy (6.9°), ^{166}Yb (6.4°), ^{160}Gd (6.3°), ^{162}Gd (6.2°), ^{158}Gd (5.9°), ^{154}Sm (3.7°), respectively.

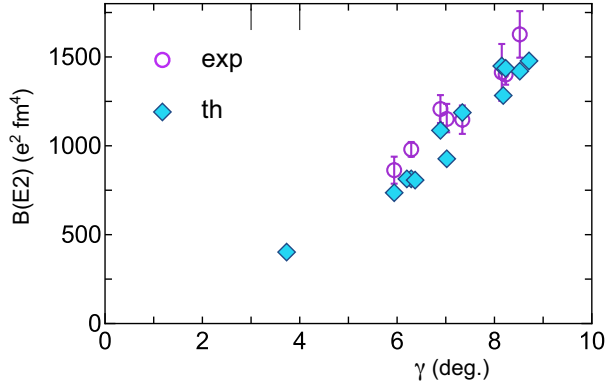


FIG. 19. Systematics of experimental (open circle) and theoretical (blue diamond) $B(E2; 0_1^+ \rightarrow 2_2^+)$ values as a function of the deformation parameter γ . See the caption of Fig. 18. The far left blue diamond represents $B(E2; 0_1^+ \rightarrow 2_2^+)$ value of ^{154}Sm (see Subsec. 10.2).

about 4 MeV as γ changes from 0° to 20° . This is comparable to the corresponding trends of other approaches such as Gogny Hartree-Fock Bogoliubov approximation [106], Relativistic Energy-Density Functional method [107] and relativistic Hartree-Bogoliubov model [108]. In this sense, the present work appears to exhibit rather consistent features up to the unprojected PES. However, the K projection was not activated in those approaches, leading to no triaxial ground states.

The analysis similar to the one for ^{166}Er shown in Fig. 10 is carried out as shown in Fig. 22. Figure 22a indicates that all three components of the interaction work against triaxiality until γ becomes about 20° . This may be a typical phenomenon in nuclei comparatively close to prolate shapes. Figure 22b presents more anatomy: the central-force multipole interaction favors triaxiality, but its effect is canceled out by strong opposition from the central monopole interaction. The tensor

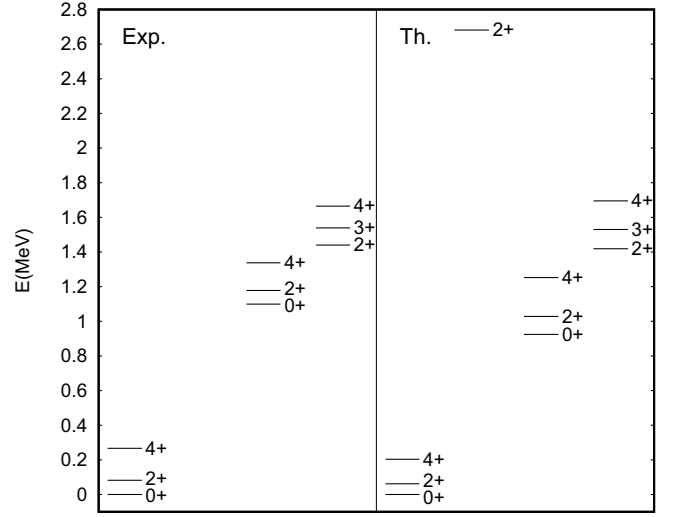


FIG. 20. Lowest level energies of ^{154}Sm compared to experimental ones [22].

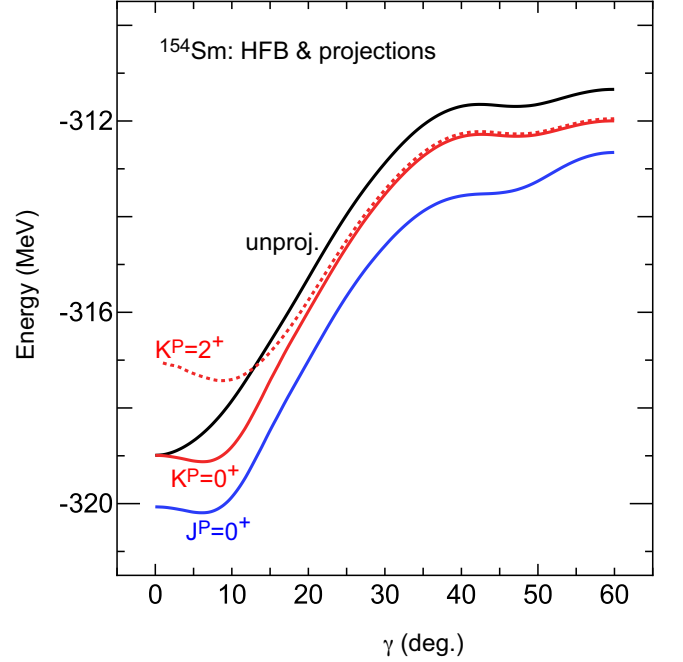


FIG. 21. Energies of the ground state of ^{154}Sm given by HFB calculations. See the caption of Fig. 7.

monopole interaction does not help either. The rank-2 central-multipole contribution does not stay near 0, most likely due to a rapid structure change by imposed γ values, as consistently shown by the fast rise of the unprojected PES.

The unprojected PES thus looks against the emergence of the triaxiality, and the triaxiality seen in Fig. 21 is perfectly due to the projection onto $K=0$, i.e., the symmetry restoration.

Figure 15 includes two cases of ^{154}Sm with $\gamma=6^\circ$ and 4° with binding-energy gain of 0.56 and 0.28 MeV, respectively, supporting the occurrence of the basic triaxiality. The gain is smaller for $\gamma=4^\circ$, as expected, but remains finite. Thus,

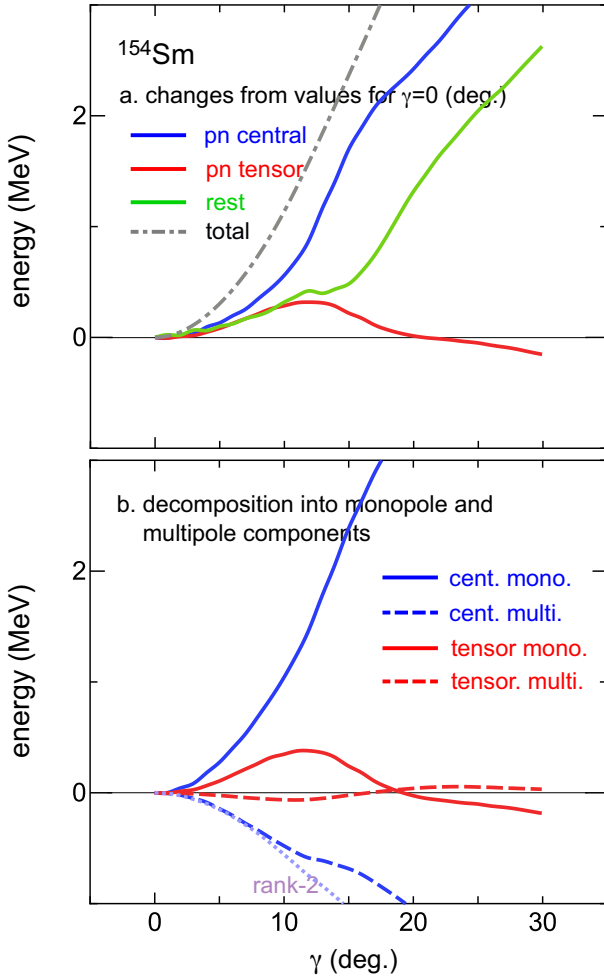


FIG. 22. Properties of the PES of ^{154}Sm as a function of the deformation parameter γ as constraint. **a.** Decomposition into contributions of proton-neutron central (blue) and tensor (red) forces and the rest (green) of the Hamiltonian. **b.** Decomposition of proton-neutron interaction effects into monopole and multipole components.

^{154}Sm exhibits how the basic triaxiality arises, which is different from the prominent triaxiality discussed in previous sections. There must be many nuclei showing the basic triaxiality due to the same underlying mechanism.

10.2. Tplots

Figure 23 shows Tplots for the $0_{1,2}^+$ and $2_{1,2,3,4}^+$ states. One finds two major patterns: one is shared by the 0_1^+ , 2_1^+ and 2_4^+ states, and the other by the 0_2^+ , 2_2^+ and 2_3^+ states. The latter group shows T-plot circles at rather large values of γ , indicating that the states of the latter group are of prominent triaxiality with an average value of $\gamma \sim 13^\circ$. So, there is a shape coexistence for ^{154}Sm with the basic and prominent triaxialities. Although this phenomenon was pointed out in [33], the in-depth explanation was missing.

The ground band built on the 0_1^+ state was considered, based on human sight, to be of $\gamma \sim 0^\circ$ in [33], without high-

resolution inspection. The objective extraction of the mean γ value has been implemented in the present study [43], and the obtained result appears to be $\gamma \sim 3.7^\circ$. Very recently, an experimental value of γ , $5.0 \pm 1.4^\circ$, is obtained for ^{154}Sm by the experiment on its Giant Dipole Resonance [109].

The obtained small but finite γ value is consistent with the HFB analysis above, and produces a $K^P=2^+$ state as well as $K^P=0^+$ state. The $K^P=2^+$ 2^+ level is calculated, in the present QVSM calculation, to be at the excitation energy ~ 2.7 MeV with a similar T-plot pattern to the 0_1^+ and 2_1^+ states. We emphasize that this state emerges because of the triaxiality of the ground state, and denote it by $2_{g\gamma}^+$, meaning the “ 2_γ^+ ” state within the family of the ground state having similar triaxialities. This $2_{g\gamma}^+$ state is predicted to be excited from the 0_1^+ state with $B(E2) \sim 400 e^2\text{fm}^4$.

Figures 18 and 19 include the values for the $2_{g\gamma}^+$ state of ^{154}Sm , which are only predictions. These values appear to be on smooth extrapolations. It is of great interest to see them experimentally in the future.

10.3. Deformation parameter γ

We briefly survey the triaxiality of some nuclei surrounding ^{154}Sm in the Segrè chart. The values of the deformation parameter γ is displayed in Fig. 24 for certain low-lying states of ^{154}Sm , as well as for the 0_1^+ states of $^{152,154}\text{Nd}$ and those of $^{152,154,156}\text{Sm}$. The γ value is almost the same between ^{152}Nd and ^{154}Nd , likely suggesting a stable modest triaxiality of $\gamma \sim 2^\circ$ in this region of the Segrè chart. A consistent tendency is found in the chain of the $^{152,154,156}\text{Sm}$ isotopes: γ is as large as about 8° for comparatively less deformed nucleus ^{152}Sm , and becomes closer to 2° in strongly deformed nucleus ^{156}Sm . Further studies on heavier isotopes are of interest.

The γ value of various states of ^{154}Sm is also shown in Fig. 24. The states are labeled by β for the 0_2^+ band, while the γ band means the lowest band built on a 2^+ state. The γ value is almost constant within each band. The γ value is larger by $\sim 1^\circ$ for the γ band than for the 0_2^+ band, similarly to the γ -value difference between the 0_1^+ and 2_2^+ bands of ^{166}Er . The last column corresponds to the $2_{g\gamma}^+$ state discussed just above (Subsec. 10.2). It belongs to the family of the 0_1^+ state and depicts a similar T-plot to the one for the 0_1^+ state (see Fig. 23). The γ value of the $2_{g\gamma}^+$ state is larger by $\sim 2^\circ$ than that for the 0_1^+ state, again similarly to the cases mentioned above. This shift can be understood in terms of the same kind of the stretching, with slight enhancement, as in Subsec. 5.6. It does not seem to change the basic picture of the $2_{g\gamma}^+$ state as the $K=2$ member of the ground-state structure.

11. SUMMARY AND PROSPECTS

This article primarily shows (i) the unexpected wide appearance of triaxial shapes in heavy deformed nuclei, (ii) the fully quantum many-body derivation of the $J(J+1) - K^2$ rule of the excitation spectrum of rotational bands, with examples by

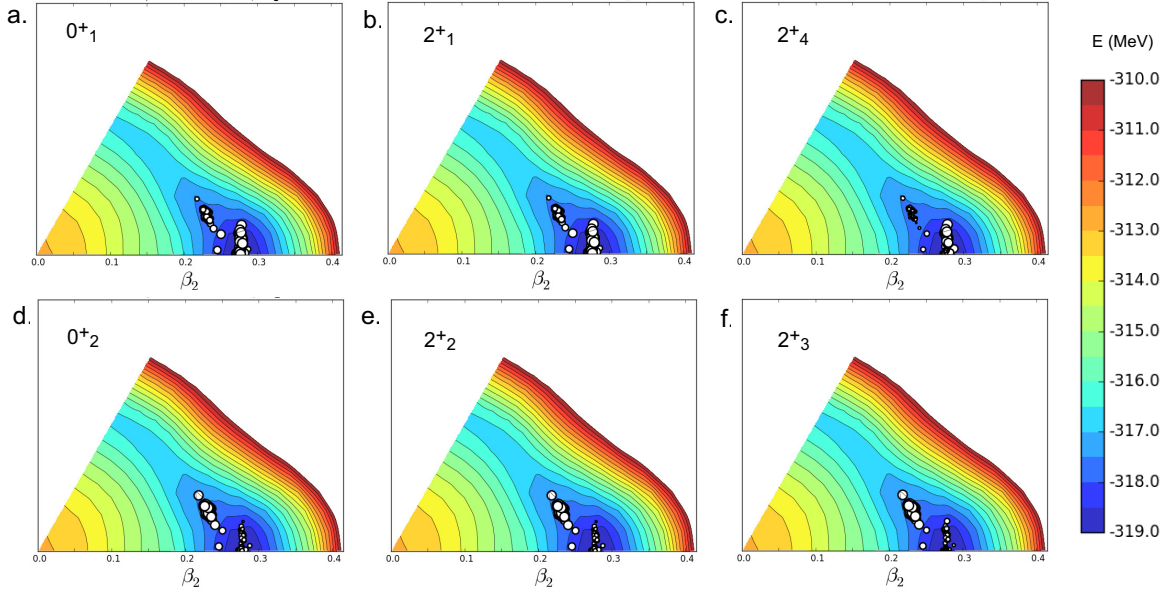


FIG. 23. T-plots for the $0^+_{1,2}$ and $2^+_{1,2,3,4}$ states of ^{154}Sm .

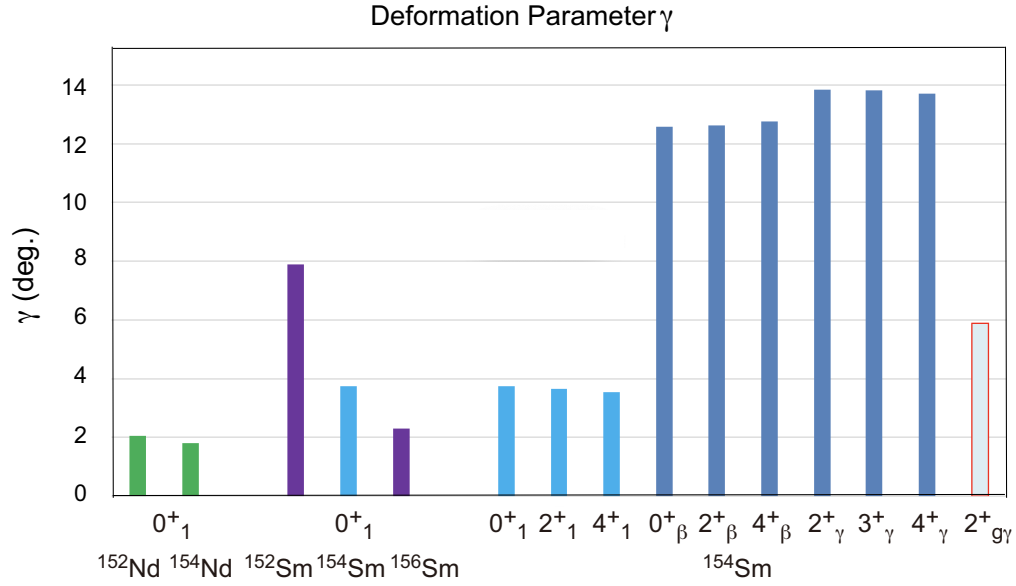


FIG. 24. Deformation parameter γ (degrees) for the 0^+_1 states of $^{152,154}\text{Nd}$ and $^{152,154,156}\text{Sm}$ nuclei. For ^{154}Sm , the value for the members of other bands are shown also. The β and γ bands are triaxial states with large values of the deformation parameter γ . The far right column is for the γ -band head built on the ground state.

^{166}Er , ^{154}Sm and some other heavy nuclei.

Two origins of the triaxiality are indicated. Once a triaxial shape arises in the xy plane (see Fig. 1), it breaks the symmetry of the rotation in this plane. This symmetry is restored by projecting onto a K quantum number as the intermediate step before the projection onto a good J value. The J projection generally causes K mixing, but it is quite weak if the deformation is strong enough, as in heavy deformed nuclei discussed in this paper. Realistic nuclear forces lower the $K=0$ state below $K \neq 0$ states. Because of this binding-energy gain, the

energy minimum is located at a finite γ value. This mechanism due to the symmetry restoration is clearly robust. It occurs in virtually all cases of strong deformation, including ^{166}Er and ^{154}Sm . The triaxiality by this mechanism is called “symmetry-created basic modest triaxiality” or simply “basic triaxiality”.

The triaxiality due to this symmetry restoration not only computationally appears in the result of the mathematical procedure, but also demonstrates how important is the interplay between intrinsic degrees of freedom (shape deformation pa-

rameters) and extrinsic features (e.g. J and K values characterizing bands and levels). For example, by specifying $K^P=0^+$, the form of the energy minimum as a function of γ is changed from the unprojected result, yielding a certain additional binding energy for certain finite γ values. As another example, each K^P band corresponds to different value of γ , and physical quantities given by such γ values exhibit good agreement with experiment. This γ variations are less than 20% of the $K^P=0^+$ γ value as shown concretely by the present CI calculations, but the excitation energies are substantially changed.

Another origin of the triaxiality is the specific components of nuclear forces. The monopole component of tensor force and the high multipole component of central forces are crucially important as well as the involvement of high- j orbitals, such as $h_{11/2,9/2}$ and $i_{13/2,11/2}$. Appropriate occupations to such orbitals are shown to bring about “prominent triaxiality” with $\gamma \sim 9^\circ$ in ^{166}Er , and that with $\gamma \sim 6^\circ$ - 13° in some other nuclei, as far as investigated so far. Due to the renormalization persistency [71], the tensor force in nuclei is closely related to the one- π -meson exchange process, leading to a direct connection between such an “elementary-particle” process and nuclear shapes. The π -meson exchange is treated separately also in the modern theory of nuclear forces [100] as materialized as the chiral Effective Field Theory [101] of the Quantum Chromo Dynamics.

The constrained Hartree-Fock-Bogoliubov (HFB) analysis was conducted to show the contributions of certain components of nuclear forces as functions of γ : tensor monopole and central multipole interactions are quite important for prominent triaxiality. Interestingly, the quadrupole interaction does not produce additional binding energy for triaxial states, as long as β_2 is fixed. The effects of higher rank interactions, particularly hexadecupole interaction, can enlarge triaxiality and those effects can be enhanced by triaxiality, yielding more binding energies for larger triaxiality. This may lead us to a plausible connection between triaxiality and fission, mediated by hexadecupole properties. It is noted that higher rank interactions are naturally included in the present work, as the pn central interaction is given by a Gaussian finite-range interaction (V_{MU}) with the strengths fixed so as to be consistent with microscopic interactions for a number of nuclei, from sd -shell nuclei up to Hg isotopes [30, 39].

If the prominent triaxiality occurs, it is generally seen that the γ value increases from the ground band to the γ band and the $\gamma\gamma$ state, as also mentioned above. This is a kind of stretching effect with K value due to nuclear forces. The difference is as “small” as $\Delta\gamma=1.3^\circ$ (see Fig. 9), but it is related to a significant lowering of energies. We thus need to be careful about the gauge of the deformation parameter γ : $\gamma \sim 9^\circ$ cannot be identified as a small number. As a separate remarkable feature, the γ value extracted from the CI calculation depicts clean trends, for instance, with the $B(E2; 2_\gamma^+ \rightarrow 0_1^+)$ (see Fig. 19). Figure 19 implies that the parameter γ is one of the dominating variables, and endorses the K rotation as the basic mode. The superheavy nuclei are one of major objectives of nuclear physics [73, 75]. The triaxiality is certainly more relevant to superheavy nuclei, as the deformation will be more

significant source of their binding energy. As a separate point, a notable stretching has not been found in the J projection, probably because of a stable equilibrium.

As the second major point of this paper, we looked into the consequences of the restoration of J , total angular momentum. The excitation energies within rotational bands have been empirically known to follow the $J(J+1)$ rule very well. However, its explanation in terms of the quantum many-body theory has been missing. Traditionally, the argument starts from the classical rotation of a rigid-body object, as shown in panel **a** of Fig. 25 (see, for instance, [4, 10, 12]). The quantization of the free rotation of a rigid-body object with the axial symmetry, like a symmetry top, was adopted as the foundation for the $J(J+1)$ rule (see panel **b** of Fig. 25).

We now can prove that the $J(J+1)$ rule is derived through a fully quantum mechanical treatment of many-body systems: panel **c** of Fig. 25 displays that the intrinsic state (represented by ellipsoid) is rotated to various angles shown by radial arrows, and such rotated states are superposed with designated amplitudes so as to be the eigenstate with a given angular momentum J . The excitation spectrum arises as a consequence of the Hamiltonian acting between bra and ket states with different angles (see panel **c** of Fig. 25). The integrated effects follow the hierarchy of the power counting of $(\cos\beta - 1)^k$, where β stands for the usual Euler angle. The $J(J+1)$ rule arises as the exact solution at the NLO (next-to-leading order), i.e., $k=1$, of this power counting, and can be extended to the $J(J+1) - K^2$ rule for bands with $K \neq 0$. The derived formulas enable us to assess the effects of Hamiltonians on the band-head energy and on the “moments of inertia” of rotational bands, in a transparent and precise way. Here, the Hamiltonian comprises single-particle energies, nucleon-nucleon forces, three-nucleon forces, *etc.* The formula is also applicable to various problems of the spin physics of composite systems.

The present study on the K and J projections is closely related to the restoration of broken symmetry. As well known, the Nambu-Goldstone Mode (NGM) has been introduced for the symmetry restoration of internal degrees of freedom [102–104]. However, the extension of the NGM to geometrical symmetries like the rotational one is known to be difficult to date. The present work may contribute to it, for instance, by showing the derivation of the dispersion relation.

The mixing of states of different K values may occur in principle. However, the $J^P = 0^+$ ground state is always $K^P = 0^+$, and it appears that the K quantum number is rather well conserved in strongly deformed nuclei [46]. In addition, the gradual minor enlargement of γ for higher K is expected to generally suppress K mixing. Because of this property, the derivation of the $J(J+1) - K^2$ rule makes sense in general cases including finite triaxiality or more complicated configurations like clusters or molecules. This feature differentiates the present discussion from the conventional quantization argument for rigid-body rotor.

Based on the robustness of the triaxiality, the prevailing triaxiality in heavy deformed nuclei is addressed in the present study. The preponderance of prolate shapes, stressed by Aage Bohr, has been a textbook item (e.g. [4, 5, 10, 12]), but the

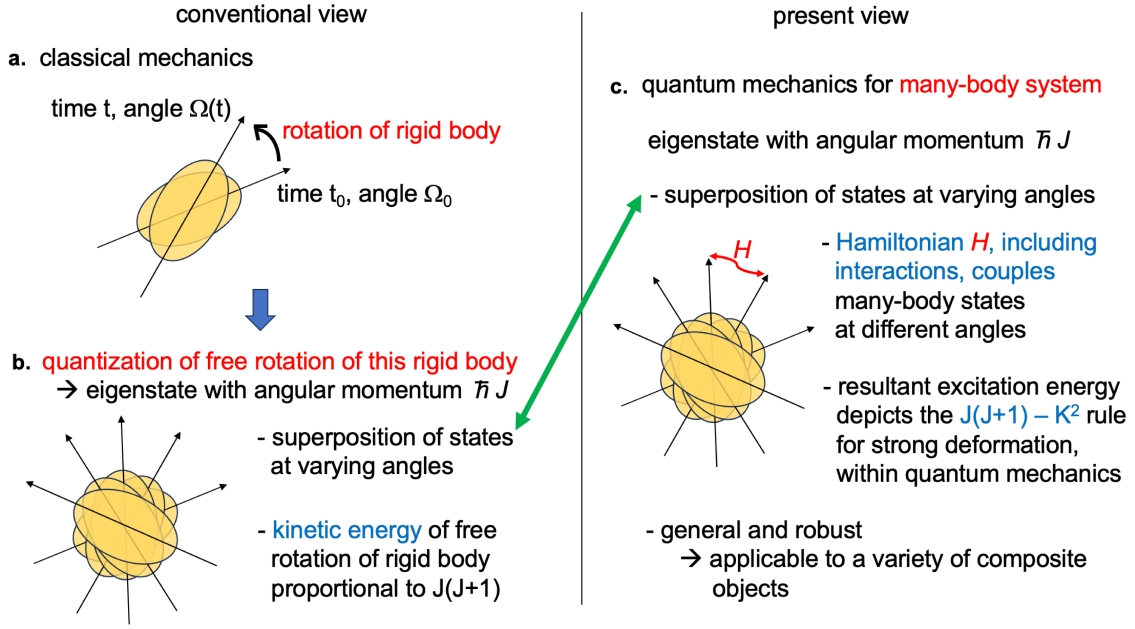


FIG. 25. Pictures of the rotation of objects like atomic nuclei. **a.** Classical mechanical view. **b.** Quantization of freely rotating rigid-body. **c.** View of the quantum mechanical system composed of many ingredients with conserved angular momentum $\hbar J$. The $J(J+1) - K^2$ rule arises. The green arrow indicates similarity in the wave function, but the energy comes from different origins.

situation may change [80]. Consequently, the traditional description by γ vibration will be replaced by the rotation of triaxial ellipsoids that is quantified by the K quantum number practically conserved in strongly deformed nuclei. These new pictures and concepts are supported by state-of-the-art extra-large-scale CI calculations (i.e., Quasiparticle Vacua Shell Model version [38] of the Monte Carlo Shell Model) with realistic effective interaction. The agreement with measured spectroscopic data is quite good. Such salient agreement suggests possible prospects of the present approach applied to other cases, like nuclei with an odd number of nucleons, so-called octupole states, *etc.* In particular, possible relations to the Nilsson model are of great interest [110].

It is still a major experimental challenge to explicitly or critically extract the triaxial shape of the ground state, *albeit with intrinsic difficulty*. Magnetic excitation is a possibility: more excitation modes may appear besides the scissors mode [111]. Such experiments may be done in facilities like HIγS and RCNP, while the outcome may be indirect. Another intriguing possibility lies in relativistic heavy-ion collision as a new tool for scanning the nuclear shape [112–117]. The experiments in this line have been performed in LHC/CERN or RHIC, for instance, [118–124], and more are expected to come. Hyper nuclei containing a Λ particle may provide with another opportunity to see the triaxiality, in the form of splitting of the level energies, which can be seen in J-Lab or J-PARC. Another relevant feature is the chirality. As a result of substantial triaxiality in the strongly deformed region, nuclear chiral doublet bands [125] may appear more widely than expected, providing new experimental opportunities.

Above all these approaches, significant contributions from multiple Coulomb excitations initiated by Cline *et al.* [96]

and extended further by Fahlander *et al.* [97] and Werner *et al.* [98] should not be overlooked. Those experimental data already pointed out, decades ago, the same trend as the present theoretical work, but the meanings may not have been appreciated. More experiments with improved efficiency and precision will be of interest and use. For the basic modest triaxiality, the E2 excitation from the ground state to the 2_{gy}^+ state seems to be of great interest, for instance, in the case of ^{154}Sm .

The binding energy gain by the deformation is likely more crucial in heavy and superheavy nuclei, and the possible appearance of triaxiality was shown even without including the present mechanism, for instance, [73–76]. The triaxiality has also been addressed over decades as it may lower the first fission barrier [72]. As triaxiality is a robust reality, due to the symmetry restoration and certain characteristics of nuclear forces, rather than an accidental incident, it may also produce more visible effects on such heavy nuclei than previously thought.

Regarding nuclei lighter than $A \sim 100$, Fig. 3 displays a few nuclei with the strong shape deformation fulfilling the criterion given there ($E_x(4_1^+)/E_x(2_1^+) \geq 3.00$). This ratio is 2.99 for ^{12}C nucleus. The 0_1^+ and 2_1^+ states of ^{12}C were investigated in the *ab initio* no-core MCSM calculation [37], depicting that the $K=0$ intrinsic state extracted from the 0_1^+ state almost perfectly reproduces, by the J projection of this $K=0$ state, the wave function of the 2_1^+ state obtained by the MCSM calculation, despite substantial triaxiality in both states [37]. This feature seems to suggest the applicability of the present idea in such a first-principles approach. Note that the clustering component is contained in these states, but it does not prevent this feature.

Strongly deformed light- and medium-mass nuclei in Fig. 3

depict notable triaxiality in their T-plots, likely implying that the triaxiality can be a global phenomenon. The properties of the nuclei ^{24}Mg , $^{34,36,38}\text{Mg}$ and ^{42}S are calculated with the USD [126], EEdf1 [35, 43] and SDPF-MU [127] interactions, respectively. The triaxiality of ^{24}Mg was noticed decades ago in shell-model calculations, for instance, by the USD interaction [126]. Similarly, a Skyrme-based HFB-GCM calculation displayed triaxiality after J/K projection [128]. However, there can be different aspects in the triaxiality of light nuclei compared to heavy strongly deformed nuclei discussed presently, and further investigations, particularly on possible variations of the basic and prominent triaxialities, are of interest. Very interestingly, exotic nuclei $^{34,36,38}\text{Mg}$ suggest that the triaxiality seems to be enhanced near driplines, shedding light on the relation between the dripline and the ellipsoidal shapes [35, 43].

As already mentioned, a number of medium-mass nuclei also exhibit features of the triaxial shapes, e.g., in ^{66}Zn [50], $^{74,76}\text{Zn}$ [51], ^{76}Ge [52] and ^{78}Se [53], but these nuclei depict modest ellipsoidal deformation, as not included in Fig. 3. Their structures will be discussed in the near future in the light of the present study. In particular, it is of great interest to see in what manner the concept of the prominent triaxiality evolves, including its origin, in such weakly deformed nuclei with large γ values like 30° . It is evident that degrees of freedom other than ellipsoidal deformation contribute more in such cases, and some other correlations due to nuclear forces may show up. The CI calculation with realistic interactions might be advantageous, as another important question arises as to how strongly K -mixings occur due to substantially smaller β_2 (or $E_x(2_1^+) \gtrsim 0.5$ MeV) and larger γ .

Figure 3 suggests that nine nuclei, ^{100}Sr , $^{102,104,106}\text{Zr}$, ^{106}Mo , ^{122}Ce , $^{128,130}\text{Nd}$, ^{132}Sm , are strongly deformed in the criterion there. The triaxiality has already been investigated by MCSM calculations including T-plots for the first five nuclei ($Z < 50$), as will be reported elsewhere [130], where the triaxiality appears more strongly in quite a few Zr isotopes than in the earlier study [27]. It is of interest that all these five nuclei are exotic neutron-rich isotopes with short lifetimes. The structure of other weakly deformed nuclei will be studied as well, also from the viewpoint of a shell-model approach to so-called γ -soft nuclei with $Z \sim 54$ [88].

The applications of the formulas of rotational excitation energies to objects other than atomic nuclei are plausible and indeed of great interest. We already see that higher-order terms in chemistry [7] can be justified. It is also of major interest to explore, in other physical systems, applications of the present views may open a new understanding. The basic triaxiality due to the symmetry restoration might emerge in triatomic molecules as an explanation of the bending configuration. Possible effects similar to the ones by the nuclear tensor force may be found: the interaction between electric dipole moments, carried possibly by molecules, depicts such similarity and may show up in microclusters of water molecules, metal molecules, *etc.*

The present underlying picture of the shapes and the rotations can be applied not only to fermionic systems but also to bosonic systems. The Interacting Boson Model (IBM) of

Arima and Iachello describes the structure of deformed nuclei [129]. It is of interest as to how the findings obtained in this work, especially those in Secs. 4 and 5, can work with bosons. For instance, the IBM shows no triaxial minimum in unprojected PES, and it is now an intriguing question as to whether the K projection may change this feature or not.

We finally address that the preponderance of triaxiality in heavy nuclei was suggested by an Ukrainian physicist, A. S. Davydov (Crimea 1912 - Kyiv 1993). This suggestion, especially for heavy strongly deformed nuclei discussed in this paper, has been appreciated, not to an adequate extent in the present view. Putting the unsuccessful energy predictions by the triaxial-rotor-model aside, his idea of the triaxial deformation as the general trend of nuclear shape turned out to be a superb and correct idea, and can be appreciated more appropriately. Pioneer experimental works with Multiple Coulomb Excitation by D. Cline are to be better appreciated as well.

Acknowledgements

The authors are grateful to Drs. P. Van Duppen, N. Pietralla, P. von Neumann-Cosel, A. Tamii, G. Giacalone, P. Ring, D. Vretenar, K. Nishio, Y. Aritomo, T. Azuma, K. Yabana and S. Yamamoto for valuable suggestions and/or discussions. TO thanks the Alexander von Humboldt Foundation for the Research Award, as the associated stay in Darmstadt resulted in some parts of this work. TO is grateful to Prof. N. Nagaosa for generous understanding and precious comments. The MCSM calculations were performed on the supercomputer Fugaku at RIKEN AICS (hp190160, hp200130, hp210165, hp220174, hp230207, hp240213). This work was supported in part by MEXT as "Priority Issue on Post-K computer" (Elucidation of the Fundamental Laws and Evolution of the Universe) (hp160211, hp170230, hp180179, hp190160) and "Program for Promoting Researches on the Supercomputer Fugaku" (Simulation for basic science: from fundamental laws of particles to creation of nuclei) (JPMXP1020200105, JPMXP1020230411), and by JICFuS. This work was supported by JSPS KAKENHI Grant Numbers JP19H05145, JP21H00117, JP21K03564, JP20K03981, JP17K05433 and JP18H05462.

AUTHOR CONTRIBUTIONS

T.O. promoted the whole study and wrote the manuscript; Y.T. performed the CI calculations, drew T-plots and contributed to code development and in-depth discussions; N.S. made the main part of the computer codes; Y.U. gave various crucial remarks; T.A., P.V.D. and H.U. made valuable discussions. All authors discussed the results and commented on the manuscript.

Appendix A: Configuration Interaction (CI) calculation or Shell-model calculation

We sketch the shell model for atomic nuclei in this Appendix. The shell-model calculation is one of the standard methods for the nuclear many-body problem [4, 12, 21, 131]. It belongs to the category of the Configuration Interaction (CI) calculation, which is more familiar to a broad audience and is also used in this article for the meaning of the shell model. The ingredients of the shell model are (i) single-particle orbitals and their energies, (ii) the numbers of protons and neutrons in these orbitals, (iii) nucleon-nucleon (NN) interaction. Thus, the properties of the nuclear states are determined by them, without other a priori assumptions. The protons and neutrons can move in these orbitals, scattering each other through the NN interaction adopted. These protons and neutrons do not include the nucleons in the inert core, as it is a closed shell and is treated as a vacuum. The single-particle energies (SPE) and the NN interaction are taken from some models and/or theories. The matrix elements of the SPE and the NN interaction are expressed, as one- and two-body operators, respectively, with respect to all possible combinations of single-particle states, which are magnetic substates of each single-particle orbital.

The Hamiltonian consists of one-body term and two-body term, as usual. The one-body term is expressed by the SPEs, and the two-body term is expressed in terms of the matrix elements of the NN interaction with respect to antisymmetrized two-nucleon states. The Hamiltonian is thus constructed, and the actually used Hamiltonian is mentioned in the main text.

The many-body states are described by superpositions of Slater determinants in many *conventional* shell-model calculations. The many-body Schrödinger equation is solved for the given Hamiltonian as,

$$H\Psi = E\Psi, \quad (\text{A1})$$

where Ψ is an eigenstate for an eigenvalue E , and the Hamiltonian *matrix* for this many-body system is represented by matrix elements of the Hamiltonian *operator* for all combinations (bra and ket vectors) of all possible Slater determinants. By diagonalizing this Hamiltonian matrix, energy eigenvalues and wave functions of eigenstates are obtained. We can calculate various physical quantities from these wave functions. The number of Slater determinants is called the shell model dimension. This is the general framework of the shell model, while many-body states can be equivalently expressed otherwise.

The shell model dimension becomes huge in many interesting cases, restricting the actual feasibility of the calculation. This is the major obstacle of the conventional shell-model calculation, and the current limit of the shell-model dimension is around 10^{11} as of 2019 [132]. In order to overcome this difficulty, the Monte Carlo Shell Model was introduced, as described in the next Appendix.

The practical setup of the present work is mentioned [33]. Proton single-particle orbitals are, $1g_{9/2,7/2}$, $2d_{5/2,3/2}$, $3s_{1/2}$, $1h_{11/2}$, $2f_{7/2}$, and $3p_{3/2}$. The neutron single-particle orbitals are, $1h_{11/2,9/2}$, $2f_{7/2,5/2}$, $3p_{3/2,1/2}$, $1i_{13/2}$, $2g_{9/2}$, $3d_{5/2}$ and $4s_{1/2}$. These orbitals define the model space, which is built on top of

the $Z=40$ and $N=70$ magic numbers of the harmonic oscillator potential. In the case of ^{166}Er , 28 protons and 28 neutrons are put into the model space formed by these orbitals. The model space and the number of nucleons are much larger than those in the usual shell-model calculation so that the shape deformation can be described. The shell-model dimension becomes as large as 4.8×10^{33} for the case of ^{166}Er . This is far beyond the limit of the conventional shell-model calculation but can be overcome by using the MCSM described in the next Appendix.

Appendix B: Monte Carlo Shell Model and T-plot

In this Appendix, we briefly describe the Monte Carlo Shell Model (MCSM). The MCSM was initially proposed in Ref. [24]. A prototype of its present version was shown in Ref. [25]. The method and applications of the MCSM were reviewed, for instance, in Refs. [23, 26]. The MCSM is the methodology fully exploited in this work. Although this work uses the advanced version of MCSM, we here outline its earlier version, for simplicity. It is formulated with Slater determinants as the basis vectors, similar to the conventional shell-model calculation. However, the Slater determinants are not the same as those used in the conventional shell-model calculation. In the conventional one, each Slater determinant is a direct product of some single-particle states, each of which is a magnetic substate of the single-particle orbital.

An MCSM eigenstate is schematically written as (see Ref. [62] for more detailed but pedagogical concise explanation),

$$\Psi = \sum_k f_k \hat{\mathcal{P}}_{J^P} \phi_k, \quad (\text{B1})$$

where f_k denotes the amplitude, $\hat{\mathcal{P}}_{J^P}$ means the projection operator on to the spin/parity J^P (this part is more complicated in practice), and ϕ_k stands for Slater determinant called (k -th) MCSM basis vector: $\phi_k = \Pi_i a_i^{(k)\dagger} |0\rangle$. Here, $|0\rangle$ is the inert core (closed shell), $a_i^{(k)\dagger}$ refers to a superposition,

$$a_i^{(k)\dagger} = \sum_n D_{n,i}^{(k)} c_n^\dagger, \quad (\text{B2})$$

with c_n^\dagger being the creation operator of a usual single-particle state, for instance, that of the HO potential, and $D_{n,i}^{(k)}$ denoting a matrix element. By choosing an optimal matrix $D^{(k)}$, we can select ϕ_k so that such ϕ_k better contributes to the lowering of the corresponding energy eigenvalue. Thus, the determination of $D^{(k)}$ is the core of the MCSM calculation. The index k runs up to 50-100, but can be more. These are much smaller than the dimension of the many-body Hilbert space, which is 4.8×10^{33} for the case of ^{166}Er , as already mentioned.

Thus, the basis vectors of the MCSM calculation are composed of “stochastically - variationally deformed” single-particle states. The adopted basis vectors are mutually independent, otherwise there is no energy gain. By having a set of these MCSM basis vectors thus fixed, we diagonalize the Hamiltonian and obtain energy eigenvalues and eigenstates.

A large number of MCSM calculations have been performed as exemplified in Refs. [27–37, 44, 66].

Besides the breakthrough in the computational limit, the MCSM also has the advantage of providing a very useful way to visualize the intrinsic shape of each MCSM eigenstate through what is called the T-plot [44, 66]. Because the MCSM basis vector is a deformed Slater determinant, one can calculate its intrinsic quadrupole moments, *i.e.* the quadrupole moments in the body-fixed frame, denoted as Q_0 and Q_2 . They can be expressed by two parameters β_2 and γ , as described in the main text. The importance of each MCSM basis vector to a given eigenstate (its overlap probability in the MCSM eigenstate) is represented by the size (area) of its circular symbol in the T-plot. The T-plot can be made on the β_2 - γ plane, but is usually on the PES, and intuitively exhibits the underlying physical pictures for the states of interest, as demonstrated in a variety of studies, *e.g.* in Refs. [27–31, 33, 34, 37].

We stress that the T-plot played a major role in the present study, displaying not only the triaxial shapes of the eigenstates but also their rigidity over different eigenstates.

As mentioned at the beginning of this Appendix, the present calculation was performed by the most advanced methodology of the MCSM. This is called Quasiparticle Vacua Shell Model (QVSM) [38]. In the original version of the MCSM, the pairing correlations are mainly incorporated by superposing different MCSM basis vectors, which are deformed Slater determinants as stated above. The QVSM basis vectors are somewhat like a Hartree-Fock-Bogoliubov ground state (which is a generalization of the BCS ground state), and this feature enables each QVSM basis vector to contain both effects of the deformed mean field and effects of the pairing correlations. This advantage is particularly exploitable for heavy nuclei where the pairing correlations over different single-particle orbitals become more important than for lighter nuclei. In the original MCSM, the pairing correlations are largely carried by superpositions of different MCSM basis vectors. As the QVSM calculation is computationally heavier, this merit makes sense for some nuclei heavier than $A \sim 100$.

The spurious center-of-mass motion is removed to a sufficient extent by the Lawson method [133].

Appendix C: K projection

We here present some detailed discussion on the K projection. The K -projected state was defined in eq. (10) as,

$$\Phi[\phi, K] = \frac{1}{N_K} \frac{1}{2\pi} \int_0^{2\pi} d\gamma e^{i\gamma(\hat{J}_z - K)} \phi, \quad (C1)$$

where γ is the angle in the xy plane, and N_K is a normalization constant with an arbitrary phase factor,

$$|N_K|^2 = \frac{1}{2\pi} \int_0^{2\pi} d\gamma \langle \phi | e^{i\gamma(\hat{J}_z - K)} | \phi \rangle. \quad (C2)$$

We introduce the norm kernel,

$$n(\gamma) = \langle \phi | e^{i\gamma\hat{J}_z} | \phi \rangle. \quad (C3)$$

Although $n(\gamma)$ looks like a complex number, it is a real number with the time reversal symmetry by the following reason. The intrinsic state is expanded by components of definite K values, $K=0, \pm 1, \pm 2, \dots$. In calculating the norm kernel, the magnitudes of amplitudes in this expansion are considered to remain unchanged for the exchange of the signs of K values, *i.e.*, K and $-K$. This property originates in the time reversal symmetry which is conserved in eigenstates. Likewise, matrix elements of the Hamiltonian to be discussed shortly are real.

The cases with γ and $2\pi - \gamma$ are equivalent because of the same relative angle, and only a phase factor may come in. For the real norm kernel, $n(\gamma) = n(2\pi - \gamma)$ holds because of no phase ambiguity for a real number. Eq. (C2) is then rewritten as

$$\begin{aligned} |N_K|^2 &= \frac{1}{2\pi} \int_0^{2\pi} d\gamma e^{-i\gamma K} n(\gamma), \\ &= \frac{1}{2\pi} \int_0^{2\pi} d\gamma \cos(K\gamma) n(\gamma), \end{aligned} \quad (C4)$$

with $|N_K|$ being the same for both signs of K . The state ϕ is assumed, in this study, to have a positive parity, and the projection actually implies the K^+ projection.

The weighting factor in the integral of eq. (C4) is $\cos(K\gamma)$. The $K=0$ projection is simple, where contributions from all γ angles are equally superposed as

$$\Phi[\phi, K=0] = \frac{1}{N_0} \frac{1}{2\pi} \int_0^{2\pi} d\gamma e^{i\gamma\hat{J}_z} \phi. \quad (C5)$$

For $K=2$, however, this factor takes values such as 1, 0, -1, 0, 1, respectively, for $\gamma = 0, \pi/4, \pi/2, 3\pi/4, \pi$. This is in contrast to the unity factor for $K=0$ (see eq. (C5)).

Considering that H is invariant under the rotation, the expectation value of the Hamiltonian H is given for $K=0$ by

$$\begin{aligned} h_{K=0} &= \langle \Phi[\phi, K=0] | H | \Phi[\phi, K=0] \rangle \\ &= \frac{1}{|N_0|^2} \frac{1}{2\pi} \int_0^{2\pi} d\gamma \langle \phi | H | e^{i\gamma\hat{J}_z} \phi \rangle. \end{aligned} \quad (C6)$$

Introducing the energy kernel similarly to the norm kernel,

$$h(\gamma) = \langle \phi | H e^{i\gamma\hat{J}_z} | \phi \rangle, \quad (C7)$$

we obtain

$$h_{K=0} = \frac{1}{|N_0|^2} \frac{1}{2\pi} \int_0^{2\pi} d\gamma h(\gamma). \quad (C8)$$

Like the norm kernel, $h(\gamma)$ is a real quantity if the time-reversal symmetry holds.

For $K \neq 0$, we obtain

$$\begin{aligned} h_K &= \langle \Phi[\phi, K] | H | \Phi[\phi, K] \rangle \\ &= \frac{1}{|N_K|^2} \frac{1}{2\pi} \int_0^{2\pi} d\gamma \langle \phi | H | e^{i\gamma(\hat{J}_z - K)} \phi \rangle \\ &= \frac{1}{|N_K|^2} \frac{1}{2\pi} \int_0^{2\pi} d\gamma e^{iK\gamma} h(\gamma), \\ &= \frac{1}{|N_K|^2} \frac{1}{2\pi} \int_0^{2\pi} d\gamma \cos(K\gamma) h(\gamma). \end{aligned} \quad (C9)$$

where a similar argument to eq. (C4) is used.

We look into contributions in eq. (C8). By introducing a complete set of states orthogonal to ϕ denoted by ζ 's, we decompose $h_{K=0}$ into the diagonal and off-diagonal contributions as

$$\begin{aligned}
 h_{K=0} &= \frac{1}{|\mathcal{N}_0|^2} \frac{1}{2\pi} \int_0^{2\pi} d\gamma \\
 &\quad \left\{ \langle \phi | H | \phi \rangle \langle \phi | e^{i\gamma \hat{J}_z} | \phi \rangle + \sum_{\zeta} \langle \phi | H | \zeta \rangle \langle \zeta | e^{i\gamma \hat{J}_z} | \phi \rangle \right\} \\
 &= \langle \phi | H | \phi \rangle \\
 &\quad + \frac{1}{|\mathcal{N}_0|^2} \frac{1}{2\pi} \int_0^{2\pi} d\gamma \sum_{\zeta} \langle \phi | H | \zeta \rangle \langle \zeta | e^{i\gamma \hat{J}_z} | \phi \rangle \\
 &= \langle \phi | H | \phi \rangle + \frac{1}{|\mathcal{N}_0|^2} \frac{1}{2\pi} \int_0^{2\pi} d\gamma \left\{ h(\gamma) - h(\gamma=0) n(\gamma) \right\}.
 \end{aligned} \tag{C10}$$

The first term on the right-hand-side (RHS) is the expectation value with respect to ϕ and provides a major contribution. It is often called unprojected energy. The state ϕ is, however, not an eigenstate of H in general, and the second term then does not vanish. The only exception arises for $\gamma=0$; no ζ is generated by the operation $e^{i\gamma \hat{J}_z}$.

Figure 26 shows actual values of the norm kernel, $n(\gamma)$, and the energy kernel, $h(\gamma)$, obtained from the state ξ_0 in the discussion for ^{166}Er in Sec. 3.4 (the most important basis vector for the ground state). As expected, $n(\gamma)$ decreases from $n(\gamma=0)$ as γ increases. Likewise, the magnitude of $h(\gamma)$ decreases, but the γ dependence is not equal between the two.

Figure 27 (a) shows the quantity $h(\gamma) - h(\gamma=0) n(\gamma)$, which appears in the integrand of the RHS of eq. (C10). This quantity remains negative (more binding) for the whole region of γ . This gives more binding energy to the $K=0$ state, as an average of this quantity becomes the change of the energy of the $K=0$ state. Figure 27 (b) shows the energies of K -projected states. It indicates that the $K=0$ state gains the binding energy by about 4 MeV from the unprojected energy.

The contribution represented by the quantity, $h(\gamma) - h(\gamma=0) n(\gamma)$, thus provides additional substantial binding energy to triaxial states, while it vanishes for the states of no triaxiality (as far as the quadrupole degree of freedom is concerned). The underlying origin of this binding energy gain is different γ dependences of the two kernels, $n(\gamma)$ and $h(\gamma)$. The magnitude of the latter decreases more gradually as a function of γ than the former, probably because various correlations from the NN interaction, including finite-range attraction, blur displacement effects between bra and ket vectors, and hence weaken the effects of decreasing overlaps represented by $n(\gamma)$. We note that this is an effect for a given triaxiality or a given value of the deformation parameter γ , but also that the amount of this effect varies as the triaxiality changes.

It is of interest what contribution the same term produces for $K \neq 0$. The quantity h_K is rewritten in a similar way to eq. (C10) as

$$h_K = \langle \phi | H | \phi \rangle$$

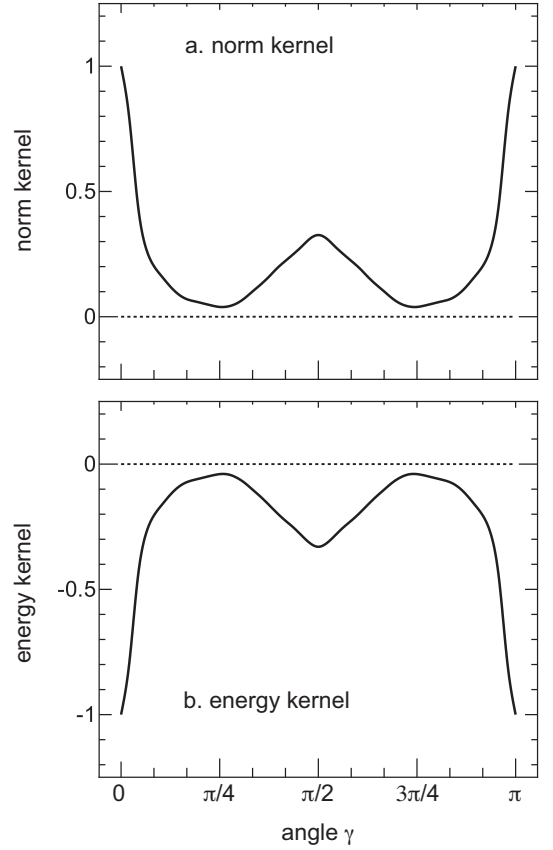


FIG. 26. **a** norm kernel and **b** energy kernel as functions of the angle γ in radian. Each kernel value is scaled by the magnitude of the original value at $\gamma=0$. The case of ^{166}Er is taken.

$$+ \frac{1}{|\mathcal{N}_K|^2} \frac{1}{2\pi} \int_0^{2\pi} d\gamma \cos(K\gamma) \left\{ h(\gamma) - h(\gamma=0) n(\gamma) \right\}. \tag{C11}$$

The first term on the RHS is again the unprojected energy, and the K dependence is carried by the second term.

We first discuss the $K=2$ case. The factor $\cos(2\gamma)$ in eq. (C11) varies from 1 for $\gamma=0$, to 0 for $\gamma=\pi/2$ and -1 for $\gamma=\pi$. This is in stark contrast to a constant factor eq. (C10). The quantity, $-\{h(\gamma)/h(\gamma=0) - n(\gamma)\}$, is shown in Fig. 27 (a). This quantity keeps the sign of $h(\gamma)$, and exhibits deviations of the relative change, $h(\gamma)/h(\gamma=0)$, from $n(\gamma)$, as $n(\gamma=0)=1$. It remains negative (attractive) for the entire region of γ , but is multiplied by $\cos(2\gamma)$, which flips between opposite signs. Thus, a certain cancellation occurs, and the net effect becomes less attractive. This pushes up the excitation energy of the $K=2$ (projected) state relative to the $K=0$ state, being consistent with Fig. 6. Fig. 27 (b) also displays the energy of the $K=2$ (projected) state, which is about 2 MeV above the $K=0$ (projected) state. On the other side, the $K=2$ energy is well below the unprojected energy, implying the triaxiality gives a substantial amount of the binding energy also to the $K=2$ state.

For states of other K values, the energies can be similarly calculated, with more frequently changing multiplication fac-

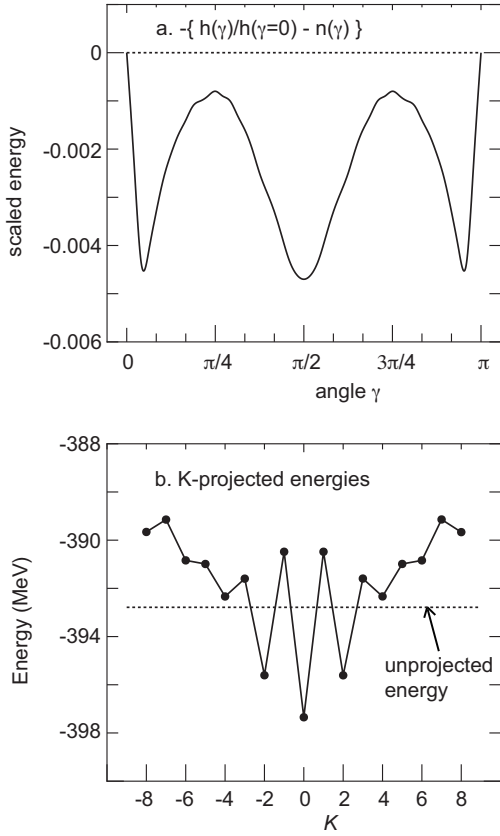


FIG. 27. a. $-\{h(\gamma)/h(0) - n(\gamma)\}$ with parity projection and b. energies of K^+ -projected states. The unprojected energy (with parity projection) is shown by a dotted horizontal line.

tors. Figure 27 (b) shows the energies of such K -projected states. For $K=4$, the $\cos(4\gamma)$ factor causes cancellations so severe as to result in almost no net additional binding energy. For $K=1$, there are cancellations between contributions from $\gamma \sim 0$ and $\gamma \sim \pi$. For higher K values, the factors make the contribution even more positive (repulsive), placing the energies of such states above the unprojected ones.

Appendix D: Analysis with reduced monopole interaction

Figure 28a displays enlarged details of the PES near the minimum of Fig. 5b. Here, it is reminded that the unprojected solution is calculated by the constrained HFB with the particle number projection and the $J^P=0^+$ projection is performed on this unprojected solution. This process is usually called VBP (Variation Before Projection). The PES minimum of the original Hamiltonian (panel a) is located at $\gamma \sim 10^\circ$ and its energy is lower by ~ 0.4 MeV than the lowest point with $\gamma=0^\circ$ (prolate shape). This is consistent with the trend shown in Fig. 7, where a cut is made with $\beta_2 \sim 0.3$.

The CI results indicate that the ground state of ^{166}Er contains, as expectation values, about four protons in $1h_{11/2}$ and about four neutrons in $1h_{9/2}$, with which a substantial triaxiality is generated as suggested in Subsec. 6.5, and the extra

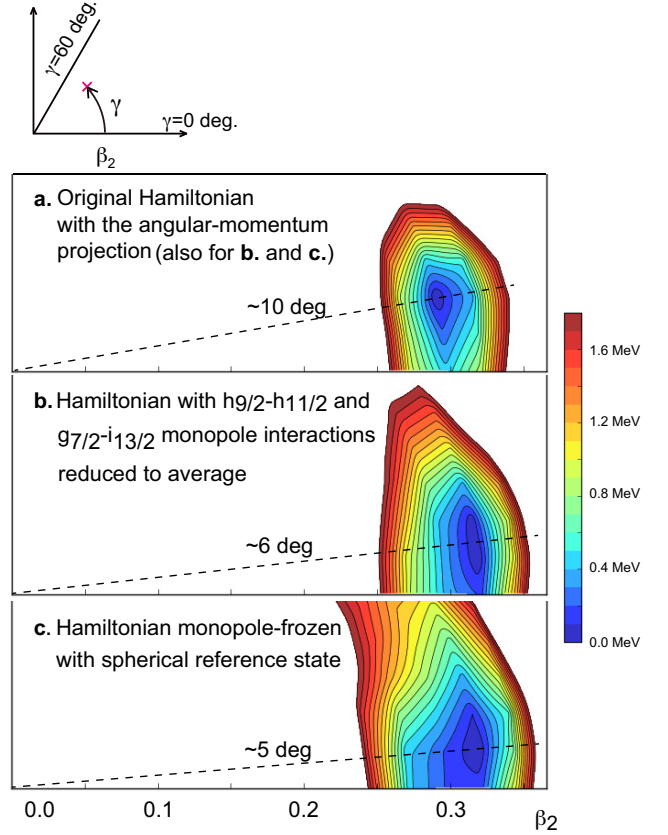


FIG. 28. PES near the minimum by the constrained HFB with the projection on to $J^P=0^+$ afterward (VBP). The calculations are made with **a** the original Hamiltonian, **b** the Hamiltonian where two crucially strong monopole interactions, such as the one in Fig. 12, are reduced to the average strength, **c** the Hamiltonian monopole-frozen with spherical HFB reference state. Dashed lines are drawn to show representative γ angles.

monopole effect beyond the average one reaches about -2.2 MeV, a substantial additional binding. A similar but weaker effect arises from the (proton $1g_{7/2}$, neutron $1i_{13/2}$) combination. These effects trigger the triaxiality, and combined effects including other orbitals produce the triaxial minimum in the unprojected PES just mentioned, and this triaxiality is consistent with T-plot circles around $\gamma=9^\circ$ shown in Fig. 5c.

In order to examine this monopole-quadrupole interplay, pn monopole matrix elements, $v_{1h_{11/2}, 1h_{9/2}}^{\text{mono}}$ and $v_{1g_{7/2}, 1i_{13/2}}^{\text{mono}}$, are reduced to the average value, -0.25 MeV (see Subsec. 6.5). This implies that for these channels, the tensor force is completely off, and the central force is weakened. Figure 28b shows the result of this monopole-reduced Hamiltonian: the minimum is shifted to $\gamma \sim 6^\circ$ with the energy only ~ 0.2 MeV below the (axially-symmetric prolate) minimum at $\gamma=0^\circ$. This trend is confirmed by the T-plot in Fig. 5d, which displays the movement of T-plot circles towards a prolate shape. The mean γ value is changed down to 1.5° , and is closer to $\gamma=0^\circ$ than the HFB minimum point, primarily due to correlations incorporated by the CI calculation.

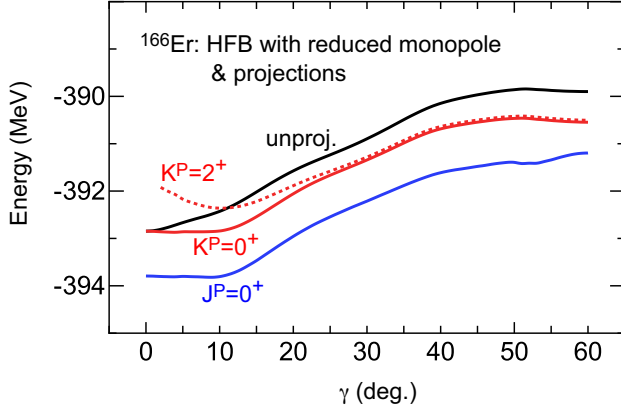


FIG. 29. Energies of the ground state of ^{166}Er given by the “reduced monopole” treatment by HFB calculations. See the caption of Fig. 7.

More striking features are presented in Fig. 29, where the results of the HFB calculations are shown similarly to Fig. 7 with the present monopole-reduced Hamiltonian. The unprojected energy is raised rapidly from $\gamma=0^\circ$. While Fig. 7 depicts a flat bed with a slight decrease up to $\gamma=7^\circ$, this flat bed is completely gone in Fig. 29, and the continuous increase from $\gamma=0^\circ$ appears to be the pattern expected in the conventional view. The lowering caused by the K projection produces just a flat bed with a subtle minimum at $\gamma \approx 7^\circ$. We mention that the flat bed in Fig. 7 is a consequence of the self-organization by the monopole interaction contained in the full Hamiltonian.

A comparison between Fig. 7 and Fig. 29 clearly exhibits clear differences in the basic γ dependence near the energy minima and in the overall energy gain. The latter includes steeper slope between $\gamma \sim 10^\circ$ to $\gamma \sim 40^\circ$ in Fig. 7 than in Fig. 29. We note that the occupation numbers differ between the two calculations for proton $1h_{11/2}$, neutron $1h_{9/2}$ and $1i_{13/2}$ orbitals, as expected from large differences in related monopole interactions. For instance, the occupation numbers of these orbitals at $\gamma = 10^\circ$ are higher by 0.4-0.8 with the full Hamiltonian than those with the monopole-reduced Hamiltonian.

Appendix E: Analysis with Monopole-Frozen interaction

As another way to see unique contribution of the monopole interaction, we calculate mean shifts of the SPEs by taking expectation values of $n_j^{(p)}$ etc. in eq. (69) etc. with a reference state. We then remove the monopole interaction and instead include such mean shifts of the SPEs. Namely, dynamical effects of the monopole interaction are *frozen* with this reference state [33]. The CI calculation is then performed. Presently, a spherical state, given by constrained HFB calculations, is used as the reference state. Figure 28c exhibits the PES of this *monopole-frozen* Hamiltonian. The minimum is even closer to the prolate line than in panels a,b. Figure 5e displays the T-plot of the 0_1^+ state obtained by the same monopole-frozen Hamiltonian. The strong deformation remains, but the triaxi-

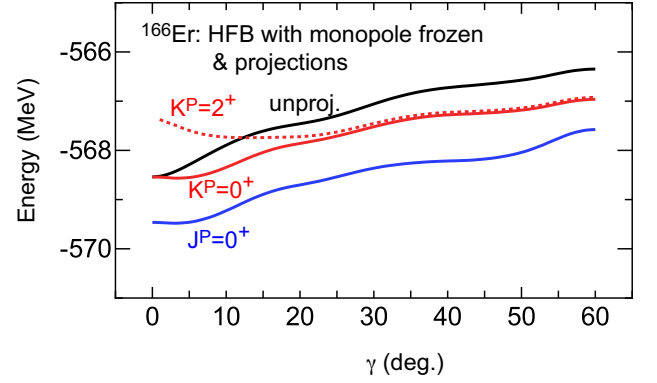


FIG. 30. Energies of the ground state of ^{166}Er given by the “monopole frozen” treatment of HFB calculations. See the caption of Fig. 7.

ality almost disappears. This further confirms that the activation of the monopole interaction is crucial for the triaxiality of ^{166}Er . This feature is found for other nuclei (see Fig. 14).

Figure 30 shows the HFB results obtained with this monopole-frozen Hamiltonian, like Fig. 29. The unprojected energy increases more rapidly from $\gamma=0^\circ$ than in Fig. 29. The energy minimum around $\gamma=9^\circ$ is moved to around $\gamma=3^\circ$. The mean γ value is somewhat smaller in the CI calculation, being 1.1° . The lowering shown by the K projection remains but can produce a narrow flat bed, even narrower than in Fig. 29. This trend is consistent with the T-plot in Fig. 5e. We emphasize that the minimum as a function of γ in the PES is not around $\gamma=0^\circ$ but around $\gamma=3^\circ$ after the K projection, which is basically maintained by the J projection. We also note that the energy comes down as γ decreases from 60° , but the gain is smaller than those in Fig. 7 or Fig. 29. This implies that not only local but also global effects of the monopole interaction as a function of γ may not be well simulated by playing with the SPE values.

REFERENCES

1. Rainwater, J., Nuclear energy level argument for a spheroidal nuclear model, *Phys. Rev.* **79**, 432 (1950).
2. Bohr, A., The Coupling of Nuclear Surface Oscillations to the Motion of Individual Nucleons, *Mat. Fys. Medd. Dan. Vid. Selsk.* **26**, 14 (1952).
3. Bohr, A. Mottelson, B. R., *Collective and Individual-Particle Aspects of Nuclear Structure*, *Mat. Fys. Medd. Dan. Vid. Selsk.* **27**, 16 (1953).
4. Ring, P., Schuck, P., *The Nuclear Many-Body Problem*, (Springer-Verlag: Berlin, 1980).
5. Bohr, A. & Mottelson, B.R., *Nuclear Structure* (Benjamin, New York, 1975), Vol. II.
6. Bohr, A. Rotational Motion in Nuclei. In *Nobel Lectures, Physics 1971–1980*, Lundqvist S., Ed.; World Scientific: Singapore, 1992; pp. 213–232; <https://www.nobelprize.org/prizes/physics/1975/bohr/facts/>.
7. Atkins, P., de Paula, J., Keeler J., *Physical Chemistry* (Oxford University Press, Oxford, 2018).

8. National Nuclear Data Center. NuDat 3.0.
<https://www.nndc.bnl.gov/nudat3/>
9. Jahn, H. A., Teller, E., Stability of Polyatomic Molecules in Degenerate Electronic States I - Orbital Degeneracy, *Proc. R. Soc. A*, **161**, 220, (1937).
10. Rowe, D. J., Nuclear collective motion:: models and theory, (World Scientific, Singapore, 2010).
11. Bohr, A. & Mottelson, B.R. Nuclear Structure (Benjamin, New York, 1969), Vol. I.
12. De Shalit, A., Feshbach, H., Nuclear Structure (theoretical Nuclear Physics), (John Wiley and Sons, New York, 1974).
13. Nix, J. R., Further studies in the liquid-drop theory of nuclear fission, *Nucl. Phys. A* **130**, 241 (1969).
14. Ichikawa, T., Iwamoto, A., Möller, P., Sierk, A. J., Contrasting fission potential-energy structure of actinides and mercury isotopes, *Phys. Rev. C* **86**, 024610 (2012).
15. Möller, P., Nix, R., Myers, W. D., Swiatecki, W. J., Nuclear ground-state masses and deformations, *At. Data Nucl. Data Tables* **59**, 185 (1995).
16. Möller, P., Bengtsson, R., Carlsson, G., Olivius, P., Ichikawa, T., Global Calculations of Ground-State Axial Shape Asymmetry of Nuclei, *Phys. Rev. Lett.* **97**, 162502 (2006).
17. Kumar, K., & Baranger, M., Nuclear deformations in the pairing-plus-quadrupole model (III). Static nuclear shapes in the rare-earth region, *Nucl. Phys. A* **110**, 529 (1968). *Proc. R. Soc. A*, **161** 220, (1937).
18. Bes, D.R., & Sorensen, R.A., The Pairing-Plus-Quadrupole Model. *Advances in Nuclear Physics*, Eds: Baranger, M., & Vogt, E., (Plenum Press, New York, 1969), Vol. II.
19. Elliott, J.P., Collective motion in the nuclear shell model I. Classification schemes for states of mixed configurations, *Proc. Roy. Soc. (London) A* **245**, 128 (1958).
20. Elliott, J.P., Collective motion in the nuclear shell model II. The introduction of intrinsic wave-functions, *Proc. Roy. Soc. (London) A* **245**, 562 (1958).
21. Caurier, E., Martinez-Pinedo, G., Nowacki, F., Poves, A., Zuker, A. P., The shell model as a unified view of nuclear structure, *Rev. Mod. Phys.* **77**, 427 (2005)
22. National Nuclear Data Center. Evaluated Nuclear Structure Data File.
<http://www.nndc.bnl.gov/ensdf/>.
23. Otsuka, T., Honma, M., Mizusaki, T., Shimizu, N. & Utsuno, Y., Monte Carlo Shell Model for Atomic Nuclei, *Prog. Part. Nucl. Phys.* **47**, 319-400 (2001).
24. Honma, M., Mizusaki, T., Otsuka, T., Diagonalization of Hamiltonians for Many-Body Systems by Auxiliary Field Quantum Monte Carlo Technique, *Phys. Rev. Lett.* **75**, 1284 (1995).
25. Otsuka, T., Mizusaki, T., Honma, M., Structure of the N=Z=28 Closed Shell Studied by Monte Carlo Shell Model Calculation, *Phys. Rev. Lett.* **81**, 1588 (1998).
26. Shimizu, N. *et al.*, New-generation Monte Carlo shell model for the K computer era, *Prog. Theor. Exp. Phys.* **2012**, 01A205 (2012).
27. Togashi, T., Tsunoda, Y., Otsuka, T., & Shimizu, N., Quantum Phase Transition in the Shape of Zr isotopes, *Phys. Rev. Lett.* **117**, 172502 (2016).
28. Leoni, S., *et al.*, Multifaceted Quadruplet of Low-Lying Spin-Zero States in ^{66}Ni : Emergence of Shape Isomerism in Light Nuclei, *Phys. Rev. Lett.* **118**, 162502 (2017).
29. Togashi, T., Tsunoda, Y., Otsuka, T., Shimizu, N., & Honma, M., Novel Shape Evolution in Sn Isotopes from Magic Numbers 50 to 82, *Phys. Rev. Lett.* **121**, 062501 (2018).
30. Marsh, B. A. *et al.* Characterization of the shape-staggering effect in mercury nuclei, *Nature Physics* **14**, 1163-1167 (2018).
31. Ichikawa, Y. *et al.*, Interplay between nuclear shell evolution and shape deformation revealed by the magnetic moment of ^{75}Cu , *Nature Physics* **15**, 321 (2019).
32. Taniuchi, R. *et al.*, ^{78}Ni revealed as a doubly magic stronghold against nuclear deformation, *Nature* **569**, 53 (2019).
33. Otsuka, T., Tsunoda, Y., Abe, T., Shimizu, N., Van Duppen, P., Underlying Structure of Collective Bands and Self-Organization in Quantum Systems, *Phys. Rev. Lett.* **123**, 222502 (2019).
34. Märginean, S., *et al.*, Shape Coexistence at Zero Spin in ^{64}Ni Driven by the Monopole Tensor Interaction, *Phys. Rev. Lett.* **125**, 102502 (2020)
35. Tsunoda, N., Otsuka, T., Takayanagi, K., Shimizu, N., Suzuki, T., Utsuno, Y., Yoshida, S., & Ueno, H., The impact of nuclear shape on the emergence of the neutron dripline, *Nature* **587**, 66 (2020).
36. Abe, T., Maris, P., Otsuka, T., Shimizu, N., Utsuno, Y., Vary, J. P., Ground-state properties of light $4n$ self-conjugate nuclei in ab initio no-core Monte Carlo shell model calculations with nonlocal NN interactions, *Phys. Rev. C* **104**, 054315 (2021).
37. Otsuka, T., Abe, T., Yoshida, T., Tsunoda, Y., Shimizu, N., Itagaki, N., Utsuno, Y., Vary, J., Maris, P., Ueno, H., α -Clustering in atomic nuclei from first principles with statistical learning and the Hoyle state character, *Nature Communications* **13**, 2234 (2022).
38. Shimizu, N., Tsunoda, Y., Utsuno, Y., Otsuka, T., Variational approach with the superposition of the symmetry-restored quasiparticle vacua for nuclear shell-model calculations, *Phys. Rev. C* **103**, 014312 (2021).
39. Otsuka, T., Suzuki, T., Honma, M., Utsuno, Y., Tsunoda, N., Tsukiyama, K., and Hjorth-Jensen, M., Novel features of nuclear forces and shell evolution in exotic nuclei, *Phys. Rev. Lett.* **104**, 012501 (2010).
40. Osterfeld, F., Nuclear spin and isospin excitations, *Rev. Mod. Phys.* **64**, 491 (1992)
41. Brown, B. A., Double-Octupole States in ^{208}Pb , *Phys. Rev. Lett.* **85**, 5300 (2000).
42. Utsuno, Y., Shimizu, N., Otsuka, T., Yoshida, T., Tsunoda, Y., Nature of Isomerism in Exotic Sulfur Isotopes. *Phys. Rev. Lett.*, **114**, 032501 (2015).
43. Otsuka, T., Shimizu, N., Tsunoda, Y., Moments and radii of exotic Na and Mg isotopes. *Phys. Rev. C* **105**, 014319 (2022).
44. Tsunoda, Y., Otsuka, T., Shimizu, N., Honma, M., Utsuno, Y., Novel shape evolution in exotic Ni isotopes and configuration-dependent shell structure, *Phys. Rev. C* **89**, 031301(R) (2014).
45. Samorajczyk-Pysk, J., *et al.*, Low-spin levels in ^{140}Sm : Five 0^+ states and the question of softness against nonaxial deformation, *Phys. Rev. C* **104**, 024322 (2021).
46. Tsunoda, Y., Otsuka, T., Triaxial rigidity of ^{166}Er and its Bohr-model realization, *Phys. Rev. C*, **103**, L021303 (2021).
47. Kumar, K., Intrinsic Quadrupole Moments and Shapes of Nuclear Ground States and Excited States, *Phys. Rev. Lett.* **28**, 249 (1972).
48. Davydov, A.S., Filippov, G.F., Rotational states in even atomic nuclei, *Nucl. Phys.* **8**, 237 (1958).
49. Davydov, A.S., Rostovsky, V.S., Relative transition probabilities between rotational levels of non-axial nuclei. *Nucl. Phys.* **12**, 58 (1959).
50. Rocchini, M., *et al.*, Onset of triaxial deformation in ^{66}Zn and properties of its first excited 0^+ state studied by means of Coulomb excitation, *Phys. Rev. C* **103**, 014311 (2021).
51. Illana, A., *et al.*, Coulomb excitation of $^{74,76}\text{Zn}$, *Phys. Rev. C* **108**, 044305 (2023).

52. Ayangeakaa, A. D., *et al.*, Evidence for Rigid Triaxial Deformation in ^{76}Ge from a Model-Independent Analysis, *Phys. Rev. Lett.*, **123**, 102501 (2019).
53. Hayakawa, T., Toh, Y., Oshima, M., *et al.*, Projectile Coulomb excitation of ^{78}Se , *Phys. Rev. C* **67**, 064310 (2003).
54. Edmonds, A. R., *Angular Momentum in Quantum Mechanics*, (Princeton University Press, Princeton, 1957).
55. Here, by $\gamma=0^\circ$, we symbolically mean a perfect invariance for the rotation about the z axis. If other deformation modes occur, more conditions are needed. Such details are omitted for simplicity.
56. Satula, W., Wyss, R. A., Mean-field description of high-spin states, *Rep. Prog. Phys.* **68**, 131 (2005).
57. Papenbrock, T., Effective theory for deformed nuclei, *Nucl. Phys. A* **852**, 36 (2011).
58. Peierls, R. E., Yoccoz, J., The Collective Model of Nuclear Motion, *Proc. Phys. Soc. A* **70**, 381 (1957).
59. Kamlah, A., An Approximation for Rotation-Projected Expectation Values of the Energy for Deformed Nuclei and a Derivation of the Cranking Variational Equation, *Z. Phys.* **216**, 52 (1968).
60. Poves, A., and A. Zuker, Theoretical spectroscopy and the fp shell, *Phys. Rep.* **70**, 235 (1981).
61. Otsuka, T., Gade, A., Sorlin, O., Suzuki, T., Utsuno, Y., Evolution of shell structure in exotic nuclei, *Rev. Mod. Phys.* **92**, 015002 (2020).
62. Otsuka, T., Emerging concepts in nuclear structure based on the shell model, *Physics* **4**, 258 (2022), <https://www.mdpi.com/2624-8174/4/1/18>.
63. Otsuka, T., Suzuki, T., Fujimoto, R., Grawe, H., Akaishi, Y., Evolution of the nuclear shells due to the tensor force, *Phys. Rev. Lett.* **95**, 232502 (2005).
64. Federman, P., Pittel, S., Towards a unified microscopic description of nuclear deformation, *Phys. Lett. B* **69**, 385 (1977).
65. Heyde, K., Van Isacker, P., Casten, R. F., Wood, J. L., A shell-model interpretation of intruder states and the onset of deformation in even-even nuclei, *Phys. Lett. B* **155**, 303 (1985).
66. Otsuka, T. and Tsunoda, Y., The role of shell evolution in shape coexistence, *J. Phys. G*, **43**, 024009 (2016).
67. Sels, S., *et al.*, Shape staggering of midshell mercury isotopes from in-source laser spectroscopy compared with density-functional-theory and Monte Carlo shell-model calculations, *Phys. Rev. C* **99**, 044306 (2019).
68. Tsunoda, Y., Otsuka, T., Configuration Interaction Approach to Atomic Nuclei: The Shell Model, "Handbook of Nuclear Physics" eds. Tanihata, I., Toki, H., Kajino, T. (Springer, Singapore, 2023), doi=10.1007/978-981-19-6345-2_17
69. Yukawa, H., On the Interaction of Elementary Particles. I, *Proc. Phys. Math. Soc. Japan* **17**, 48 (1935)
70. Bethe, H. A., The Meson Theory of Nuclear Forces I. General Theory, *Phys. Rev.* **57**, 260 (1940)
71. Tsunoda, N., Otsuka, T., Tsukiyama, K., Hjorth-Jensen, M., Renormalization persistency of the tensor force in nuclei, *Phys. Rev. C* **84**, 044322 (2011).
72. Larsson, S. E., Leander, G., Fission Barriers for Heavy Elements with Quadrupole, Hexadecapole and Axially Asymmetric Distortions Taken into Account Simultaneously, *Physics and Chemistry of Fission 1973, Proc. of the 3rd IAEA Symposium on the Physics and Chemistry of Fission* (International Atomic Energy Agency, Vienna, 1974), vol. I, p. 177.
73. Ćwiok, S., Heenen, P.-H., Nazarewicz, W., Shape coexistence and triaxiality in the superheavy nuclei, *Nature* **433**, 705 (2005).
74. Sobczewski, A., Kowal, M., Shvedov, L., Search for less important deformations in the shapes of heaviest nuclei, *Acta Physica Polonica B* **38**, 1577 (2007).
75. Kowal, M., Jachimowicz, P., Sobczewski, A., Fission barriers for even-even superheavy nuclei, *Phys. Rev. C* **82**, 014303 (2010).
76. Benrabia, K., Medjadi, D. E., Imadalou, M., Quentin, P., Triaxial quadrupole dynamics and the inner fission barrier of some heavy even-even nuclei, *Phys. Rev. C* **96**, 034320 (2017).
77. Delaroche, J.-P., Girod, M., Libert, J., Goutte, H., Hilaire, S., P'eu, S., Pillet, N., Bertsch, G. F., Structure of even-even nuclei using a mapped collective Hamiltonian and the D1S Gogny interaction, *Phys. Rev. C* **81**, 014303 (2010).
78. Li, Z.P., Nikšić, T., Vretenar, D., Ring, P., and D. Meng, J., Relativistic energy density functionals: Low-energy collective states of ^{240}Pu and ^{166}Er , *Phys. Rev. C* **81**, 064321 (2010).
79. Yang, Y. L., Wang, Y. K., Zhao, P. W., Li, Z. P., Nuclear landscape in a mapped collective Hamiltonian from covariant density functional theory, *Phys. Rev. C* **104**, 054312 (2021); Supplemental Material <http://link.aps.org/supplemental/10.1103/PhysRevC.104.054312>.
80. Sharpey-Schafer, J. F., Bark, R. A., Bvumbi, S. P., Dinoko, T. R. S., Majola, S. N. T., "Stiff" deformed nuclei, configuration dependent pairing and the β and γ degrees of freedom, *Eur. Phys. J. A* **55**, 15 (2019).
81. Fahlander, C., Axelsson, A., Heinebrodt, M., Hartlein, T., Schwalm, D., Two-phonon γ -vibrational states in ^{166}Er , *Phys. Lett. B* **388**, 475 (1996).
82. Garrett, P. E., Kadi, M., Li, Min, McGrath, C. A., Sorokin, V., Yeh, Minfang, Yates, S. W., $K^\pi=0^+$ and 4^+ Two-Phonon γ -Vibrational States in ^{166}Er , *Phys. Rev. Lett.* **78**, 4545 (1997).
83. Garrett, P. E., Wood, S. W., Yates, S. W., Critical insights into nuclear collectivity from complementary nuclear spectroscopic methods, *Phys. Scr.* **83**, 063001 (2018).
84. Jehangir, S., Bhat, G. H., Sheikh, J. A., Frauendorf, S., Majola, S. N. T., Ganai, P. A. and Sharpey-Schafer, J. F., Quasiparticle and γ -band structures in ^{156}Dy , *Phys. Rev. C* **97**, 014310 (2018).
85. Fortunato, L., Solutions of the Bohr hamiltonian, a compendium, *Eur. Phys. J. A* **26**, 1 (2005).
86. Próchniak, L., Rohoziński, S. G., Quadrupole collective states within the Bohr collective Hamiltonian, *J. Phys. G: Nucl. Part. Phys.* **36**, 123101 (2009).
87. Casten, R. F., *Nuclear structure from a simple perspective*, (Oxford U.P., Oxford, 1990).
88. Zamfir, N. V., Casten, R. F., Signatures of γ softness or triaxiality in low energy nuclear spectra, *Phys. Lett. B* **260**, 265 (1991).
89. Sun, Y., Hara, K., Sheikh, J. A., Hirsch, J. G., Velázquez, V., Guidry, M., Multiphonon γ -vibrational bands and the triaxial projected shell model, *Phys. Rev. C* **61**, 064323 (2000).
90. Boutachkov, P., Aprahamian, A., Sun, Y., Sheikh, J.A., Frauendorf, S., In-band and inter-band B(E2) values within the Triaxial Projected Shell Model, *Eur. Phys. J. A* **15**, 455 (2002).
91. Frauendorf, S., The low-energy quadrupole mode of nuclei, *Int. J. Mod. Phys. E* **24**, 1541001 (2015).
92. Frauendorf, S., Gu, Y., Sun, J., Tidal waves - A non-adiabatic microscopic description of the yrast states in near-spherical nuclei, *Int. J. Mod. Phys. E* **20**, 465 (2011).
93. Sheikh, J. A., Hara, K., Triaxial projected shell model approach, *Phys. Rev. Lett.* **82**, 3968 (1999).
94. Tajima, N., Takahara, S., Onishi, N., Extensive Hartree-Fock+BCS calculation with Skyrme SIII force, *Nucl. Phys. A* **603** 23 (1996).
95. Hayashi, A., Hara, K., Ring, P., Existence of Triaxial Shapes in

- Transitional Nuclei. Phys. Rev. Lett. **53**, 337 (1984).
96. Cline, D., NUCLEAR SHAPES STUDIED BY COULOMB EXCITATION, Ann. Rev. Nucl. Part. Sci. **36**, 683 (1986).
 97. Fahlander, C., Thorslund, I., Varnestig, B., *et al.*, TRIAXIALITY IN ^{166}Er , Nucl. Phys. A **537**, 183 (1992).
 98. Werner, V., Scholl, C., von Brentano, P., Triaxiality and the determination of the cubic shape parameter K_3 from five observables, Phys. Rev. C **71**, 054314 (2005).
 99. Kotliński, B., Cline, D., Bäcklin, A., *et al.*, COULOMB EXCITATION OF ^{166}Er , Nucl. Phys. A **517**, 365 (1990).
 100. Weinberg, S., Nuclear forces from chiral lagrangians, Phys. Lett. B **251**, 288 (1990).
 101. Machleidt, R., Entem, D. R., Chiral effective field theory and nuclear forces, Phys. Rep. **503**, 1 (2011).
 102. Nambu, Y., Axial Vector Current Conservation in Weak Interactions, Phys. Rev. Lett. **4**, 380 (1960).
 103. Goldstone, J., Field Theories with <<Superconductor>> Solutions, Nuovo Cimento (1955-1965) **19**, 154 (1961).
 104. Goldstone, J., Salam, A., Weinberg, S., Broken Symmetries, Phys. Rev. **127**, 965 (1962).
 105. Tsunoda, Y., Shimizu, N., and Otsuka, T., Shape transition of Nd and Sm isotopes and the neutrinoless double- β -decay nuclear matrix element of ^{150}Nd , Phys. Rev. C, **108**, L021302 (2023).
 106. Robledo, L. M. Rodríguez-Guzmán, R. R. and Sarriuren, P. Evolution of nuclear shapes in medium mass isotopes from a microscopic perspective, Phys. Rev. C **78**, 034314 (2008).
 107. Li, Z. P. Nikšić, T. Vretenar, D. Meng, J. Lalazissis, G. A. and Ring, P. Microscopic analysis of nuclear quantum phase transitions in the $N \approx 90$ region, Phys. Rev. C **79**, 054301 (2009).
 108. Nikšić, T., Ring, P., Vretenar, D., Tian, Yuan, Ma, Zhongyu, 3D relativistic Hartree-Bogoliubov model with a separable pairing interaction: Triaxial ground-state shapes, Phys. Rev. C **81**, 054318 (2010).
 109. Kleemann, J., *et al.*, Gamma decay of the ^{154}Sm Isovector Giant Dipole Resonance: Smekal-Raman Scattering as a Novel Probe of Nuclear Ground-State Deformation, <https://arxiv.org/abs/2406.19695>.
 110. Nilsson, S. G., Binding states of individual nucleons in strongly deformed nuclei, Mat. Fys. Medd. Dan. Vid. Selsk. **29**, 16 (1955).
 111. Pietralla, N., von Brentano, P., Herzberg, R.-D., Kneissl, U., Lo Iudice, N., Maser, H., Pitz, H. H., Zilges, A., Systematics of the excitation energy of the 1^+ scissors mode and its empirical dependence on the nuclear deformation parameter, Phys. Rev. C **58**, 184 (1998).
 112. Giacalone, G., A matter of shape: seeing the deformation of atomic nuclei at high-energy colliders, Ph.D thesis, Université Paris-Saclay, CNRS, CEA, <https://arxiv.org/abs/2101.00168>.
 113. Bally, B., Bender, M., Giacalone, G., Somà, V., Evidence of the Triaxial Structure of ^{129}Xe at the Large Hadron Collider, Phys. Rev. Lett. **128**, 082301 (2022).
 114. Jia, J., Probing triaxial deformation of atomic nuclei in high-energy heavy ion collisions, Phys. Rev. C **105**, 044905 (2022).
 115. Dimri, A., Bhatta, S., Jia, J., Impact of nuclear shape fluctuations in high-energy heavy ion collisions, Eur. Phys. J. A. **59**, 45 (2023).
 116. Giacalone, G., Many-body correlations for nuclear physics across scales: from nuclei to quark-gluon plasmas to hadron distributions, Eur. Phys. J. A. **59**, 297 (2023).
 117. Ryssens, W., Giacalone, G., Schenke, B., Shen, C., Evidence of Hexadecapole Deformation in Uranium-238 at the Relativistic Heavy Ion Collider. Phys. Rev. Lett. **130**, 212302 (2023).
 118. Adamczyk, L., *et al.* (STAR Collaboration), Azimuthal Anisotropy in U+U and Au+Au Collisions at RHIC, Phys. Rev. Lett. **115**, 222301 (2015).
 119. ALICE Collaboration, Anisotropic flow in Xe-Xe collisions at $\sqrt{s_{NN}} = 5.44$ TeV, Phys. Lett. B **784**, 82 (2018).
 120. Sirunyan, A. M., *et al.* (CMS Collaboration), Charged-particle angular correlations in XeXe collisions at $\sqrt{s_{NN}} = 5.44$ TeV, Phys. Rev. C **100**, 044902 (2019).
 121. Aad, G., *et al.* (ATLAS Collaboration), Measurement of the azimuthal anisotropy of charged-particle production in Xe + Xe collisions at $\sqrt{s_{NN}} = 5.44$ TeV with the ATLAS detector, Phys. Rev. C **101**, 024906 (2020).
 122. Abdallah, M. S., *et al.* (STAR Collaboration), Search for the chiral magnetic effect with isobar collisions at $\sqrt{s_{NN}} = 200$ GeV by the STAR Collaboration at the BNL Relativistic Heavy Ion Collider, Phys. Rev. C **105**, 014901 (2022).
 123. ALICE Collaboration, Characterizing the initial conditions of heavy-ion collisions at the LHC with mean transverse momentum and anisotropic flow correlations, Phys. Lett. B **834**, 137393 (2022).
 124. Aad, G., *et al.* (ATLAS Collaboration), Correlations between flow and transverse momentum in Xe+Xe and Pb+Pb collisions at the LHC with the ATLAS detector: A probe of the heavy-ion initial state and nuclear deformation, Phys. Rev. C **107**, 054910 (2023).
 125. Frauendorf, S., Spontaneous symmetry breaking in rotating nuclei, Rev. Mod. Phys. **73**, 463 (2001)
 126. Brown, B. A., Wildenthal, B. H., Status of the Nuclear Shell Model, Annu. Rev. Nucl. Part. Sci. **38**, 29 (1988).
 127. Utsuno, Y., Otsuka, T., Brown, B. A., Honma, M., Mizusaki, T., Shimizu, N., Shape transitions in exotic Si and S isotopes and tensor-force-driven Jahn-Teller effect Phys. Rev. C **86**, 051301 (R) (2012).
 128. Bender, M., and Heenen, P.-H., Configuration mixing of angular-momentum and particle-number projected triaxial Hartree-Fock-Bogoliubov states using the Skyrme energy density functional, Phys. Rev. C **78**, 024309 (2008).
 129. Iachello, F., Arima, A., *The Interacting Boson Model*, (Cambridge University Press, 1987).
 130. Yanase, K., *et al.*, to appear.
 131. Talmi, I., Simple Models of Complex Nuclei: The Shell Model and Interacting Boson Model, (CRC Press, Boca Raton, 2017).
 132. Shimizu, N., Mizusaki, T., Utsuno, Y. & Tsunoda, Y., Thick-Restart Block Lanczos Method for Large-Scale Shell-Model Calculations, Comp. Phys. Comm. **244**, 372 (2019).
 133. Gloeckner, D. H. and Lawson, R. D., Spurious Center-of-Mass Motion, Phys. Lett. B **53**, 313 (1974).